Tuning the Passive Structural Response of an Oscillating-foil Propulsion Mechanism for Improved Thrust Generation and Efficiency

by

Andrew James Richards
B.A.Sc., The University of British Columbia, 2011

A Thesis Submitted in Partial Fulfillment of the
Requirements for the Degree of

Master of Applied Science

in the Department of Mechanical Engineering

University of Victoria

Tuning the Passive Structural Response of an Oscillating-foil Propulsion Mechanism for Improved Thrust Generation and Efficiency

by

Andrew James Richards
B.A.Sc., The University of British Columbia, 2011

Supervisory Committee

Dr. Peter Oshkai, Supervisor
(Department of Mechanical Engineering)

Dr. Brad Buckham, Departmental Member
(Department of Mechanical Engineering)

Supervisory Committee

Dr. Peter Oshkai, Supervisor
(Department of Mechanical Engineering)

Dr. Brad Buckham, Departmental Member
(Department of Mechanical Engineering)

ABSTRACT

While most propulsion systems which drive aquatic and aerial vehicles today are based on rotating blades or foils, there has recently been renewed interest in the use of oscillating foils for this purpose, similar to the fins or wings of biological swimmers and flyers. These propulsion systems offer the potential to achieve a much higher degree of manoeuvrability than what is possible with current man-made propulsion systems. There has been extensive research both on the theoretical aspects of oscillating-foil propulsion and the implementation of oscillating foils in practical vehicles, but the current understanding of the physics of oscillating foils is incomplete. In particular, questions remain about the selection of the appropriate structural properties for the use of flexible oscillating foils which, under suitable conditions, have been demonstrated to achieve better propulsive performance than rigid foils.

This thesis investigates the effect of the foil inertia, stiffness, resonant frequency and oscillation kinematics on the thrust generation and efficiency of a flexible oscillating-foil propulsion system. The study is based on experimental measurements made by recording the applied forces while driving foil models submerged in a water tunnel in an oscillating motion using servo-motors. The design of the models allowed for the construction of foils with various levels of stiffness and inertia. High-speed photography was also used to observe the dynamic deformation of the flexible foils.

The results show that the frequency ratio, or ratio of oscillation frequency to resonant frequency, is one of the main parameters which determines the propulsive efficiency since the phase of the deformation and overall amplitude of the motion of the bending foil depend on this ratio. When comparing foils of equivalent resonant frequency, heavier and stiffer foils were found to achieve greater thrust production than lighter and more flexible foils but the efficiency of each design was comparable. Through the development of a semi-empirical model of the foil structure, it was shown that the heavier foils have a lower damping ratio which allows for greater amplification of the input motion by the foil deformation. It is expected that the greater motion amplitude in turn leads to the improved propulsive performance. Changing the Reynolds number of the flow over the foils was found to have little effect on the relation between structural properties and propulsive performance. Conversely, increasing the amplitude of the driven oscillating motion was found to reduce the differences in performance between the various structural designs and also caused the peak efficiency to be achieved at lower frequency ratios. The semi-empirical model predicted a corresponding shift in the frequency ratio which results in the maximum amplification of the input motion and also predicted more rapid development of a phase lag between the deformation and the actuating motion at low frequency ratios. The shift in the location of the peak efficiency was attributed to these changes in the structural dynamics. When considering the form of the oscillating motion, foils driven in combined active rotation and translation motions were found to achieve greater efficiency but lower thrust production than foils which were driven in translation only. The peak efficiencies achieved by the different structural designs relative to each other also changed considerably when comparing the results of the combined motion trials to the translation-only cases. To complete the discussion of the results, the implications of all of these findings for the design of practical propulsion systems are examined.

Contents

List of Tables

List of Figures

ACKNOWLEDGEMENTS

First, I would like to thank my advisor, Dr. Peter Oshkai, whose guidance and advice have made this research work a rewarding experience and enabled its successful completion. I would also like thank Dr. Brad Buckham from the Department of Mechanical Engineering at UVic and Dr. Robert Shadwick from the Department of Zoology at UBC for offering their time and expertise as examiners for the thesis defence.

I am grateful to Rodney Katz and the co-op students in the UVic Mechanical Engineering machine shop for their technical assistance. Without their knowledge of mechanical design and skills in manufacturing, it would not have been possible to construct the elaborate apparatus required for the experiments. I would also like to thank Peggy White and Susan Walton for providing administrative support and for fostering a friendly and collegial atmosphere within the Institute for Integrated Energy Systems (IESVic) research group.

Many friends have enriched my life here in Victoria. I thank them both for their help with the research and also for the many hours of fishing, hiking and playing board games which we enjoyed together. The loving support of my family throughout my academic career is also greatly appreciated.

Financial support from NSERC through a Canada Graduate Scholarship and from the Trussell family and the Vancouver Foundation through the Paul and Helen Trussell Science and Technology Scholarship was gratefully appreciated.

Finally, a special acknowledgement is owed to Dr. Mina Hoorfar who was a mentor to me during my time as an undergraduate at UBC. Dr. Hoorfar's enthusiasm for scientific research taught me the value of the opportunities for creative thinking and intellectual discovery which only this endeavour can provide. Her efforts will continue to inspire and motivate me in all of my work as an engineer.

Chapter 1

Introduction

Flying and swimming animals such as insects, birds and fish have long served as inspiration for human inventors seeking to create aircraft or watercraft. While the mechanical systems which propel the airplanes and ships of today differ distinctly from this original biological inspiration by the use of rotating rather than oscillating blades, in recent years there has been renewed interest in the development of mechanical propulsion systems based on oscillating blades or foils. These novel designs offer the potential to achieve the very high degree of manoeuvrability observed in natural flyers and swimmers which is yet unmatched by any man-made vehicles [1]. The ability to perform station keeping operations, rapid starts and stops, and sudden direction changes would be invaluable for such bioinspired vehicles which are envisioned to find applications in the inspection of underwater structures [2], military or civilian reconnaissance [3] and extraterrestrial exploration [4].

Various researchers have successfully implemented oscillating foils in proof-of-concept prototype vehicles. Notable examples include the *RoboTuna* [5] and the more recent *DelFly* project [6]. Alongside these efforts to develop practical vehicles, there has been a large body of research which examined the operation of oscillating foils from a more theoretical standpoint with the aim to improve thrust production and efficiency. One topic within this field which has received considerable attention is the effects of using flexible oscillating foils. While the results of these works have demonstrated the potential to improve thrust production and efficiency by introducing flexibility into the the foil structure, the selection of the appropriate structural properties to improve performance under a given set of oscillation and forward travel kinematics remains to a large extent an open question. The work described in this thesis uses experimental measurements to further develop the knowledge towards a more complete understanding of the combined effect of structural properties and kinematic parameters on the performance an oscillating-foil propulsion mechanism.

The design of an oscillating-foil propulsion system requires the selection of parameters which can be grouped into two general categories:

1. the kinematics of the oscillating motion, and
2. the shape and structure of the foils.

The primary objective in the selection of these parameters is to have the system develop sufficient thrust forces such that the vehicle is able to hold its position or move forward against resisting forces such as fluid drag or the vehicle weight. As a secondary objective, it is desirable to produce with this thrust force with the minimum power input to the system or, in other words, to have high propulsive efficiency. Typically, the parameters must be chosen from within ranges set by various constraints such as the vehicle size, material properties and the limitations of the drive mechanism actuating the flapping motion.

To meet the performance objectives in the design of a propulsion system, it is necessary for engineers to understand the effect of the various design parameters on the thrust generation and efficiency. For this reason, the performance of oscillating foils throughout a wide range of operating conditions has been studied extensively. Since the findings of these works have led to the questions which are addressed by the research conducted for this thesis, it is worthwhile to begin by examining the present understanding of the fluid flow and physics of flexible oscillating foils. This synopsis of the current theory comprises the first four subsections of this chapter which begin with an overview of the basic definitions and important parameters in Section 1.1 followed by discussions of unsteady force generation, wake structure, and the effects of flexibility in Sections 1.2, 1.3 and 1.4 respectively. Following this review of the knowledge provided by existing works, Section 1.5, poses the central research questions addressed by this thesis and explains how the answers will contribute to the design of future propulsion systems with improved performance. Section 1.6 then identifies the specific objectives of the present experimental work and Section 1.7 outlines the content in the remaining chapters of the thesis.

1.1 Overview of Oscillating-foil Propulsion

Typically, an oscillating foil used for propulsion will undergo a heaving motion in which the foil translates perpendicular to the direction of travel, a pitching motion in which the foil rotates about a spanwise axis, or a combination of pitching and heaving [7]. A sequence of images showing the typical positioning with respect to time of a foil undergoing combined pitching and heaving motions for locomotion is shown in Figure 1.1.

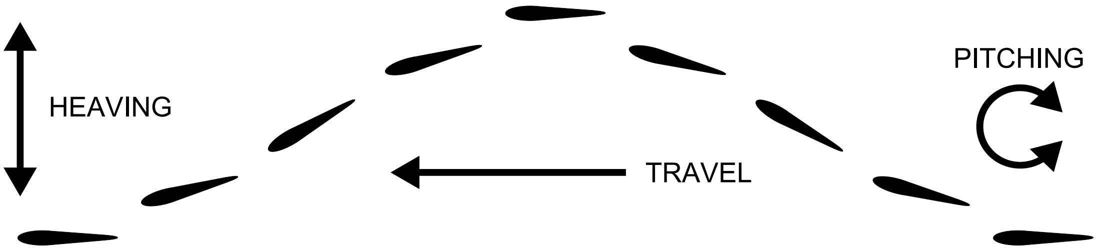

Figure 1.1: Movement of an oscillating foil undergoing combined heaving and pitching motions.

Fundamentally, the relative motion of the foil and the fluid generates a pressure on the surface of the foil resulting in a force which is directed to either support a weight or overcome drag forces in forward propulsion [8]. The method of generating this force can be classified as lift-based or drag-based [7]. In drag-based propulsion, the foil moves in a rowing motion, pushing the surrounding fluid away in a direction opposite to the desired force. This method of force generation allows for the most precise control of the force direction which is useful for the low-speed, high-precision manoeuvring of a vehicle [7]. However, lift-based propulsion is generally more efficient than drag-based force generation and is thus more suitable for travel over long distances or at high speeds or prolonged hovering flight [7]. Because of its suitability for the majority of vehicle operating conditions, the lift-based mechanism is likely to play a larger role in most propulsion systems. For this reason, the research conducted for this thesis and the remainder of the discussion in this chapter will consider lift-based propulsion.

In lift-based propulsion, the foil acts as a lifting surface to produce a force which is orthogonal to, rather than aligned with, the direction of the relative velocity between the foil and the surrounding fluid. The motion of the foil directs the fluid flow in such a way as to establish a bound circulation around the foil. This bound circulation results in a pressure difference across the foil and generates a lift force according to the Kutta-Jukowski theorem [9], similar to the function of a wing in steady flight. When generating forces in this way, the pitching and heaving motions are timed to orient the foil such that one component of the lift force is directed along the travel path. If this force component is sufficiently large, it will act to provide a net forward thrust by overcoming the drag resisting the forward travel. This explanation for the generation of forces by an oscillating foil is referred to as the Knoller-Betz effect, after researchers who independently developed the theory in the early twentieth century [10, 11]. The foil also produces forces which oppose the oscillating motion, requiring a power input to drive the system. A diagram showing the relevant force and velocity vectors at one instant during the oscillation cycle of a lift-based propulsor is given in Figure 1.2.

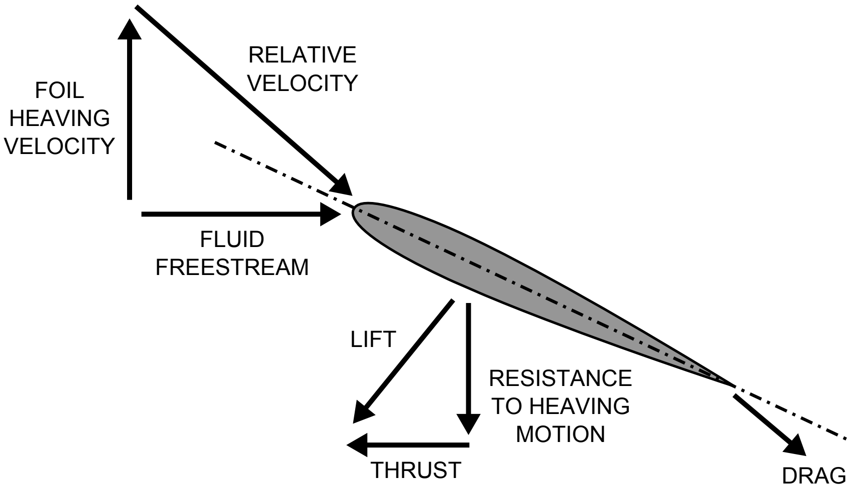

Figure 1.2: Relevant velocity and force vectors for an oscillating foil used in lift-based propulsion.

Having made the decision to use an oscillating-foil propulsion system, vehicle designers are then presented with task of selecting the specific motion kinematics and foil structure. These choices will in turn set a number of parameters which have been shown in the literature to affect the thrust generation and efficiency. The proper selection of these parameters is therefore necessary in order to meet the design objectives. With respect to the foil itself, the geometric shape of the foil, both in profile and planform as well as the ratio of span to chord length, or aspect ratio, are known to be relevant [7]. Pertinent kinematic parameters include the motion profiles used for the heaving and pitching motions, the timing between the two motions, the average and maximum angles of attack, and the ratio of the heaving amplitude to the foil chord length, h_0/c [7]. To account for the influence of the surrounding fluid, the dimensionless Reynolds number and Strouhal number are also important [7]. The Reynolds number quantifies the ratio of viscous and inertial forces, and is given by the expression:

$$Re = \frac{Uc}{\nu} \tag{1.1}$$

where U is the forward velocity, c is the foil chord length and and ν is the kinematic viscosity . The significance of the Strouhal number arises due to the dynamic behaviour of the flow in the foil wake. This quantity is given by

$$St = \frac{fA}{U} \tag{1.2}$$

where f is the flapping velocity and A the width of the wake.

To quantify the performance of an oscillating-foil propulsion system and to make comparisons between design alternatives, it is useful to define a further set of three dimensionless groupings: the thrust coefficient, the power coefficient, and the efficiency [12]. The thrust coefficient, which is given by

$$C_T = \frac{Q}{\rho U^2 a} \tag{1.3}$$

where Q is the thrust, ρ is the fluid density, and a is the planform area, expresses the thrust production normalized by the flow speed and foil size . The power coefficient is a similar grouping to express the input power, P, and is defined

$$C_P = \frac{P}{\rho U^3 a} \tag{1.4}$$

The efficiency is given by the ratio of these two coefficients,

$$\eta = \frac{C_T}{C_P} \tag{1.5}$$

and relates the output power in direction of travel to the input power required to generate the motion. Because the thrust generation and required power input vary with the foil velocity and orientation throughout the oscillation cycle, it is generally necessary to take time averages of these quantities over the oscillation period in order to understand the effectiveness of a given propulsion system design [12]. Therefore, throughout this thesis the terms thrust coefficient, power coefficient and efficiency will refer to the cycle averages unless the qualifier *instantaneous* is applied.

The discussion in this section has explained the fundamental operation of an oscillating-foil propulsion systems and identified a number of relevant geometric, kinematic and fluid mechanical parameters. The subsequent subsections will examine in more detail the underlying physical mechanisms of thrust generation and how the design of the propulsion system enables or impedes these phenomena.

1.2 Mechanisms of Unsteady Force Generation

While the production of a lift force by an oscillating foil is similar to the action of other foils such as the wings of an aircraft undergoing steady translation, there are a number of interesting phenomena which arise due to the unsteady oscillating motion. Considering one instant of the oscillation cycle, these phenomena may act to increase the lift force beyond what would be generated by a foil with the same geometry undergoing a steady motion with the same velocity and angle of attack. Three main mechanisms which enhance the unsteady lift generation of oscillating foils have been identified as delayed stall, rotational circulation and wake capture [7,9]. Added mass effects, which are caused by the fluid inertia, also contribute to the forces on oscillating foils [9].

When the delayed stall phenomenon occurs, the flow on the upper surface of a foil translating at a high angle of attack separates from the foil at the leading edge. The separated flow will initially reattach to the foil surface at some location back towards the trailing edge. The fluid between the separation and reattachment points circulates in what is termed a leading edge vortex. The fluid in the leading edge vortex is at low pressure, and thus gives rise to suction which serves to augment the lift force [13]. The leading edge vortex can also be understood to be increasing the circulation on the foil, and thus also increases the lift by the Kutta-Jukowski theorem [13]. In steady operation, the leading edge vortex will grow in size, forcing the reattachment point back along the chord, until passing the trailing edge and causing the flow to become completely detached. In the case of a detached flow, the foil no longer serves to direct the flow properly to generate a lift force, resulting in a stall condition [9]. In an oscillating foil, the stall can be avoided by setting the phase between the pitching and heaving motions such that the leading edge vortex is shed at the correct time during the oscillation cycle when it will not interfere with lift generation [12]. Alternatively, in the case of a three-dimensional foil, certain kinematics of the oscillating motion can establish a spanwise flow which convects momentum out of the leading edge vortex and thus limits its growth. For example, in many insects the heaving motion is generated by rotating the wings about a pivot point on the insect's body. In these cases, it is speculated that a spanwise flow can be attributed to the pressure gradient associated with changing cordwise velocity along the length of the wing or to a centrifugal effect [13].

In cases where oscillating foils take advantage of rotational circulation, the pitching motion serves to enhance the lift forces, especially near the stroke reversals when the rotation is generally fastest [9]. For an airfoil undergoing steady translation, there is a stagnation point at the trailing edge where the local relative velocity between the fluid and foil is zero. If the foil rotates about a spanwise axis, the stagnation point moves away from the trailing edge. This repositioning of the stagnation point forces the fluid flow to turn sharply as it goes around the trailing edge, resulting in a strong velocity gradient at this point. The velocity gradient in turn gives rise to strong viscous forces which act to restore the stagnation point to the trailing edge and in doing so increase the bound circulation on the foil [9]. Since lift is proportional to bound circulation, the lift forces also increase. This effect is alternately termed the Kramer effect or rotational circulation [9]. The amount of additional lift provided by rotational circulation is affected by both the relative timing of the pitching and heaving motion, and also by the chordwise position of the pitching axis [14].

Wake capture refers to interaction between an oscillating foil and the velocity field induced in the surrounding fluid by its motion. At the stroke reversals, the bound circulation is transferred from the foil to the surrounding fluid in the form of shed vortices. These vortices can increase the relative velocity between the fluid and the foil at the beginning of the subsequent stroke [9]. With the correct timing of the pitching and heaving motions, this increase in relative velocity can also lead to an increase in the lift force [9, 14].

Added mass is an inertial effect associated with the accelerations of an oscillating foil. As the foil accelerates, some of the surrounding fluid is displaced and also undergoes acceleration. Additional force will be imposed on the foil to accelerate the inertia of this fluid [9]. This resulting force is in phase with the foil acceleration, and the inertia of the accelerated fluid appears to be added to the mass of the foil, hence the term *added mass*.

The extent to which each of the lift-enhancing unsteady flow phenomena play a role in the force generation for any given foil will depend on the parameters governing the foil performance mentioned in Section 1.1. Depending on the design goal of the propulsion system, these parameters may be tailored to use the various unsteady effects to a greater or lesser extent. For example, while delayed stall and the accompanying leading edge vortices may give rise to very substantial lift forces, drag is also increased, lowering the propulsive efficiency. Therefore, for short-term hovering flight when supporting the vehicle weight is critical, it is reasonable to operate a foil at high angles of attack to cause leading edge separation which leads the formation of leading edge vortices and enhances lift generation. However, for long distance swimming, where efficiency is the primary goal, the average angle of attack of the foil should be reduced to achieve lower drag [7].

1.3 Wake Dynamics

Because of the unsteady flow phenomena discussed in Section 1.2 the forces on an oscillating foil will generally be different from what is predicted by lift and drag coefficients which are measured at steady state. For this reason, it is often more effective to gain a high-level understanding of the thrust production by oscillating foils by considering the dynamics of the foil wake, rather than trying to relate the foil motion to the force generation using basic aerodynamic theory.

The foil wake refers to the region of fluid around the foil where the flow has been disturbed by the foil presence. Because the flow velocity is different in this region, the foil wake constitutes a shear layer. This shear layer can be shown to be unstable, meaning that when disturbances act to alter the direction of the flow in this region, the shear layer flow does not act to correct these changes [15]. Instead, the disturbances are amplified, causing the flow to further deviate from the original path. This amplification of disturbances is said to be convective, meaning that its effect does not propagate throughout the entire flow field. Rather, the changes to the flow caused by the disturbance are observed to grow in time but are convected downstream from the point where the disturbance was originally applied [15]. Due to saturation effects, the disturbances cannot be amplified indefinitely to infinite amplitude, but rather causes the flow to form circulating vortices in the foil wake [15].

Fundamentally, any object which is acting to generate thrust in a fluid must produce a jet-like wake profile where the momentum flux within the wake exceeds that of the surrounding free-stream flow [15]. The formation of this wake can be attributed to the conservation of momentum which requires that the thrust force on the object be balanced by momentum imparted to the fluid in the opposite direction. In a time-averaged sense, an unstable shear layer will develop this jet-like profile when the vortices resulting from the amplification of disturbances are arranged as shown in Figure 1.3. In this case, the velocity fields of the vortices in each row will add together in the direction of the flow along the wake centerline. This arrangement of vortices is referred to as a reverse Kármán vortex street and has been experimentally observed in the wake of thrust-producing oscillating foils [11, 12, 16].

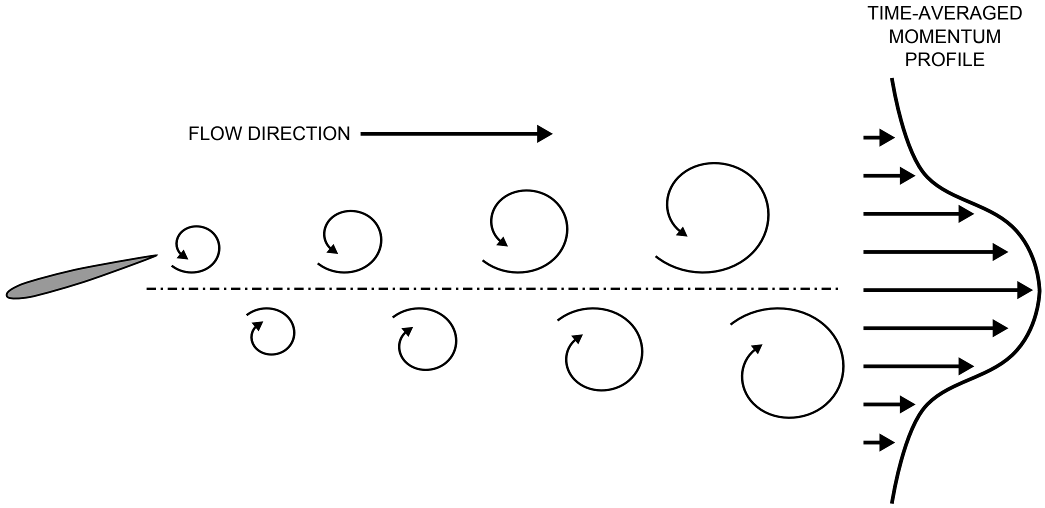

Figure 1.3: Vortex arrangement in a reverse Kármán street wake structure.

The amplification of disturbances by an unstable shear layer is frequency selective, meaning that disturbances applied at certain frequencies will more rapidly lead to the development of stronger vortices [15]. Since the development of the development of a reverse Kármán vortex street through the amplification of disturbances in turn leads to the formation of a distinct thrust-producing jet, it is desirable for an oscillating foil to apply disturbances at the frequency of maximum amplification in order to achieve the optimal propulsive efficiency [15].

The frequency response of an unstable shear layer is related to its width and the flow velocity. In the operation of an oscillating foil, the shear layer width is related to the motion amplitude, and disturbances are applied at the oscillation frequency. The Strouhal number given by Equation 1.2), which relates all three of the parameters affecting the stability of the shear layer, is therefore a key dimensionless parameter governing the thrust production and efficiency of an oscillating foil. Analysis of a typical jet velocity profiles observed in experimental studies indicates that the frequency of maximum amplification corresponds to Strouhal numbers in the range of $0.25 < St < 0.35$, with the specific value dependent on the ratio of the jet centerline velocity to the mean flow velocity [15]. Observation of the swimming behaviour of several species of fish shows that natural swimmers typically operate in this relatively narrow range of Strouhal numbers that provide high efficiency, even over range of Reynolds numbers of several orders of magnitude [15].

Equipped with an understanding of the importance of operating oscillating foils in the correct range of Strouhal numbers, Anderson et al. [12] undertook an extensive parametric study to identify the conditions for maximum propulsive efficiency. This study employed a combination of direct force measurement and flow visualisation. The force measurements indicated that high efficiency is achieved when the ratio of heave amplitude to chord length is large, the maximum angle of attack is in the range of 15°-25°, and Strouhal number based on trailing edge excursion is in the range of $0.3 < St < 0.4$. A thrust-producing reverse Kármán vortex street was observed for Strouhal numbers between 0.2 and 0.5 and maximum angles of attack between 7°and 50°. In this flapping regime, the foil shed two vortices into the wake during each oscillation cycle. Leading edge separation was observed, but the associated leading edge vortex was found to amalgamate with the trailing edge vortex before shedding into the wake.

1.3.1 Three-dimensional Foil Wakes

In many of the existing studies using flow visualisation to demonstrate the formation of a reverse Kármán vortex street in the wake of an oscillating foil such as [12, 16], the authors used measures such as high-aspect-ratio foils and end plates to create an approximately two-dimensional flow in the imaging plane at the foil mid-span location. In general, if these measures are not put in place the wake of a three-dimensional foil may be considerably different from a reverse Kármán street [17]. Vortex lines do not terminate in the fluid [18], and consequently all of the vortices surrounding a three-dimensional foil must be interconnected or form ring-like structures [7]. Such patterns of interconnected vortex loops in the wakes of three-dimensional foils been observed experimentally [19,20] as well as in the results of numerical simulations [17,21]. Under some conditions, Dong et al. [17] observed that the vortices in the wake separate into discrete rings. Generally in all of these studies, the specific geometry of the vortex loops was found to depend on the foil aspect ratio as well as the Strouhal number. For example, [17] reports that the vortex rings and loops travel at some angle relative to the freestream flow and that this angle becomes smaller as the aspect ratio is increased, while von Ellenrieder et al. [20] identify a trend where the vortex loops expand in the spanwise direction and contract in the streamwise direction as the Strouhal number is increased. As the aspect ratio of a three-dimensional foil increases, the wake pattern within planes perpendicular to the foil span begins to more closely resemble a reverse Kármán street, especially in the near wake and when the foil is operating at the Strouhal number of peak efficiency [17, 19].

Given the substantial differences between the wakes of two-dimensional and three-dimensional oscillating foils, it is unclear whether the trends relating the propulsive efficiency to Strouhal number described in Section 1.3 can simply be extended to design the operation of physical propulsion systems [20, 22]. These trends have been identified based on the stability two-dimensional shear layers. In the examinations of the propulsive efficiency of finite-aspect-ratio foils which are available in the literature [17, 19, 22], the Strouhal number reported for optimal efficiency is generally outside of the theoretical optimal range identified for two-dimensional foils identified by Triantafyllou et al. [15]. However, in these cases a number of factors including a low Reynolds number and the associated high viscous drag [17], variation of Reynolds number between trials [19], and the interaction among two foils and a rigid body upstream [22] complicate the trends in the results. In contrast to these findings, Barannyk et al. [23] report that the Strouhal number of peak efficiency did fall in the range of $0.25 < St < 0.35$ when conducting experiments with foils having a very low aspect ratio of $\mathcal{AR} = 0.5$. In spite of these quantitative discrepancies, in all of these cases [17,19,22,23], the efficiency was observed to change as the Strouhal number was varied, indicating that this parameter is relevant in the design of all oscillating-foil propulsion systems, even when the aspect ratio is small.

The data available in the literature relating the efficiency of oscillating foils to aspect ratio is limited. From observation of the studies that are available, it appears that the effect the aspect ratio on the efficiency of oscillating foils is small above a certain threshold level. However, quantifying this threshold is difficult because it is likely influenced by other parameters such as the Strouhal number and foil geometry. Buchholz and Smits [19] report that the peak efficiencies achieved in their experiments were similar for foils with an aspect ratio above $\mathcal{AR} = 0.83$, while the efficiency of the lowest aspect ratio panel ($\mathcal{AR} = 0.54$) was considerably lower. In the numerical simulations of [17], the relation between efficiency and Strouhal number collapses onto the same trend line at high Strouhal numbers ($St > 0.85$) for foils with an aspect ratio greater than $\text{Æ} = 2.55$, while the efficiency of a smaller aspect ratio foil ($\text{Æ} = 1.27$) was well below this trend line.

The trends relating the thrust production of three-dimensional oscillating foils to aspect ratio and Strouhal number are somewhat more clear than those for propulsive efficiency. The thrust coefficient is found to increase with Strouhal number as is the case for two-dimensional foils [17,19,23]. When comparing foils operating at the same Strouhal number, higher-aspect-ratio foils achieve a higher thrust coefficient [17,19]. However, the relationship between the thrust coefficient and the aspect ratio is not linear and the effect of aspect ratio is less significant when the aspect ratio is high and the flow structure approaches two-dimensional conditions [17].

The uncertainty in the current understanding of the wake dynamics and the relation between the Strouhal number and efficiency of three-dimensional foils contrasts with the case of two-dimensional foils where the development of a reverse Kármán street leading to efficient thrust production is well known from both theoretical analysis and practical demonstrations. For this reason, further research is required to develop the knowledge which will allow engineers to design with confidence efficient practical propulsion systems using finite aspect ratio foils. In this work described in this thesis, the foils used in the experiments were of relatively low aspect ratio ($\text{Æ} = 0.7$). However, the aspect ratio was not explicitly considered in the experimental parameter space, and owing to the lack of clear design guidelines for the selection of the appropriate kinematics for this foil geometry, the theory developed for two-dimensional foils was applied in the selection of the operating Strouhal number range.

1.4 Effects of Foil Flexibility

Much of the recent research on oscillating-foil propulsion has focused on the use of flexible foils. These studies have been inspired in part by the observation that many natural oscillating foils incorporate some degree of flexibility. Indeed, it is speculated that the passive deformation of fish fins [24], insect wings [25] and the feathers on bird wings [26] plays an important role in the thrust generation of these appendages and improves the biomechanical efficiency of the animals in question. As an additional benefit to using flexible foils, the bending of the foil can act to generate a pitching motion when a heaving motion is applied near the leading edge. By removing the need for separate actuator to drive the pitching motion, the use of flexible foils in a man-made propulsion system can simplify the design of the drive mechanism which in turn makes the vehicle lighter and more reliable [27, 28]. With these advantages in mind, numerous experimental and numerical studies have been undertaken examining the effect of flexibility on the thrust generation and efficiency of oscillating foils.

One early effort to understand the role of foil flexibility in propulsion was conducted by Katz and Weihs [29]. The results of these simulations showed that a flexible oscillating foil was able to achieve higher efficiency than a rigid foil with the same flapping kinematics. While the deformed shape of the flexible foil generated smaller lift forces, the deformation redirected the lift force vector, which acts normal to the foil surface, towards the direction of propulsion. Similar results were found experimentally by Barannyk et al. [23]. This study considered flapping plates comprised of rigid and flexible sections of the chord length. Both the efficiency and thrust generation were found to improve as the fraction of the plate chord comprised by the flexible section increased. However, for high Strouhal numbers, beyond the range of the peak efficiency, all of the plates with varying lengths of rigid and flexible sections reached the same asymptotic efficiency.

While the works of [29] and [23] have demonstrated the possibility to improve the propulsive performance of an oscillating foil by reducing the chordwise bending stiffness, it has also been demonstrated that under certain conditions such as high forward velocities and flapping frequencies a more rigid foil may actually outperform a more flexible one [10, 28, 30]. Heathcote and Gursul [10] measured the propulsive performance of chordwise-flexible foils assembled from flexible steel sheets attached to a rigid aluminum leading edge section. The foils were driven in a flapping motion while immersed in a water flow. The stiffness of the foils was modulated by using sheets of different thickness while the Strouhal number was varied by changing the oscillation frequency. Tests were conducted at three different Reynolds numbers by changing the flow speed. It was found that at low Reynolds numbers, the foils with the thinnest sheets, and highest flexibility, achieved the highest efficiency, while at higher Reynolds numbers, the foils of intermediate flexibility operated more efficiently. Considering the thrust coefficients, the required stiffness for maximum thrust generation was found to increase at higher Strouhal numbers. Similar results were observed by Wu et al. [28] who tested membrane wings reinforced with carbon fibre strips flapping in air. In this work, it was found that at low flapping frequencies the most flexible wings, with the fewest number of reinforcing strips, produced the highest thrust. As the flapping frequency increased, the wings of intermediate flexibility and then finally the most rigid wings were observed to generate highest thrust.

The deformation of a flexible oscillating foil is a dynamic process, meaning that the deformed foil shape will vary in time throughout the oscillation cycle as the direction and magnitude of the applied forces change. This time-varying deformation requires that parts of the foil to accelerate with respect to one another. For this reason, the behaviour of flexible oscillating foils is likely to be influenced not only by the stiffness, which is the resistance to deformation under static loads, but also by the inertia which refers to the tendency of matter to resist changes in velocity. Together, the stiffness and inertia of a structure set its resonant or natural frequency, f_n which characterizes the behaviour in time as the structure recovers from an imposed deformation. If the resonant frequency is included into the characterization of a propulsion system, the frequency ratio f/f_n where f is the flapping frequency, becomes a second important non-dimensional frequency in addition to the Strouhal number. This ratio is important because a structure may either amplify or attenuate the deformations caused by a dynamically applied force depending on the ratio of forcing frequency to resonant frequency. To date, there have been a number of studies which considered the relation among the foil resonant frequency, flapping kinematics, and propulsive efficiency [28, 31–33].

It has been observed in numerical simulations by Michelin and Smith [32] and experiments by Wu et al. [28] that optimal thrust generation can be achieved when the flapping motion is close to the resonant frequency so that the foil deformation amplifies the input motion. However, in the experiments of Ramananarivo et al. [31], no resonant-like peak in the deformation amplitude is observed when the foil is actuated near the resonant frequency and this combination of structural properties and flapping kinematics was actually found to yield sub-optimal thrust and efficiency. The foils were found to perform better when the flapping frequency was lower which resulted in a more appropriate phase difference between the deformation cycle and the input motion. The importance of this proper phasing was also discussed by Wu et al. [28].

Despite the wide breadth of studies which have examined flexible foils in general, and even explicitly considered the resonant frequency, the availability of parametric investigations into the effects of both inertia and stiffness is limited. The work which has examined the effects of inertia is generally restricted to numerical simulations

[32–34] because it is difficult to change the mass of a physical structure without also affecting the stiffness or geometry. However, the simulations have shown that the foil mass is indeed an important parameter. When comparing foils of the same resonant frequency in the results of Yin and Luo [33], the lighter and more flexible foils generally achieve higher performance. Similar findings are included in the results of Zhu [34] where it was shown that in the case of chordwise bending, increasing the relative mass between the foil and the surrounding fluid results in a poor phase between the deformation and the input motion which is not conducive to thrust generation.

Considering the work which has been reviewed here, the results of previous works indicate that the incorporation of the correct degree of flexibility into the design of an oscillating foil can lead to improved propulsive performance. However, further research is required to assist engineers in the selection of the appropriate stiffness and inertia for a given propulsion system. The study described in this thesis is expected to further develop the understanding of this field by addressing the research questions described in the next section.

1.5 The Problem of Tuning the Foil Structure for Improved Thrust Generation and Efficiency

The knowledge contained in the existing literature provides engineers working on oscillating-foil propulsion systems with a set of design guidelines. The studies reviewed in Sections 1.1-1.4 have identified a range of parameters in both the flapping kinematics and foil structure which affect the thrust and efficiency by influencing the unsteady flow around the foil and in the wake. In particular, the research which was examined in Section 1.3 has found that the Strouhal number is a key dimensionless grouping which governs the wake dynamics. Considering the discussion in Section 1.4, it is known that a certain degree of flexibility in the foil structure is beneficial in order to set the frequency ratio which results in either the appropriate phase between the deformation and the actuated oscillating motion or the maximum amplification of this input motion by the deformation. These findings relating the wake and structural dynamics to the propulsive performance raise the issue of “tuning” the foil properties for a given set of flow conditions. More precisely, while both the Strouhal number and frequency ratio have been shown to be important non-dimensional frequencies, the current understanding does not offer specific and quantitative advice regarding the selection of an appropriate combination of stiffness, inertia, and oscillation amplitude and frequency to meet constraints such as forward speed and thrust requirements while also achieving a high efficiency. For this reason, engineers working through the design process of a propulsion system are therefore apt to ask the following logical questions:

1. Can the propulsive efficiency be improved by choosing the stiffness and inertia of a foil such that the optimal Strouhal number and the optimal frequency ratio coincide at the same oscillation frequency?
2. What is the effect on the thrust generation and efficiency if the frequency ratio is set by changing the foil stiffness or inertia?
3. How does the optimal frequency ratio change as the kinematic parameters such as the heaving or pitching amplitude are varied?

In the study described by this thesis, a series of experiments was conducted in attempt to answer these questions. While it is unlikely that the results obtained here will provide engineers with a set of specific rules that can applied ubiquitously in the design of propulsion systems, the findings of this work are expected to demonstrate trends which will be useful in the initial high-level design stages and when planning the testing of a new propulsion system. For instance, it was not possible to answer Question 1 affirmatively indicating that the relation among the structural dynamics, oscillation kinematics and propulsive performance is complicated and the effects of structural changes and variations in the wake structure cannot be isolated from each other. Essentially, the effective kinematics of the motion change due to the deformation of the foil and engineers must account for these changes when planning the operation of an oscillating foil. To answer Question 2, it is demonstrated that heavier foils achieve higher peak thrust when compared to lighter and more flexible foils with the same resonant frequency, but the efficiency of both designs is approximately equivalent. Finally, in an attempt to answer Question 3, it was found that peak efficiency is achieved at a lower frequency ratio as the heaving amplitude is increased. The addition of an active pitch motion was found to reduce thrust production while improving efficiency. These findings concerning the effect of the heave amplitude and active pitching motions will help engineers anticipate the ranges of structural parameters which lead to optimal efficiency once the oscillation kinematics have been established. At the very least, the results of all of the experiments which were undertaken for this thesis will help to guide further research in the field of flexible oscillating-foil propulsion by accentuating the importance of the questions identified here.

1.6 Objectives

With an overall goal to further the understanding of the relationship between the kinematics, structural properties and propulsive performance of oscillating foils, the study described in this thesis has used experimental measurements of thrust production and efficiency to satisfy the following specific objectives:

1. Assess the feasibility of improving efficiency by appropriately matching the foil resonant frequency to the oscillation frequency and amplitude and the forward travel speed.
2. Compare the thrust production and propulsive efficiency of foils with equivalent resonant frequency but different mass and stiffness.
3. Examine the changes in the trends relating the structural properties to propulsive performance as the oscillation amplitude and forward travel speed are varied and an active rotation is added in combination with the translation to the oscillating motion.
4. Develop a theoretical model which describes the structural dynamics of an oscillating foil to explain the observed trends in the experimental measurements.

1.7 Thesis Overview

Chapter 2 describes the experimental method and apparatus used in the study. The set up and operation of the flow facility, motion control system, force measurement apparatus and photographic equipment are all discussed. The procedure for the calculation of the thrust coefficient and efficiency from the force and position measurements is explained. The uncertainty in the measurements and derived quantities is also examined.

Chapter 3 discusses the design and construction of the foils used in the propulsion testing experiments. The foils are characterized in terms of resonant frequency and bending stiffness. In the final section of the chapter, a theoretical model is developed to represent the structure of the foils and describe the dynamic deformation of this structure in response to inputs of varying frequencies.

Chapter 4 presents the results of the experiments. The chapter begins by discussing how the foil deformation can be observed indirectly from torque measurements. The parameters of the theoretical model developed in Chapter 3 are then determined empirically by fitting the model predictions to the observed deformation behaviour. Subsequent sections of the chapter use this model to explain the observed trends in propulsive performance as the oscillation kinematics and foil structure are varied. Finally, the last section of the chapter discusses the implications of the findings for the design of practical propulsion systems.

Chapter 5 summarizes the work described in the thesis and identifies potential future investigations which build on the present results.

Chapter 2

Experimental Propulsion Testing Apparatus and Procedure

The main focus of the work described in this thesis was a series of experiments conducted to assess the effect of the foil structural design and the oscillation kinematics on the propulsive performance as measured by the thrust generation and efficiency. Conceptually, the procedure for these experiments was simple; flexible foils with a range of bending stiffness and inertia were immersed in water channel and driven in a oscillating motion using servo motors while the forces and torque applied to the foils were measured using a load cell and recorded. The thrust, power and efficiency were then calculated from the recorded force measurements and motion profiles to enable quantitative comparisons of the propulsive performance among the various trials. A sketch of the experimental set-up is shown in Figure 2.1. In addition to the force measurements, the foil deformation was observed by high-speed photography.

This chapter describes in detail the equipment and methods used in the propulsive performance trials. The first two sections describe the equipment and methods used to establish the kinematic conditions of the relative flow equivalent to forward travel and the oscillating motion. Sections 2.3 and 2.4 present the measurement of the applied forces on the foil and the foil deformation respectively. Section 2.5 examines the calculation of the thrust coefficient, power coefficient and efficiency from the experimental measurements. While the error in the individual position and force measurements are discussed along with the descriptions of the relevant equipment in Sections 2.2 and 2.3, the uncertainty in the calculated quantities is assessed separately in Section 2.6.

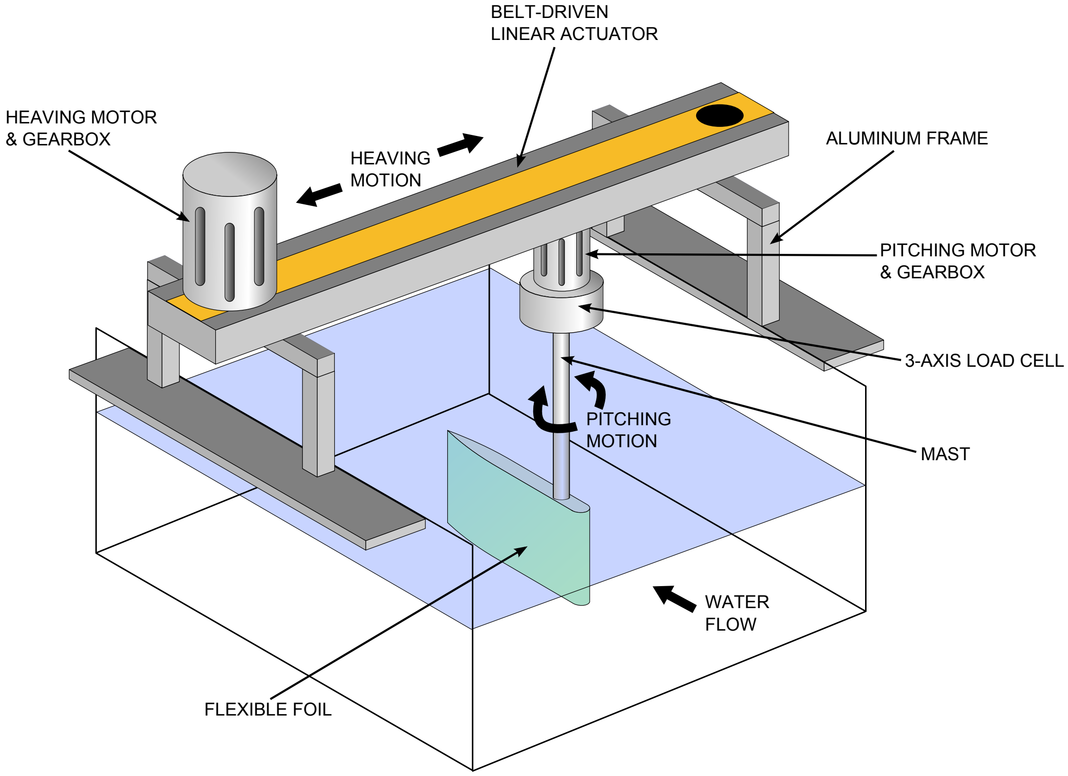

Figure 2.1: Sketch of the experimental set-up used to measure the propulsive performance of the oscillating foils.

2.1 Flow System

The experiments described in this thesis were conducted in the flow visualization water tunnel in the Department of Mechanical Engineering's Fluid Dynamics Laboratory at the University of Victoria. This water tunnel is a commercially available model produced by Engineering Laboratory Design Inc. The tunnel is of a re-circulating design, generating a continuous flow in the test section by drawing fluid from the outlet and reintroducing it at the inlet. The flow is driven by a pump powered by a large 25 HP motor. The flow speed in the test section can be adjusted using a variable frequency drive which controls the rotational speed of the pump.

The tunnel test section is constructed of transparent acrylic panels making up the sidewalls and bottom. During the experiments in this study, the upper surface of the test section was left uncovered, creating a free-surface flow. The test section has a length of 2.5 m and width of 45 cm. The tunnel was filled to its maximum depth of 45 cm to create a flow with a square cross-section. A large converging nozzle and a tank filled with honeycombs are situated upstream of the test section between the pump and the test section inlet. At the outlet, a vaned diffuser guides the fluid into the pipe which returns it to the pump. The nozzle, honeycombs and diffuser act to establish a uniform flow in the test section.

2.2 Control and Actuation of the Oscillating Motion

The flapping motions required for the study were generated using a servo motor motion system supplied by Parker Hannifin Corporation (Electromechanical Automation Division). A timing belt-driven linear actuator (Parker OSPE32-600L2-00680-PM2A6C) powered by a 1.756 kW motor was used to generate the heaving motion. A smaller motor (Parker SM233AE-NPSN) mounted on the carriage of the actuator was used to rotate the foils through a gear drive (Parker RX60-010-S2), generating a pitching motion. Both motors were powered using Parker Aries series digital servo drives (Parker AR-XXAE). The motors and actuators were mounted above the water tunnel, supported by an aluminum frame. The load cell used for force and torque measurements was mounted on the output shaft of the pitching gear drive. The foils were in turn connected to the load cell by a stainless steel mast.

The motion was controlled using a Parker ACR9000 controller. The motion profiles were prescribed using the cam table feature of the AcroBASIC programming language employed by the controller. This feature allows the user to input a table containing an arbitrary set of position points to which the controller will command the actuators to move at regular intervals in time. The motion is repeated by cycling through all of the points on the table for a prescribed number of times. For the experiments in this study, the motion profiles were sinusoidal so the cam tables consisted of one period of a sine wave discretized into one hundred points. The frequency of the motion was varied by changing the time period required to complete one cycle of the table. The sine waves were set to start at the negative peak where the velocity is zero so that infinite acceleration would not be required when the motion started from rest. To reduce the jerk when starting and stopping the motion, the amplitude of the motion was ramped up or down linearly over twenty cycles at the start or end of the trials. In addition to the ramping, twenty cycles were performed at the full amplitude before any data was taken to allow the flow conditions and the forces on the foil to arrive at a state of periodic oscillations.

The controller operated in servo mode, using a feedback control strategy to adjust the motor torque as necessary such that the actuators would accurately follow the commanded motion profile. During the operation of the system, the actual positions of each axis were measured using incremental optical encoders mounted on the motor shafts. The control signals were generated by multiplying the error between the commanded and measured positions by a gain factor. A component proportional to the derivative of this error was also added to the signal. The drives adjusted the current powering the motors based on this control signal. The appropriate servo gains were determined empirically using a step tuning procedure. In this process, the motor is commanded to move instantaneously through a small step of 400 encoder counts. The response of the motor is not instant, and the actual position of the actuator approaches the commanded position over time. The proportional and derivative gains are adjusted until the actuator is observed to move to the commanded position as rapidly as possible with no oscillations. With the chosen gains, peak following errors between the commanded and actual positions during trials with combined heaving and pitching motion were found to be on the order of 0.396 mm on the heave axis and 0.144°on the pitch axis. The following error was found to generally increase with the frequency of the motion but was relatively insensitive to the inertia of the foil.

The controller was also used to log the actual position of the linear actuator carriage and pitching gearbox shaft based on the encoder feedback during the experiments. This data was used in combination with the force measurements to calculate the power input (see Section 2.5). The controller was set to record the position every 3 ms which resulted in a minimum of 111 data points per cycle throughout the range of frequencies considered in the propulsion trials.

2.2.1 Uncertainty in the Position Measurements

The position records are subject to some uncertainty due to the limitations of the actuator mechanics and measurement hardware. Errors in these measurements arise due to the repeatability limitation of the linear actuator, backlash in the gear drives and the finite resolution of the encoders. The repeatability specification of the linear actuator refers to the ability of the device to repeat motions to within a certain precision limit. It is believed that the error arises due to factors such as non-uniformity in the timing belt and sprocket teeth, eccentricity of the drive pulleys and shafts, and play or looseness in the rotary and linear bearings. Backlash refers to the ability of the output shaft of a gearbox to rotate through some small angle without any movement of the input shaft. This relative motion is possible due to clearance between the gear teeth and a small amount of deformation of the internal components. The resolution of the optical encoders is finite because these measurement devices operate by counting pulses of light which pass through a grating that rotates with the motor shaft. The smallest movement of the motor shafts which can be detected therefore corresponds to the angular increment between successive openings in the grating. The error expected from each of these sources for both axes has been tabulated in Table 2.1. The errors from each source have been combined using a root-sum-square (RSS) method [35] to estimate the overall uncertainty in the position measurements. It is expected that there is an additional small amount of error due to flexing of the frame supporting the motion system and bending of the mast and couplings which connect it to the foils. However, this error is likely small because the framework and mast were constructed to be rigid considering the loads and forcing frequencies in the experiments.

Error Source	**Linear Axis**	**Rotary Axis**
Repeatability	±0.05mm	not applicable
Backlash	±0.111mm	±0.333°
Encoder resolution	±0.006mm	±0.009°
Overall error	±0.122mm	±0.333°

Table 2.1: Contributions from relevant error sources and overall uncertainty in the measurement of linear and angular positions.

2.3 Dynamic Force Measurement

A three-axis load cell supplied by Novatech Measurements Ltd. (Novatech F233-Z3712) was used to measure the force and torque applied to flexible foils during the trials. In general, load cells are force transducers consisting of foil strain gauges bonded to the surface of a metallic structure. When loads are applied to the structure, it deforms and stretches or compresses the strain gauges, causing a change in their electrical resistance. A Wheatstone bridge circuit is used to output a voltage proportional to this change in resistance which is in turn proportional to the applied load [36]. In this particular load cell, the metallic structure is an arrangement of cantilevered beams which bend in different directions depending on the applied loading. The bridge circuit for each force direction or torque uses an active strain gauge in each arm to compensate for temperature effects [37] and the resistance of the leads connecting the load cell to the supply voltage and measurement hardware [36].

The load cell was positioned to measure the torque about the pitching axis and forces in two orthogonal directions perpendicular to the foil span. One of the force axes was oriented to be aligned with the foil chord when the foil was in its undeformed shape. The foils were positioned such that the mid-span location along the pitching axis coincided with the factory-calibrated force center. Because this force center is situated 335 mm from the attachment point on the load cell, the foils were connected to the load cell using a stainless steel mast of 19.1 mm (0.75 inch) diameter. With the foils positioned in the water tunnel with the mid-span plane at the mid-depth of the test section, the mast protruded above the free surface allowing the load cell to remain above the water where it would not disturb the flow.

In the chosen experimental configuration, manufacturing errors resulting in asymmetry of the foil structure or imperfect alignment of the set-up had the potential to introduce a bias into the force measurements. This error would arise if the foils were positioned to direct a component of the weight or buoyant forces along one of the force axes of the load cell or generate a moment about the torque axis. To correct for this possibility, an initial load cell reading was taken for each foil when it was mounted motionlessly in the water tunnel under no-flow conditions. This reading was subtracted from all of the measurements during the propulsion trials to tare the load cell for the given foil design.

A set of Mantracourt Electronics SGA/A load cell amplifiers also supplied by Novatech Measurements Ltd. were used to boost the output of the load cell from a signal on the order of millivolts to a ±10 V scale. This amplification served to increase the signal-to-noise ratio in the measurements. These amplifiers also supplied the excitation voltage for the load cell. The load cell was factory calibrated about three months before the completion of the propulsion trials and the amplifier gains were also set during this procedure.

A National Instruments NI-PXI4472 analog-to-digital converter (ADC) was used to record the amplifier outputs at a sample rate of 10 kHz. This device is a delta-sigma converter which incorporates analog and digital low-pass filters to avoid aliasing in the digital records [38]. In this design, the conversion is performed in two stages. In the first stage, the signal input to the converter passes through a low-pass analog filter with a cutoff frequency of 400 kHz to remove high-frequency components which could cause aliasing in the conversion. A low-resolution one bit conversion is then performed on the filtered signal at a high sampling rate of 1.28 MHz. In the second stage, the output of the one bit conversion is passed through a digital filter which removes signal components above the Nyquist frequency for the sampling rate of the final output. This second low-pass filtering also removes the quantization noise added in the first conversion, which is uncorrelated with the original signal and restricted to frequencies well above the Nyquist frequency. The digital filtering calculations are performed to 24-bit precision to give the final conversion.

In order to use the force measurements for the calculation of the propulsive performance metrics (see Section 2.5), it was necessary to synchronize the sampling with the position records stored in the controller (see Section 2.2). To achieve this synchronization, the controller was programmed to send a triggering signal from one of its general purpose outputs at the correct time during the trial to begin recording data. Because of the relatively long (2 ms) turn-on time for these opto-isolated outputs [39], the triggering signal was treated as an analog rather than digital output. The trigger signal was connected to one of the input channels of the ADC which was dedicated for analog edge triggering. The trigger signal was also routed back to the trigger inputs on the controller which have a turn-on time of 400 ns [39] to initiate the position recording. By adjusting the threshold voltage for the analog trigger of the ADC to the appropriate level, it was possible to reliably synchronize the force and position recording to within 0.5 ms. At the maximum oscillation frequency considered in the trials, this difference corresponds to 0.15% of an oscillation period. The relatively high sampling rate for the force measurements was chosen in order to precisely identify the time when the analog triggering signal crossed the threshold level.

The sampling rates of the ADC as well as the triggering parameters are software configurable. A program was developed using National Instruments Corporation's Labview software to set the appropriate options and control the instrument during the experiments.

2.3.1 Post-processing of the Force Measurement Signals

Because the forces were recorded at a much higher sampling rate than the foil position, it was necessary to decimate the force records to have the same interval between samples for both quantities. This process reduced the effective sampling rate of the force signals from 10 kHz to 333 Hz. To avoid aliasing in the decimated force records, digital low-pass filtering was performed on the complete records before extracting data points in the decimation process. It was decided to implement this filtering digitally after taking the measurements rather than incorporating an analog filter into the measurement system because of the greater flexibility in terms of cutoff frequencies and filter topologies available with digital filters. Second-order Butterworth filters were eventually chosen because this topology does not have any ripple in the amplification or attenuation of the signal in the passband [40]. Because it is important to maintain the synchronization of the force and position measurements, it was decided to implement a zero-phase filtering strategy which allows the features of the filtered signal to remain at the same location in time as in the original measurements. In this approach, the software performing the filtering calculations applies the filter once, reverses the ordering of the data points, and then applies the filter to the reversed sequence [41]. The original ordering is then restored to the data points. Because the ordering of the data points is reversed between the two filtering operations, the phase shifts caused by each filter are in opposite directions and cancel each other. Because the filter is applied two times in total, the attenuation factors applied to the amplitude of the signal are squared and the order of the filter is doubled. The filtering applied in this study was therefore in fact effectively fourth-order. The filtering routines were implemented using built-in functions in The Mathworks's Matlab software.

The digital filtering process was also used to remove high-frequency fluctuations in the signals. These components of the force and torque recordings were not believed to be related to any interesting physical phenomena in the fluid flow or foil deformation. Instead this noise was attributed in part to electromagnetic and thermal effects on the equipment. The servo-loop control strategy employed for the motion equipment was also believed to cause fluctuations in the torque of the motors which would in turn introduce additional oscillations into the measurements. Setting the cutoff frequencies of the digital filters a factor of ten times above the oscillation frequency for each trial was found to be generally effective at removing this noise and is believed to have had a minimal effect on the relevant low-frequency components.

Examples of filtered and unfiltered force signals acquired during trials at oscillation frequencies of 0.59 Hz and 1.17 Hz are shown in Figures 2.2 and 2.3 respectively. These trials did not include an active pitching motion and the x- and y-axes of the load cell remained aligned with the streamwise and transverse directions respectively. In the case of the low-frequency oscillations at 0.59 Hz, the streamwise force is small and the signal-to-noise ratio is very poor. This inability to precisely resolve the streamwise force limits the accuracy of the calculated thrust and efficiency data for the low-frequency trials. However, a periodic signal can be discerned more clearly from the measurements in the trial with a 1.17 Hz oscillation frequency, and also at higher frequencies where the interesting performance trends occur. The transverse force and torque are also subject to some noise but can be measured more clearly in both trials.

2.3.2 Uncertainty in the Force Measurements

The load cell measurements are subject to errors arising from non-linearity, cross talk, hysteresis and repeatability [42–44]. The contribution of each of these error sources can be estimated based on the data obtained during calibration when known loads were applied. Non-linearity errors arise due to the fact that the output voltage of the load cell in response to applied loads is not strictly linear, while the scaling from voltage to force or torque is made based on linear interpolations between the calibration data points. One of the most significant error sources for multi-axis load cells is cross talk. This error is defined as the offset between the measurement and the true load on one axis which occurs when load is applied on one of the other axes. Ideally, the axes would operate completely independently by either designing the structure such that no loads can be transmitted from one axis to another, or constructing the bridge circuits such that resistance changes in the strain gauges used for one axis would cancel each other when an off-axis load is applied. Such perfect operation can never be achieved in practice due to manufacturing errors such as the gauge alignment or asymmetry of the structure. In addition to these two bias errors, further errors will limit the precision of measurements made when applying the same load repeatedly. The load cell has a specified repeatability limit which is obtained by observing the difference in output between consecutive applications of the full rated load. Strain gauge load cells are also known to be subject to a hysteresis error, defined as the difference between the output voltages obtained when the same force or torque is applied under conditions of increasing or decreasing load.

The estimated errors for each axis due to the sources identified here are tabulated in Table 2.2. The individual error sources have been combined using an RSS method [35] to give an overall uncertainty in the measurements. In each case, it is observed that cross talk is the dominant error source.

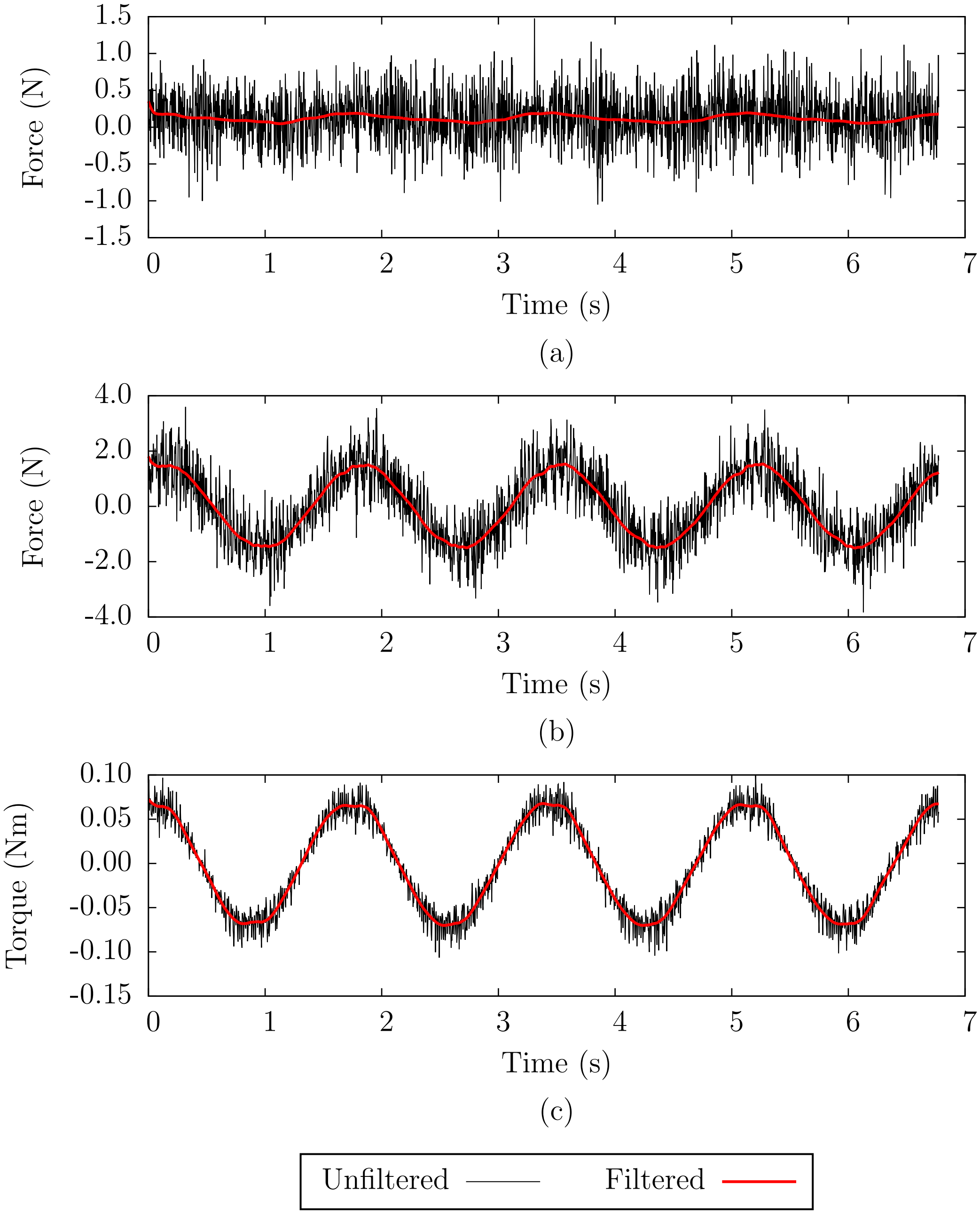

(a)

(b)

(c)

Figure 2.2: Signals recorded from the load cell (a) x-axis, (b) y-axis and (c) torque axis during a propulsion trial with an oscillation frequency of 0.59 Hz and heave amplitude of 25 mm.

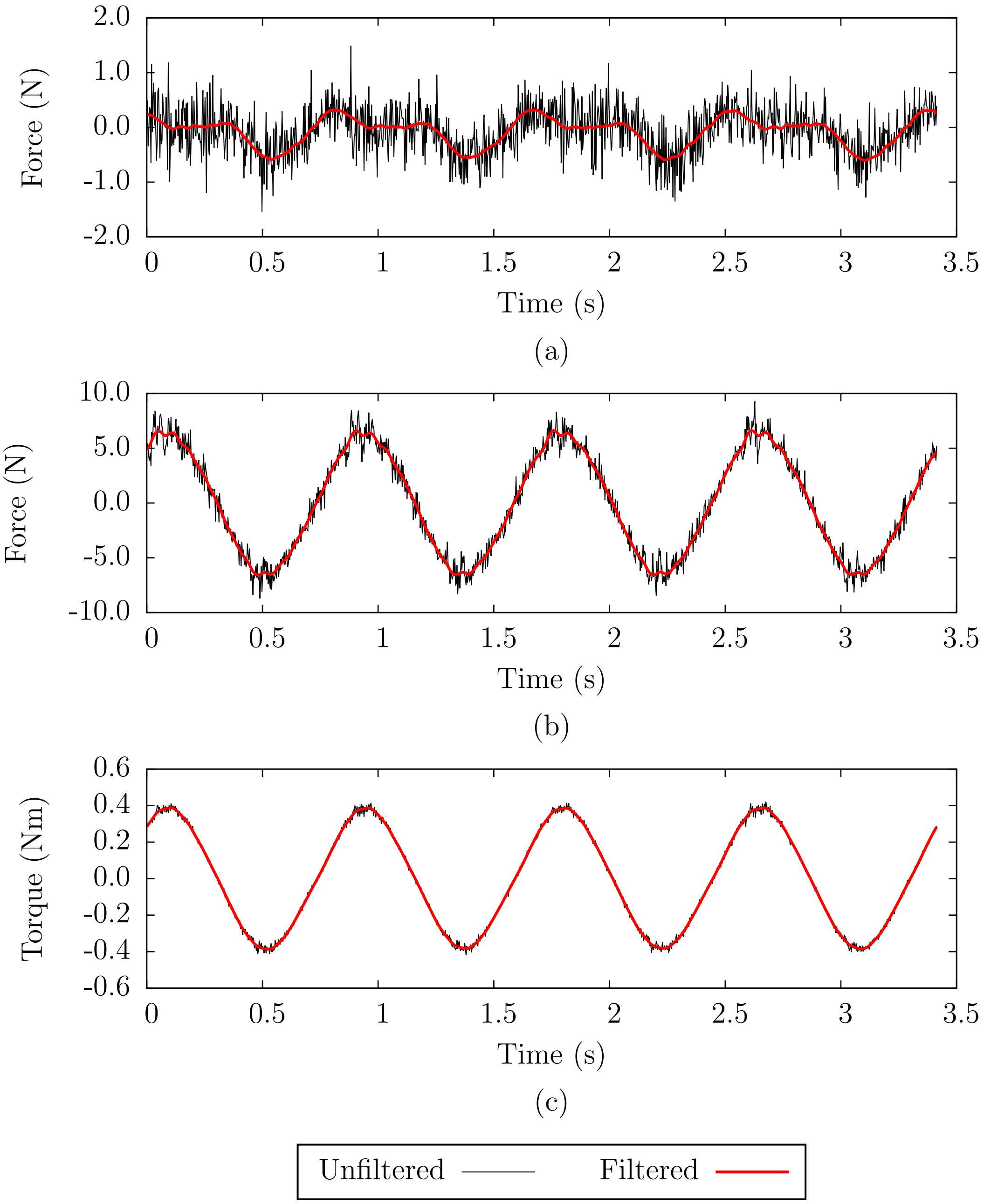

Figure 2.3: Signals recorded from the load cell (a) x-axis, (b) y-axis and (c) torque axis during a propulsion trial with an oscillation frequency of 1.17 Hz and heave amplitude of 25 mm.

Error Source	**x-axis**	**y-axis**	**torque axis**
Non-linearity	±0.19 N	±0.60 N	±0.0036 Nm
Cross talk	±2.6 N	±4.6 N	±0.36 Nm
Repeatability	±0.07 N	±0.05 N	±0.007 Nm
Hysteresis	±0.16 N	±0.27 N	±0.012 Nm
Overall error	±2.6 N	±4.6 N	±0.36 Nm

Table 2.2: Contributions of relevant error sources and overall uncertainty in the load cell measurements on each axis.

The uncertainties listed for each axis in Table 2.2 likely represent a very conservative estimate. The non-linearity and hysteresis errors were obtained by comparing the measured outputs at half of the rated load to the output predicted by a linear interpolation over the full load range. In the actual trials, the interpolations were made between all three of these calibrated load points. When interpolating over a smaller range, the linear trends will more accurately represent the actual response of the load cell. Additionally, it is reasonable to expect that non-linearity and hysteresis errors will be greater near the midpoints of the load range. Small forces near the zero load point will likely be subject to smaller errors from these sources. It is assumed that the cross talk specifications for the load cell were obtained by applying the maximum rated load on one axis and observing the output on the other two. Since the forces and torques applied during the propulsion trials were considerably smaller than the rated loads, it is reasonable to expect that the cross talk errors would also be proportionally smaller. Based on this discussion, it may be more reasonable to remove the non-linearity, hysteresis and cross talk errors and consider only the repeatability specification for the relatively low forces and torque which were measured in the propulsion trials. In this case, the overall uncertainty is much lower.

Errors in the force and torque measurements arising from the quantization in the ADC and from the dynamic response of the load cell are not believed to be significant and have been omitted from the discussion here. The high bit count of the ADC makes quantization errors small relative to the other sources identified in Table 2.2. The error due to the dynamic response of the load cell is also minor because the frequencies of the applied forces were less than one tenth of the resonant frequencies of the force measurement system [45]. An estimate of these resonant frequencies is included in Appendix A.

2.4 Photographic Observation of the Foil Deformation

During some propulsion trials, digital photographs were recorded to directly observe the degree of chordwise bending of the foils and the phase of this deformation with respect to the input motion. A Photron APX-RS high-speed digital camera fitted with a Nikon Nikorr AF-series 28 mm lens was positioned below the test section of the water tunnel looking up at the flexible foil through the transparent acrylic floor. The lens focal ratio was set to f/2.8 and the camera was configured to record at 500 frames per second. The frame rate was chosen to be much higher than the oscillation frequencies to avoid aliasing in the observed deformation patterns and to reduce the blurring of the moving foil in recorded images. The camera shutter speed was left to be selected automatically by the Photron FastCam Viewer software which was used to control and configure the camera. The lens was focused on the plane at the lower end of the foil span, approximately 0.4 m above the front surface of the lens. The camera was mounted on a Manfrotto three-axis tripod head which was used to rotate the camera such that the edges of the field of view were aligned to be parallel and perpendicular to the streamwise direction. With the chosen camera position and the viewing angle provided by the 28 mm lens, the chord length of the foil occupied almost the entire length of the field of view, allowing the movement and deformation of the foil to be observed with the maximum possible resolution on the 1024×1024 pixel sensor of the camera.

Sheets of corrugated cardboard with a black paper covering were placed spanning the water tunnel test section above the water free surface to create a dark background in the photographs. The overhead lighting in the laboratory was switched off during these trials. Illumination for the photographs was provided by a standard 60 W incandescent light bulb mounted in a small desk lamp placed beside the test section at the approximate height of the mid-span of the foil. The lamp was located approximately 0.06 m from the outside wall of the tunnel and oriented to direct the light at an angle slightly downstream. The precise positioning of the light was adjusted separately for each trial to establish a high contrast between the foil and the dark background in the photographs. The arrangement of photographic and lighting equipment is illustrated in Figure 2.4.

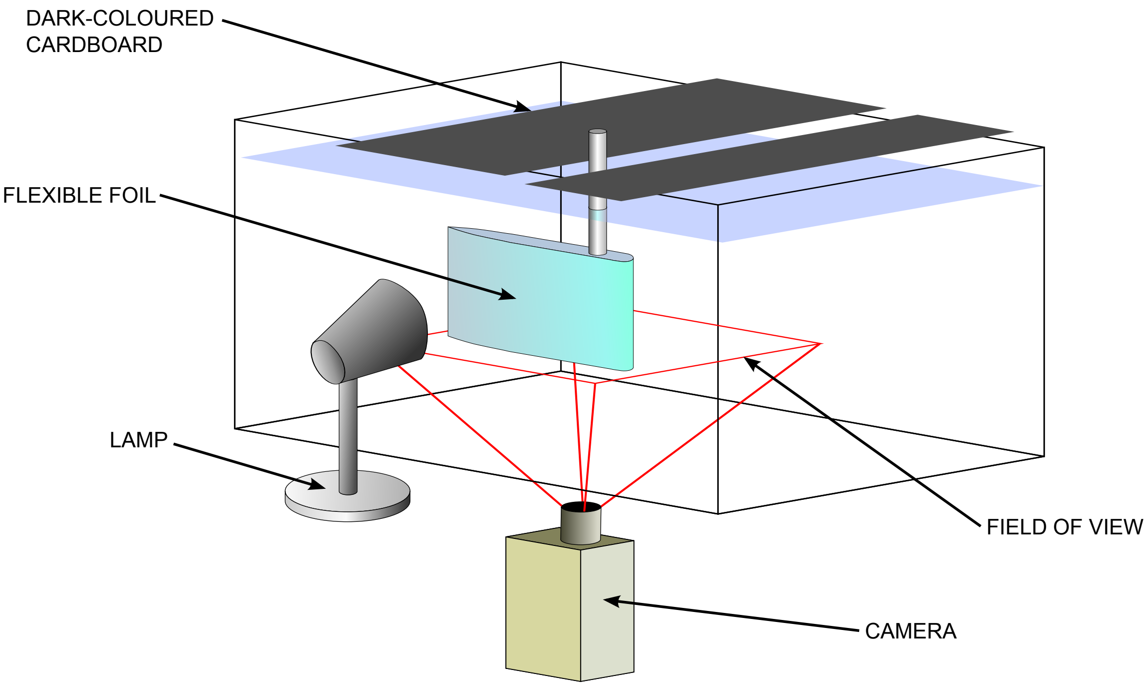

Figure 2.4: Set-up of photographic and lighting equipment for observation of the foil deformation.

Since the silicone rubber material from which foils were constructed is of a translucent white or light gray colour, the chosen combination of lighting and photographic settings resulted in a distinct contrast in the light intensity between the foil and the dark background in the recorded images. This contrast is desirable since it makes it possible to determine the foil position using computerized edge-detection methods such as the Canny algorithm included with Matlab. This algorithm first calculates the intensity gradient throughout the image using the derivative of a Gaussian filter. Pixels with local maxima in the intensity gradient are designated as edge pixels. Two threshold operations of different levels are then applied to trace object contours. In the first operation, edge pixels with an intensity gradient above the upper threshold are marked as "strong" edges and form an initial set of contours. In the second operation, "weak" edge pixels with an intensity gradient between the low and high threshold levels are added to the contours if connected by a continuous line to the strong edges. By using the two thresholds, the algorithm is better able to produce continuous contours while rejecting false edges than other edge detection algorithms which only apply a single threshold [41]. In the selection of the Canny algorithm settings, the Gaussian filter standard deviation was set to $\sqrt{2}$, the default value used by Matlab. The high threshold value corresponding to strong edges was set to 0.25

and the low threshold value 0.025. Both thresholds are measured on a normalized scale from 0 to 1, where 1 is the highest intensity gradient in the image [41]. The chosen low and high threshold values allowed the algorithm to trace a distinct contour around the foil while largely rejecting other potential edges which arise due to dust or roughness on the foil surface or any shadows and reflections creating non-uniform lighting in the background of the image. A typical photograph of a foil and the resulting contours from the edge detection algorithm are shown in Figure 2.5.

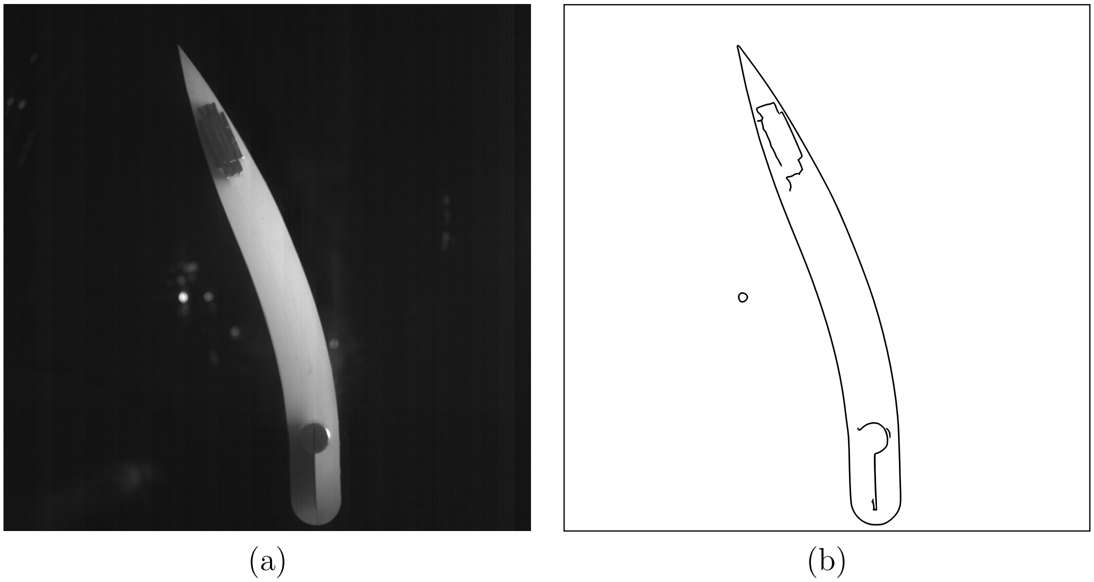

(a) (b)

Figure 2.5: Examples of (a) a typical photograph of a dynamically deforming foil and (b) the result after processing the photograph using the Canny edge detection algorithm.

After outlining the foil with the edge detection algorithm, it was necessary track specific points on the contour between acquired images in order to observe the movement and deformation. The chosen points for this purpose were the trailing edge and the pitching axis, where the foil does not bend appreciably and remains aligned with the measured heaving position. The identification of the trailing edge position was straightforward since this point could be located by simply selecting the furthest downstream point on the foil contour. The trailing edge was therefore located by searching from left to right and moving down the rows of pixels until an edge pixel was found. In the cases where the furthest downstream row with valid edges contained more than one edge pixel, the average of the minimum and maximum index of the edge pixels was chosen as the transverse location of the trailing edge. The identification of the pitching axis position was somewhat more complicated. The foil designs incorporated an embedded aluminum rod running the length of the foil span, centred on the pitching axis. A sheet of stainless steel used to reinforce the leading edge area extended ahead of this rod (see Section 3.1). With the foils illuminated from the side, the rod appeared as a dark spot within the lighter foil region in the photographs, and the shadow of the stainless steel sheet darkened one side of the foil. The edge detection algorithm therefore traced the edge of the rod and the stainless steel sheet since the image intensity abruptly changed from light to dark along these contours. Since the videos were only recorded during trials with no active pitching motion in which the rod did not rotate, the furthest upstream point on the rod could be identified by selecting the point where the detected edge changed from the curved contour around the rod to a straight contour aligned with the streamwise direction defined by the stainless steel sheet. Because the rod was not rotating, this point also remained aligned at the same transverse position as the rod center which coincided with the pitching axis and the measured heaving position.

The repeatability of the observation of the foil position was tested by acquiring sets of ten images with the foil held in a constant position. In addition to the trailing edge and heave position, the leading edge of the foil was also tracked during these tests. Image sets were acquired for five different transverse positions. In all but one of the image sets, the pixel indices identified to represent the leading edge, trailing edge and heave position were consistent to within one pixel, suggesting that the precision of these observations is limited by the camera resolution rather than by random fluctuations such as vibrations resulting in relative movement between the camera and the foil or digital noise in the images. In one image set, the trailing edge transverse position was found to fluctuate by 1.5 pixels between images.

To calibrate the image scaling, the pixel displacement of the relevant points on the foil was observed from one image set to the next in the same five different positions used in the repeatability tests. The movement of the foil through these positions was actuated using the motion system described in Section 2.2, and the physical displacement of the foil between positions was therefore measurable using the motion system heaving encoder. Figure 2.6 shows the measured physical displacement plotted against the observed pixel shift of the heave position. The relation between the physical displacement and the observed pixel shift is apparently linear indicating that effects of optical distortion, non-uniform lighting, and non-uniform sensitivity of the camera sensor are minimal. A least-squares regression line was fit between the measured displacement and the observed pixel shifts to give scalings of 0.2036 mm/pixel for the trailing edge and 0.2052 mm/pixel for the heave position. The slight difference occurs because the end of the aluminum rod lies in a plane 5 mm above the lower end of the foil span.

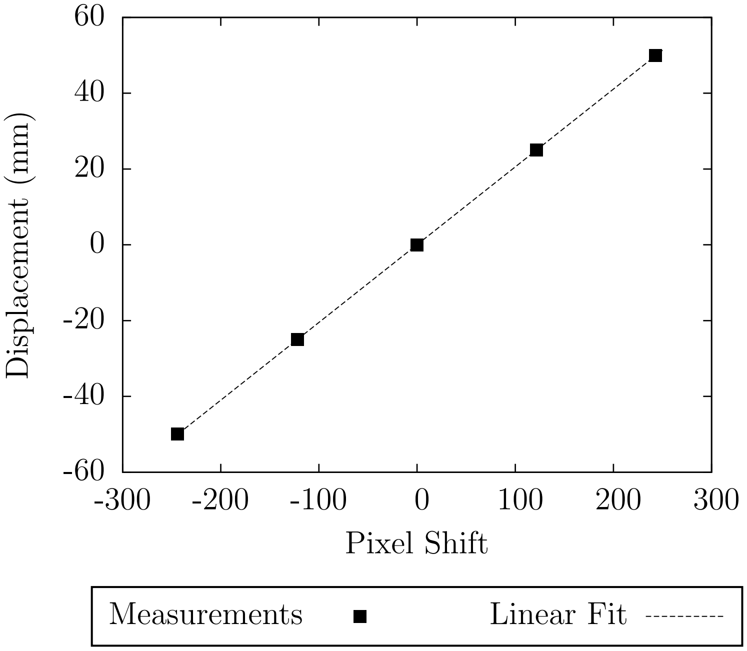

Figure 2.6: Measured displacement vs. observed pixel shift of the rod through the foil pitching axis.

When collecting photographic records of the propulsion trials, the foil motion and deformation were recorded over four complete cycles of the actuating motion. When processing these recordings to track the heave position and trailing edge, the algorithm occasionally detected incorrect edges resulting from reflections of entrapped air bubbles or waves on the free surface creating bright spots in the images. To reject these outlying data points, a sine wave was fitted to the recorded motion by selecting the dominant frequency component obtained from a Fourier transform of the records. Any data points outside of a band of ±10% of the amplitude of the fitted wave were rejected and replaced with the point on the wave at the corresponding time. After rejecting the outliers, second-order Butterworth filters were applied to the records using the same zero-phase filtering strategy as for the load cell measurements (see Section 2.3). These filters removed the remaining small-amplitude, high-frequency oscillations resulting from vibrations caused by the motion system and the repeatability limitations of the photographic observation. The foil deflection was then determined by subtracting the recorded trailing edge and heave positions. Examples of photographically recorded motions of the heave position and trailing edge are shown in Figure 2.7. The bands outside of which the data points were rejected are illustrated with dashed lines.

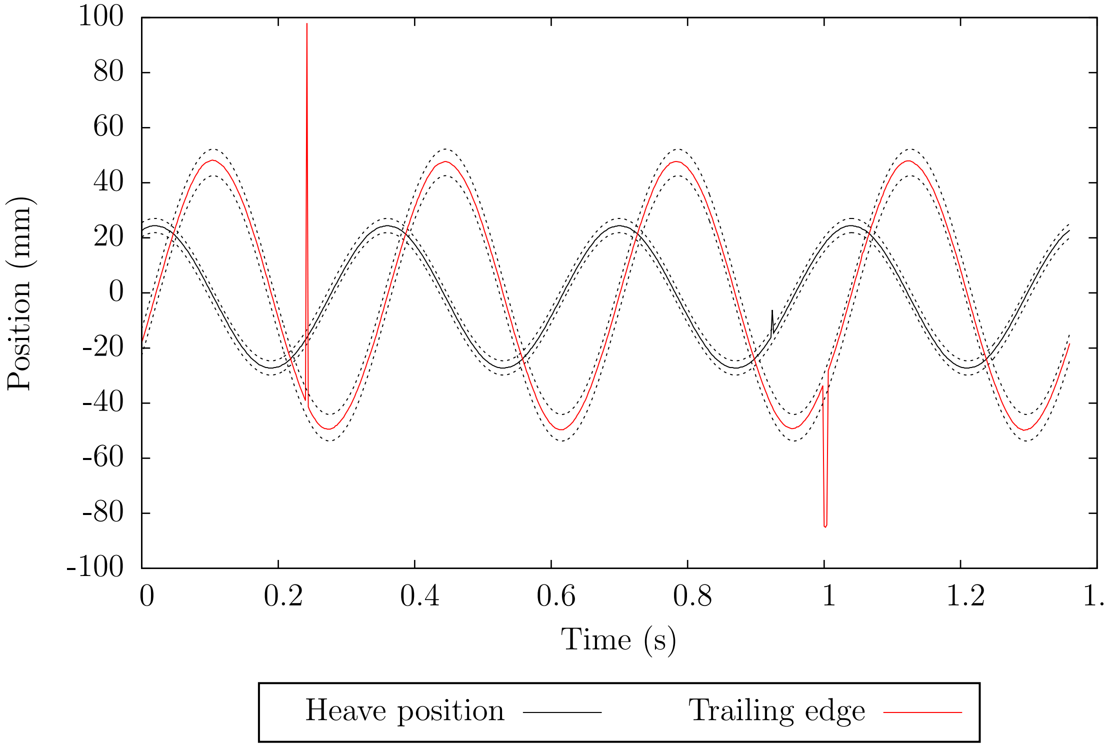

Figure 2.7: Recorded heaving and trailing edge positions throughout four motion cycles at 2.94 Hz. Any points outside of the dashed lines around the traces were rejected as outliers.

2.5 Calculation of Performance Parameters

In order to make comparisons between the propulsive performance of different foils and evaluate the potential use of a given foil design as a propulsion mechanism, it is useful to define dimensionless measures based on the time-averaged thrust generation and power requirements. These groupings are the thrust coefficient, power coefficient, and efficiency which have been defined in Section 1.1. The calculation of these quantities from the position and force measurements recorded during the propulsion trials is discussed here.

Because the load cell rotated with the foil during the trials which included an active pitching motion, the first step in the calculation of the dimensionless performance measures was to project the measured forces from a foil-based coordinate system onto the axes aligned with the flow and heaving motion in a fixed laboratory coordinate system. The directions defined for the forces and torque in each coordinate system are illustrated in Figure 2.8.

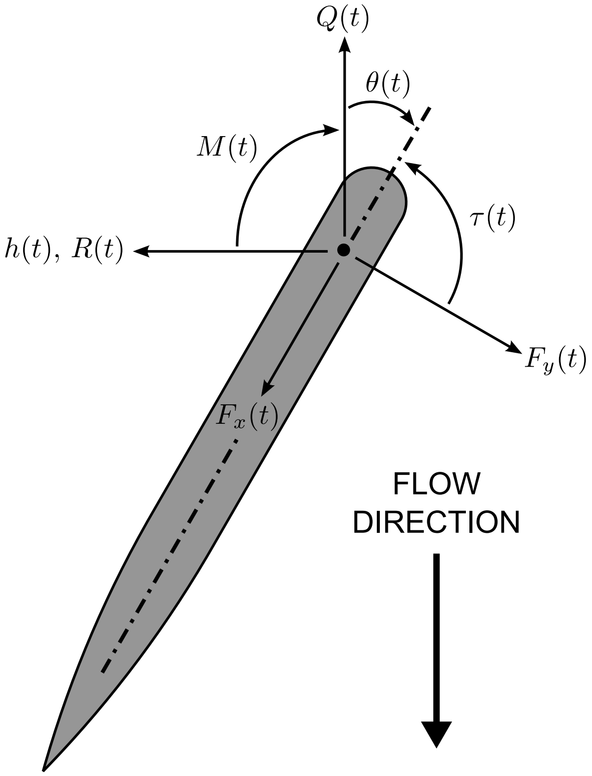

Figure 2.8: Defined directions of the load cell measurements, $F_x(t)$, $F_y(t)$ and $\tau(t)$; measured positions, $h(t)$ and $\theta(t)$; and projected forces and torque, $Q(t)$, $R(t)$ and $M(t)$ required for the thrust, power and efficiency calculation.

Inspection of Figure 2.8 shows that the relevant forces and torque in the fixed coordinate system are obtained from the load cell measurements using the geometric transformations given by Equations 2.1-2.3.

$$Q(t) = -F_x(t)\cos\theta(t) - F_y(t)\sin\theta(t) \tag{2.1}$$

$$R(t) = F_x(t)\sin\theta(t) - F_y(t)\cos\theta(t) \tag{2.2}$$

$$M(t) = -\tau(t) \tag{2.3}$$

Recalling the definition of the thrust coefficient, $C_T = \frac{Q}{\rho U^2 a}$, from Section 1.1, it is apparent that the only quantity in this expression which varies in time in the experimental configuration considered here is the thrust, Q. The time-averaged thrust coefficient is therefore obtained from

$$C_T = \frac{1}{\rho U^2 a} \frac{1}{nT} \int_0^{nT} Q(t) dt \tag{2.4}$$

where T is the oscillation period and n is the number of periods over which the time-average is computed [12]. In theory, the forces are expected to vary periodically with the oscillating motion and averaging the thrust over one cycle should be sufficient. However, to account for the repeatability of measurements in these experimental trials it was decided to take the averages over multiple periods (see Section 2.6).

To calculate the power coefficient, it is first necessary to obtain an expression for the instantaneous power input required to drive the foil in its oscillating motion:

$$P(t) = -R(t)\frac{dh}{dt} - M(t)\frac{d\theta}{dt} \tag{2.5}$$

To obtain the time-averaged power coefficient, Equation 2.5 is integrated over a number of cycles and then normalized in a manner similar to the thrust coefficient [12]:

$$C_P = \frac{1}{\rho U^3 a} \frac{1}{nT} \left[-\int_0^{nT} R(t)\frac{dh}{dt} dt - \int_0^{nT} M(t)\frac{d\theta}{dt} dt \right] \tag{2.6}$$

It can be noted that the differentiation with respect to time of the heave and pitch positions in the calculation of the instantaneous power (Equation 2.5) is cancelled by integration with respect to time in the calculation of the time-averaged power coefficient in Equation 2.6. The time-averaged power coefficient is therefore effectively obtained by integration of the lateral force and the pitch axis torque with respect to distance and angle respectively. This approach was adopted here in the calculation of power coefficient from the experimental data because the linear and angular positions were measured at each data point while the velocities were not. Evaluating the integral in this way removes the need to obtain the velocities by discrete differentiation of the measured positions.

In the experimental measurements, the forces, torque and positions are known as discrete data points rather than continuous functions of time. To use this data to approximate the integrals in Equations 2.4 and 2.6, trapezoidal quadrature was applied. Using this scheme, and recalling that the integration with respect to time in Equation 2.6 has been replaced with the equivalent integration in space, the expressions for the thrust and power coefficient become

$$C_T \cong \frac{1}{\rho U^2 a} \frac{1}{nN\Delta t} \sum_{i=1}^{nN-1} \frac{Q_i + Q_{i+1}}{2} \Delta t \tag{2.7}$$

and

$$\begin{aligned} C_P \cong \frac{1}{\rho U^3 a} \frac{1}{nN\Delta t} \Bigg[& - \sum_{i=1}^{nN-1} \frac{R_i + R_{i+1}}{2} (h_{i+1} - h_i) - \\ & \sum_{i=1}^{nN-1} \frac{M_i + M_{i+1}}{2} (\theta_{i+1} - \theta_i) \Bigg] \end{aligned} \tag{2.8}$$

respectively, where i is an index of the data points, N is the number of measurements taken during each cycle and Δt is the time interval between measurements.

Once the thrust and power coefficients have been calculated, it is straightforward to find the efficiency by recalling the definition from Section 1.1, $\eta = C_T/C_P$.

2.6 Uncertainty in the Derived Quantities

Because of the uncertainty in the measurements of position, force and torque, the calculated parameters are also subject to some error. Although the uncertainties associated with the measurements made using the motion system encoders and load cell have been quantified in Sections 2.2 and 2.3, it is difficult to relate these uncertainties to the resulting overall error in the derived quantities of thrust coefficient, power coefficient and efficiency. The approach suggested by Coleman and Steele [35] to combine the uncertainties from individual measurements using an RSS method is difficult to apply here because the sensitivity of the results to the measurements at each recorded point in the oscillation cycle would have to be calculated. The calculation is further complicated by the fact that in some cases the errors of multiple measurements are correlated. For example, if one of the motors on the motion system rotates in the same direction throughout the time interval between two position measurements, the bias error in each measurement resulting from backlash in the gearbox will be the same and the two errors will cancel when considering the incremental distance between these points. However, if the motor reverses the direction of the applied torque between measurement points, the incremental distance will be subject to this error so the effect of backlash can neither be included nor ignored consistently throughout the cyclic motion.

Because of the inherent difficulties in determining the overall uncertainties by combining the errors from individual measurements, it is more practical to instead estimate the uncertainty in the calculated quantities by comparing results obtained from measurements taken during different cycles. This approach has been used by Buchholz and Smits [19]. An estimate of the uncertainty obtained in this way will include the effect of precision errors, such as those that arise from the repeatability limitations of the actuators and instruments or random changes in the environmental conditions including turbulent fluctuations in the water tunnel flow. However, errors which result in a consistent bias in the results will not be reflected by the estimate. This bias may arise, for example, due to improper alignment of the foil in the tunnel resulting in a non-zero mean pitch angle, or a combined load which occurs periodically and produces a consistent cross talk error in the load cell measurements at some point during the oscillation cycle. To a certain extent, the bias error in the results is expected to be similar among the various propulsion trials with different foils and kinematic conditions since the same equipment is used in each case. Since the objective of these experiments is to compare the relative performance of the foils rather than to make predictions of the performance of a specific design in the field, a consistent bias error across the trials will have a limited effect on the interpretation of the results. For this reason, the estimate of the uncertainty in the results obtained by comparing the calculated performance over successive cycles is still useful even though the bias is not included.

Figure 2.9 shows the thrust coefficient, power coefficient and efficiency calculated over successive cycles for a single foil at one particular oscillation frequency. Although the values change from one cycle to the next, there is no apparent trend in the results with respect to time. This result indicates that a sufficient period of time has passed between the start of the motion and the recording such that the effects of initial conditions are not included.

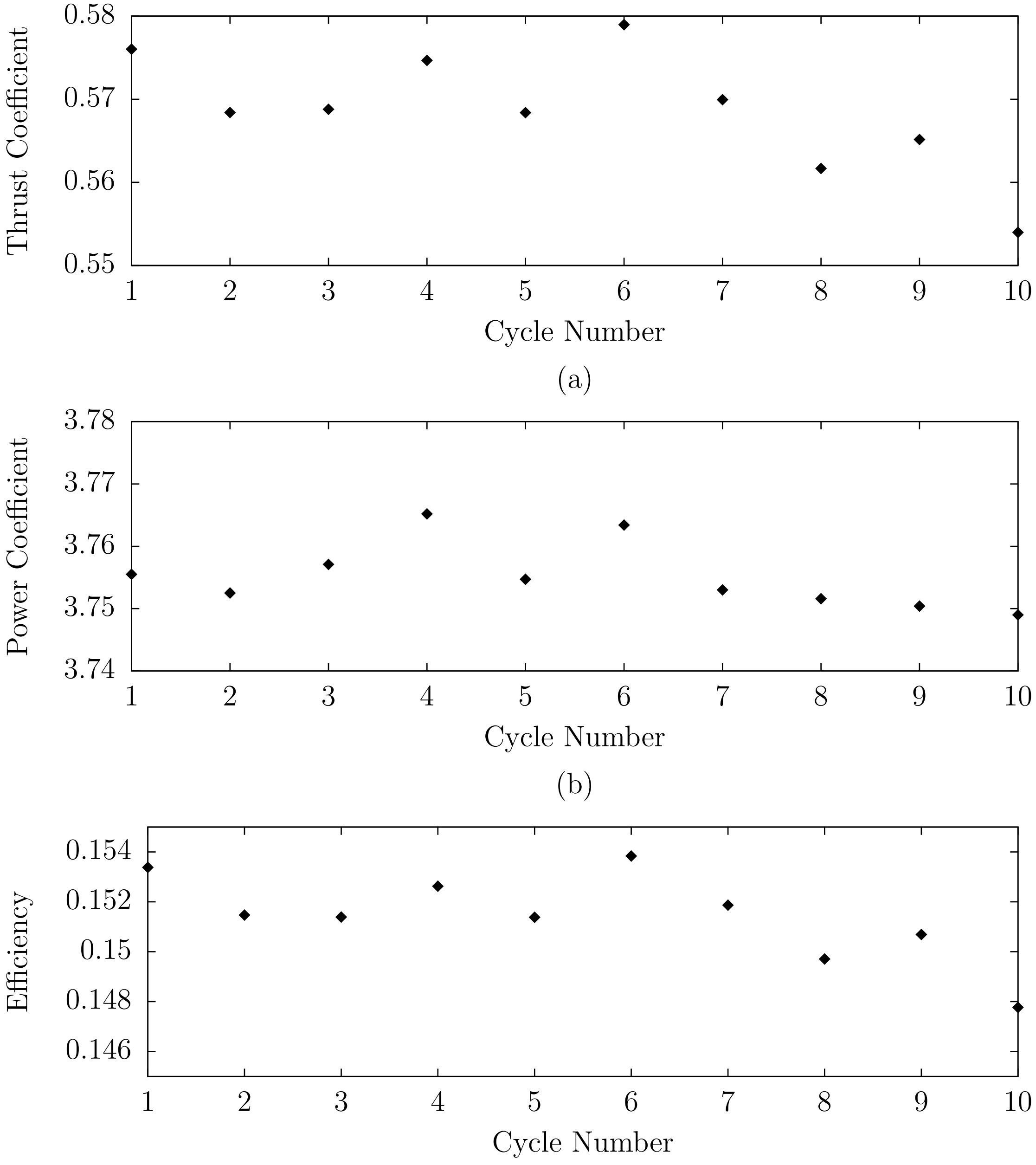

(a)

(b)

(c)

Figure 2.9: Cycle-averaged (a) thrust coefficient, (b) power coefficient and (c) efficiency calculated for ten consecutive oscillation cycles.

Since the differences in the performance parameters calculated during different cycles arise due to what are essentially random fluctuations, it is expected that in the limit of an infinite number of cycles, the quantities calculated from the measurements during individual cycles would fit a Gaussian distribution [35]. For the finite number of cycles considered here, it is therefore appropriate determine the uncertainty in the measured mean values of thrust coefficient, power coefficient and efficiency with respect to the true mean by assuming a t-distribution. In this case, the interval around the measured mean, $\pm P_{\overline{x}}$, within which the true mean is expected is given by [35]

$$P_{\overline{x}} = z\frac{S_x}{\sqrt{n}} \tag{2.9}$$

where S_x is the standard deviation within the sampled cycles and n is the number of cycles. The parameter z depends on the number of degrees of freedom in the sample, $n-1$, and the confidence level or probability with which it is expected to find the true mean within the interval. The specific value of z for a given number of degrees of freedom and confidence level can be obtained from published tables [35] or software such as Matlab.

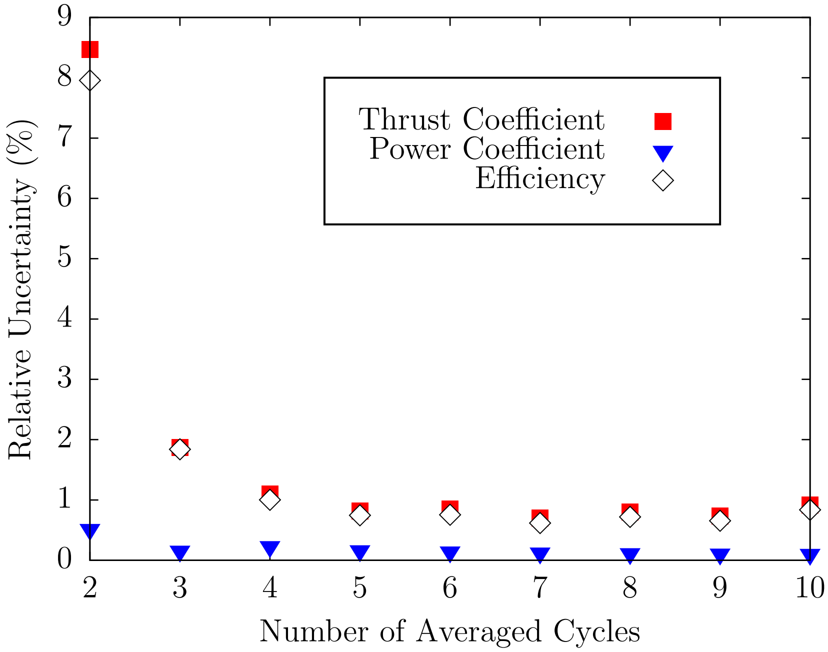

Figure 2.10: Variation in the relative uncertainty at the 95% confidence level with the number of cycles considered in the averaging of the thrust coefficient, power coefficient and efficiency.

In Figure 2.10, the relative uncertainties at 95% confidence in the estimates of the mean thrust coefficient, power coefficient and efficiency are plotted with respect to the number of cycles considered in the averaging. It is observed that the uncertainty in the thrust coefficient is much higher than that of the power coefficient, likely due to the relatively poor signal-to-noise ratio in the measurement of streamwise forces compared to transverse forces. This same error is also dominant in the calculation of the efficiency and the uncertainty of both quantities is approximately the same. It is found that by averaging over ten cycles, the relative uncertainty in the thrust coefficient and efficiency approach a level of approximately ±1% while the uncertainty in the power coefficient is lower. Based on this analysis, it was decided to compute the averages in the calculation of the performance parameters over ten cycles since the uncertainty apparently decreases rather slowly with respect to the number of cycles considered at this point.

Chapter 3

Construction and Characterisation of the Flexible Foils

The flexible foils tested in the propulsion trials allowed the parameters of foil stiffness and inertia to be varied between trials. A set of six foils was constructed, each having the same external geometry but different structural properties. The novel composite design of the foils included an internal stainless steel reinforcement to set the bending stiffness, a lead mass to set the resonant frequency and a silicone rubber encapsulant to form the external shape. This design is similar to models used by Heathcote et al. [30], but in that case the foils did not include an embedded mass and were constructed to have spanwise rather than chordwise flexibility. The foils used in this study are grouped into two categories, “A” and “B”, based on the design of the internal reinforcement. Each category included three foils with different amounts of embedded mass. The designs and structural properties of each of these foils are described in Table 3.1.

While the foil properties pertinent to this study have been summarized in Table 3.1, the foil design and the measurement of the structural properties are explained in more detail in the sections of this chapter. Section 3.1 describes the geometry of both the external shape and the internal structure. Section 3.2 discusses the fabrication process used to encapsulate the metal structure within the silicone rubber body. Sections 3.3 and 3.4 examine the characterization of the foils by the measurement of resonant frequency and bending stiffness respectively. In Section 3.5 a theoretical model is developed to relate the dynamic bending behaviour to the mass, stiffness and damping of the foil structures.

Foil Name	**Reinforcement**	**Embedded Mass (g)**	**Stiffness (N/m)**	**Resonant Frequency (Hz)**
A1	stainless steel sheet - full chord length	0	142	3.08
A2	stainless steel sheet - full chord length	140	168	2.77
A3	stainless steel sheet - full chord length	383	171	2.57
B1	stainless steel sheet - leading edge area only	0	125	2.81
B2	stainless steel sheet - leading edge area only	147	131	2.57
B3	stainless steel sheet - leading edge area only	384	105	2.26

Table 3.1: Nomenclature and design summary for the foils used in the experimental propulsion testing.

3.1 Structure and Geometry

The foils used in this study were composite structures made up of internal metal components to give the desired stiffness and mass properties encapsulated in a flexible rubber body to give the final shape. The foil chord length was 200 mm and the span was 140 mm. In profile, the foils had a rectangular cross-section 20 mm thick occupying 110 mm of the chord length. The foils tapered in circular arcs at the leading and trailing edges. The leading edge had a semi-circular profile and tapered in an arc with a radius of 10 mm. The radius of the arc at the trailing edge was 325 mm so that the arc began tangent to the side of the rectangular portion of the profile and ended in a sharp point at the trailing edge. The foil profile geometry is illustrated in Figure 3.1. This rather unusual profile was chosen over standard designs such as symmetric NACA 00XX profiles to allow for a greater thickness close to the trailing edge where the weight was embedded.

The internal metal structure of the foils served to modulate properties of bending stiffness and resonant frequency and also provided an attachment point for the foils to the drive system. The structures generally consisted of an aluminum rod, a reinforcing stainless steel sheet and a lead weight. With the exception of the weights, all of the internal metal components described here were fabricated in the UVic Mechanical

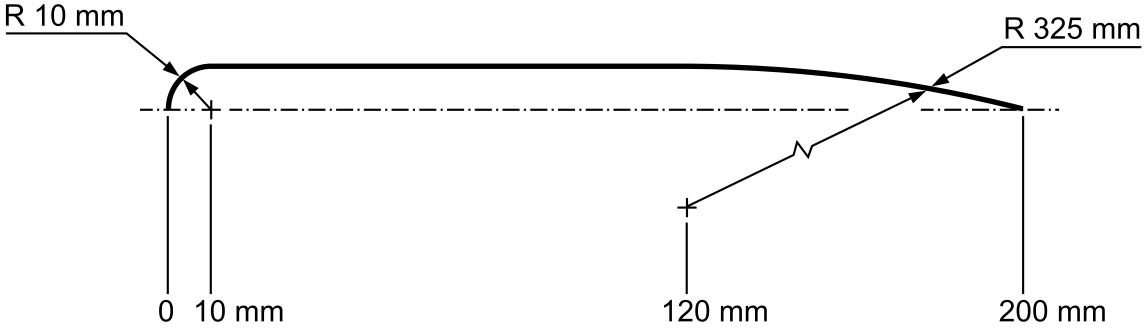

Figure 3.1: Foil half-profile showing the dimensions and placement of the circular arcs which taper the leading and trailing edges.

Engineering machine shop.

The aluminum rods served to transfer the force and torque from the drive system onto the foil and prevent flexing the spanwise direction. The 12.7 mm (0.5 inch) diameter rod ran along the foil span centered at location 33.7 mm back from the leading edge. Placing the rod in this position left 160 mm of the foil chord extending behind the rod in a cantilevered arrangement. The rod was assembled from two semi-circular sections which were placed on either side of the reinforcing stainless steel sheet and screwed together through clearance holes in the sheet to clamp it in place. Half of the sheet thickness was cut away from the inside flat face of each semi-circular section to ensure that the outside diameter of the assembled rod would be exactly 12.7 mm when clamped in place around the sheet. The rods extended approximately 30 mm beyond one end of the foil span to form a stem which fit into the mast which connected the foils to the load cell and drive system as described in Section 2.3. The rods were terminated within the foil 5 mm before the opposite end to ensure that the structure was securely embedded within the rubber.

The reinforcing stainless steel sheets were used to set the chordwise bending stiffness of the foils. The sheets were rectangular pieces, cut from 0.254 mm (0.010 inch) shim stock. To build foils with different bending stiffness, two different reinforcement designs were used. In the first design, the length of the sheet was 185 mm and it was placed in the foil to extend from 5 mm behind the leading edge to 10 mm ahead of the trailing edge, reinforcing almost the entire chord length of the foil. In the second design, length of the sheet was 35 mm and it was again placed in the foil 5 mm behind the leading edge but terminated where it was clamped by the aluminum rod. In this design, the sheet only reinforced the section of the chord ahead of the rod. In both designs, the width of the sheet was 130 mm and it was placed centered in the foil along the spanwise direction terminating 5 mm from either end. This placement ensured that the sheet was completely embedded within the rubber which prevented the metal and rubber components from separating during the experiments.

The lead weights were used to set the resonant frequency of the foils, effectively allowing this parameter to be changed without influencing the stiffness or geometry. The weights were constructed by gluing together strips of lead cut from 1.2 mm (3/64 inch) sheet. A cyanoacrylate adhesive, commercially available as "Original Instant Krazy Glue" was used to bond the strips together. Two different sizes of weights were constructed. The first design, having a mass of approximately 145 g, was comprised of six plies of lead strips with a maximum width of 20 mm. The second design, having a mass of about 384 g was assembled from ten plies of lead strips with a maximum width of 30 mm. The strips were cut to be 130 mm long, again to allow the weight to be completely embedded within the foil with 5 mm of rubber around each end. The weights were located in the foil such that the center of mass of the weights was 160 mm behind the leading edge. The strips were glued together such that the weights were symmetrical on either side of centerline of the foil profile. For the foils with a reinforcing stainless steel sheet running behind the aluminum rod, the weights were glued in place onto the sheet. For the foils which were only reinforced ahead of the rod, small tabs cut from the same 0.254 mm stainless shim stock were included in the center of the weight. Since the rubber shape was formed by a replica molding process, these tabs were necessary to hold the weight in place while the rubber resin cured.

In total, six foils were constructed, each with a different internal structure but with the same external geometry. Three foils had large reinforcements, stiffening the foil along its chord both ahead and behind the aluminum rod, and three foils had reinforcement only in the section ahead of the rod. For each reinforcement design, one foil had no embedded mass, one foil had a small (approximately 145 g) embedded mass and one foil had a large (approximately 384 g) embedded mass. The general foil design showing the layout of the internal components is illustrated in Figure 3.2.

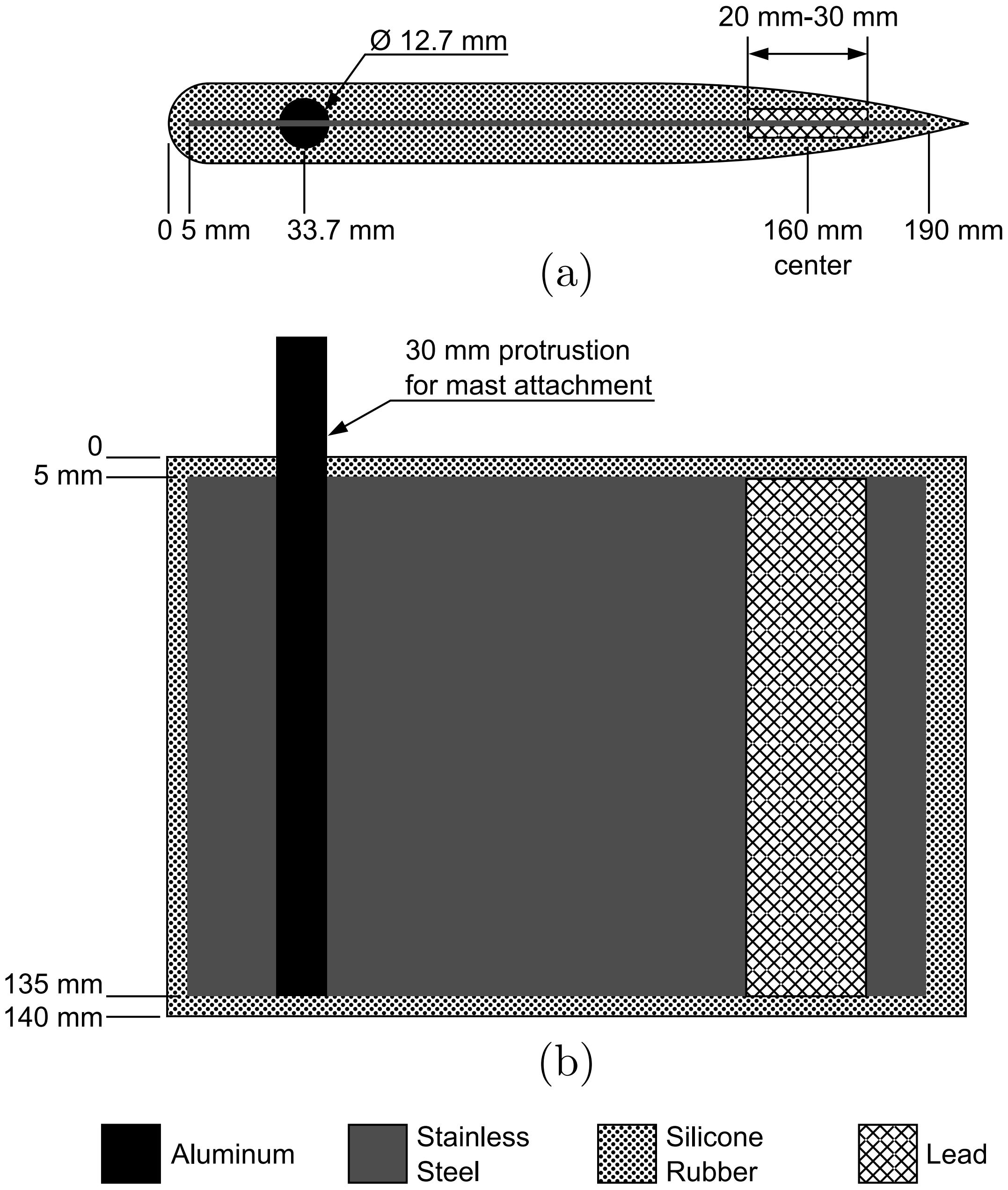

Figure 3.2: Cross-sections of the foil structure from the (a) profile and (b) plan views showing the dimensions of the internal metal components.

3.2 Fabrication Process

The flexible foils used in this study were constructed by replica molding in Dow-Corning Sylgard 186 polydimethylsiloxane (PDMS), a flexible silicone rubber material. The PDMS was supplied as two components which where mixed together and degassed in a vacuum oven to form a resin. The mixed resin was then poured into a mold containing the internal metal structure. The mold cavity was a negative of the foil shape. The PDMS resin was very viscous and could only be poured into the mold slowly. Inevitably a substantial amount of air was entrapped during the pouring process. Because of the need to pour the PDMS resin into the mold and remove entrapped air from the poured mixture before it solidified, it was necessary to mix and pour the PDMS in four separate batches and to apply vacuum to degas the mold after each pouring.

The mold used in the fabrication process was constructed from Dupont Delrin acetal plastic in the UVic Mechanical Engineering machine shop. A shape of half the foil profile was cut out of 20 mm high Delrin blocks. Seven tiers of these blocks were then stacked together to form each of the two sides of the mold. Steel dowels were inserted through the blocks to maintain alignment and the blocks were clamped together using threaded rods. The two mold halves were then bolted together. The top and bottom of the mold were formed by single pieces spanning both halves. These pieces were also machined from Delrin blocks. A track protruded from one surface of both pieces to hold the internal metal reinforcements and weights in place while the PDMS solidified. When assembling the mold, the bottom piece was put place with the track facing inward and the internal metal components were inserted into the track. The top was then put into position, again with the track facing inward to secure the upper end of the metal components. Both the top and bottom pieces were aligned and clamped in place using the same steel dowels and threaded rods which protruded from the upper and lower surfaces of the mold halves. The arrangement of the mold and the internal metal components of the foil structure during the molding process is illustrated in Figure 3.3.

After filling the mold cavity with the mixed and degassed PDMS resin, the mold was baked in a low-temperature (70°C) oven for approximately ninety minutes to cure the PDMS resin into a solid rubber. After the initial curing, the mold top was removed and any flash which formed due to PDMS resin seeping into the space between the mold top and upper surfaces of the sides was scraped away. The track

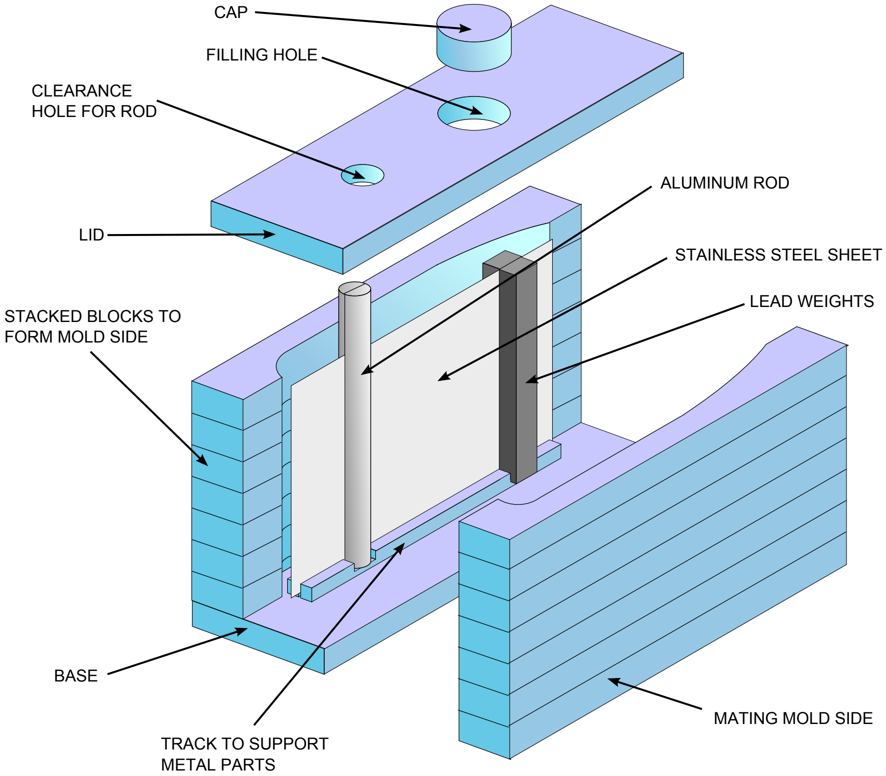

Figure 3.3: Arrangement for the replica-molding process to encapsulate the metal structure within a silicone rubber body of the foil shape.

on the mold top piece which held the metal pieces in place during the casting process left a void in top surface of the foil. After the initial casting, this void was filled with more PDMS resin and the mold top was then secured in place a second time but with the track facing outward. The mold was then baked again to cure the PDMS filling the void. The process of filling the void left by the track was then repeated on the bottom surface to complete the casting. To remove the completed foil from the mold, the top and bottom pieces were removed and the two sides were unbolted from each other. The sides were then pried apart by pulling on the alignment dowels.

3.3 Resonant Frequency Measurement

As discussed in Section 1.4, the resonant frequency is a governing parameter in the dynamic deformation behaviour of any structure. It was therefore important to be able to measure the resonant frequency of the foils constructed for this study. The measurement was performed with the foil immersed in water to account for added mass effects which are relevant to the conditions in the propulsive performance trials. The foil was placed in the water tunnel using the same set-up and positioning as in the propulsion trials (see Sections 2.1-2.3). The heaving axis position was set such that the foil was centered across the width of the test section. A sudden rotation of the foil was actuated using the pitching motor of the motion system. The rotation followed a trapezoidal motion profile accelerating and decelerating at $2000°/s^2$ with a maximum velocity of 200°/s through a total angular distance of 45°. The rotation terminated with the foil chord parallel to the test section walls when in the undeformed shape. The torque applied to the load cell was recorded after the rotation completed. In general, the objective of experiments which apply a sudden force or motion to a structure and record the response is to measure the impulse response which is made up of components oscillating at the natural frequencies [46].

The spectrum of the recorded torque was calculated and the maximum peak was taken as the resonant frequency of the foil. Approximately four periods of the response were extracted for analysis, beginning at the first zero-crossing following the completion of the actuated rotation. At the time of recording, second-order (-12 dB/octave) analog low-pass filters included in the measurement system removed frequency components which could cause aliasing in the calculated spectrum. Digital filtering of the recordings was therefore unnecessary. The data points from the extracted periods were multiplied by a Hanning window function to reduce leakage errors which may arrise due to sampling over a non-integer number of oscillation periods. These errors may occur without proper windowing because the discrete, finite-time Fourier transform used to calculate the spectrum is applied with the assumption that the signal is periodic within the recorded time. The Hanning window is a bell-shaped function which has a zero value outside of the recorded time period and is a popular windowing function in experimental vibration analysis [46]. Figure 3.4 shows examples of the recorded signal, windowed signal, and calculated spectrum for the foil B3. The extraction of the oscillation periods, multiplication by the windowing function and calculation of the spectrum using a fast Fourier transform (FFT) were all performed using built-in algorithms in Matlab.

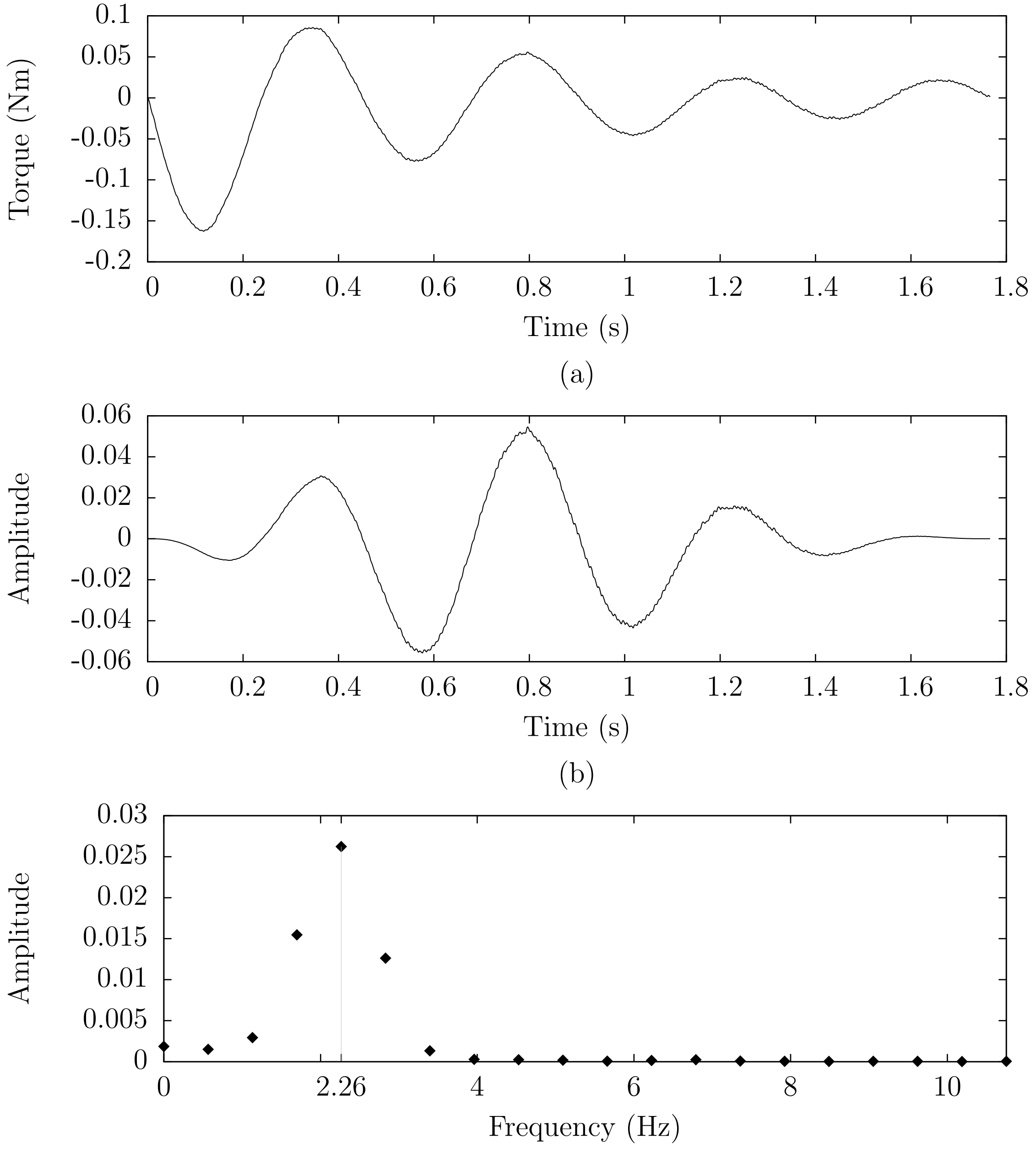

(a)

(b)

(c)

Figure 3.4: Examples of a (a) recorded torque signal, (b) windowed signal and (c) computed spectrum from the tests to measure the resonant frequency of the foils.

The tests to measure the resonant frequency were repeated using two different analog low-pass filter cutoff frequencies of 10 Hz and 50 Hz. These filters produced attenuations of -68 dB and -28 dB respectively at the Nyquist frequency of 500 Hz for the 1 kHz sampling rate of the load cell torque signal. The calculated frequencies obtained from the measurements with each filter are presented in Table 3.2. The results in each case are similar, indicating that the cut off frequency of 10 Hz is high enough to avoid distorting the relevant low-frequency components of the signal, while the cutoff frequency of 50 Hz is low enough to avoid aliasing in the spectrum. Since the filter with a 50 Hz cutoff frequency would produce less distortion in the signal components around the resonant frequencies of the foils, the values calculated from these measurements were accepted and will be used in the discussion of the results obtained from the propulsion trials.

Foil Name	**Resonant frequency (Hz) with 50 Hz Analog Filter**	**Resonant frequency (Hz) with 10 Hz Analog Filter**
A1	3.08	3.08
A2	2.77	2.76
A3	2.57	2.58
B1	2.81	2.82
B2	2.57	2.55
B3	2.26	2.27

Table 3.2: Measured resonant frequencies of the foil designs.

3.4 Bending Stiffness Measurement

One of the aims of this study is to be able to compare the propulsive performance of foils with equivalent resonant frequency but different levels of static bending stiffness and inertia. To make these comparisons, it is useful to be able to measure the bending stiffness of the foils and determine whether there is any substantial difference between designs of the same resonant frequency but with different internal structures. Since the stiffness is quantified by the magnitude of force required to effect a given deformation under static loading conditions, the stiffness measurement was performed by bending the foils and measuring the applied force.

Figure 3.5 shows the arrangement used in the stiffness measurement. The foils were connected from the aluminum rods to the same load cell and force measurement equipment used in the propulsion trials (see Section 2.3). This equipment was used to measure and record the force F_x. The load cell was in turn mounted on a single axis camera stage which allowed for translation to the left and right by a distance Δx as shown in the figure. At each data point, the distance was measured using a ruler. Near to the trailing edge of the foil, a 12 mm diameter post blocked the foil from moving and forced it to bend. The post was positioned to be behind the embedded lead weights so that the effect of these weights on the stiffness would be reflected in the measurement. During the tests, the attachment point of the foil to the mast and load cell was translated to the left or right to a defined position and the applied force was recorded for one second at 10 kHz. These recordings were averaged to give the applied force at the given position. The measurements were taken in order of increasing displacements at intervals of 10 mm up to a maximum of 40 mm. The post was then moved to the other side of the foil and the measurements were repeated with the foil bent in the opposite direction. A tare measurement was also taken for each foil with no deformation applied and subtracted from the applied force at each displacement.

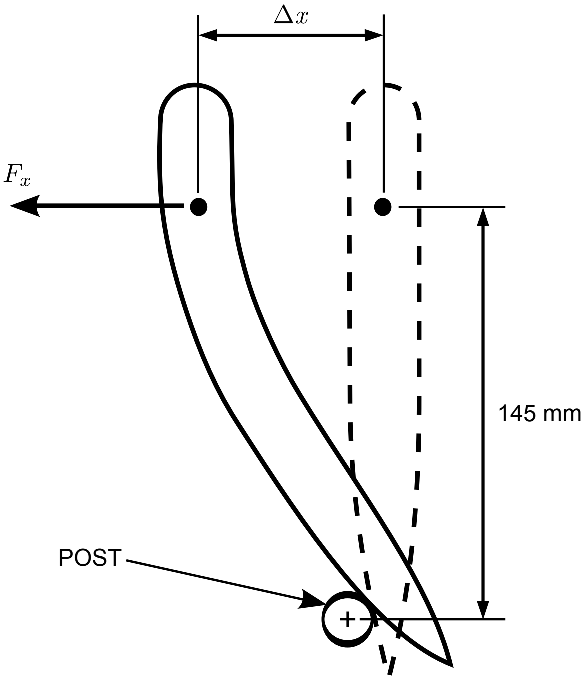

Figure 3.5: Set-up for the measurement of the foil bending stiffness.

Figure 3.6 shows the applied force plotted against the displacement for all six foils. In each case, a linear regression line through the origin was fit to the measurements.

The slope of this regression line is an indication of the foil bending stiffness (see Table 3.1). The regression line was forced to fit through the origin because the deformation behaviour should be in theory symmetrical.

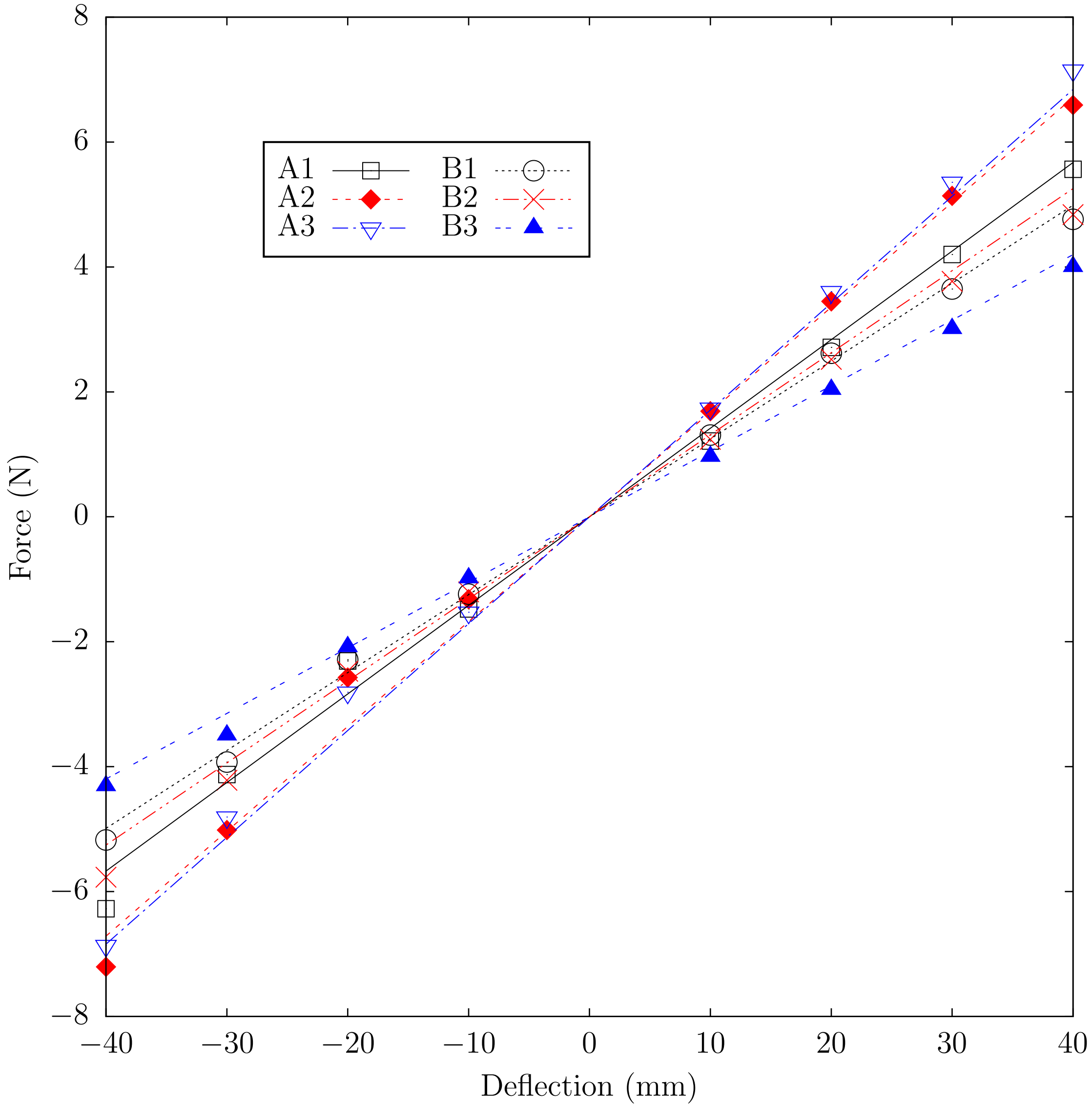

Figure 3.6: Applied forces and deflections during the bending stiffness measurement of the foils. The markers represent measured points and the lines represent the fitted linear regression.

All of the “A” category foils which have a stainless steel sheet reinforcing the entire chord length are at least 5% stiffer than the “B” category foils which are only reinforced ahead of the aluminum rod. However, the stiffness is not completely uniform within each group. The lead weights embedded within the “A” category foils were found to increase the stiffness by approximately 20%. In the case of the “B” category foils, the trend is not clear because the embedded weight appears to increase the stiffness in one case and reduce it in another. The foil B1 which has no weight is found to be about 19% stiffer than the foil with largest weight, B3. The foil B2, which has an intermediately sized weight, has a bending stiffness that is 5% greater than B1. One possible explanation for this unexpected result is that the thin coating of silicone rubber around the weight in the foil B3 was able to detach from the weight, slipping over its surface and taking most of the loading during the bending. The relatively high stress on the rubber would then cause the foil to bend more sharply at this location and allow the foil to achieve greater deflections at the tip with less applied force.

The bending stiffness measurements indicate that the foil design has allowed for the construction of foils with equivalent resonant frequency but with substantially different stiffness. Considering the pair of foils A2-B1, the resonant frequencies differ by 1.4% while the bending stiffness of foil A2 is 34% greater than that of foil B1. Since the resonant frequency is related to both the stiffness and inertia, the effective inertia of the foil A2 must also be greater by approximately the same factor due to the embedded mass. The results are similar when comparing the results within the pair of foils A3-B2. In this case, the resonant frequencies are essentially the same, while the stiffness of the foil A3 is approximately 30% greater.

The results of the stiffness measurement have also demonstrated that, to a limited extent, the foil design which was used here allows for the construction of foils with equivalent bending stiffness but different resonant frequencies. When comparing the foils A2 and A3, the stiffness is found to differ by 1.8% but the resonant frequencies differ by 7.2%. Similarly, the foil B1 has a stiffness which is 4.6% lower than B2, but a resonant frequency which is 9.3% greater. In both of these cases, the difference in resonant frequency is more substantial than the difference in bending stiffness. However, in both cases there is also found to be some variation in the stiffness within the pairs. Constructing foils of equivalent stiffness but with an even greater difference in resonant frequency than what was observed here would likely be difficult because the embedded lead weights which are necessary to increase the inertia also have some effect on the stiffness. To increase the difference in resonant frequency, a larger weight would be required which would stiffen a longer portion of the chord length and consequently have a greater effect on the overall stiffness of the foil.

The results shown in Figure 3.6 indicate some asymmetry and nonlinearity in the bending behaviour of the foils. In particular, the force measurements for the "A" category foils at displacements of -20 mm lie somewhat above the regression line, indicating that a smaller force was required to cause these deflections than what is predicted by the linear trend. The same discrepancy is not observed when bending the foils in the opposite direction or in the case of the "B" category of foils. It is expected that this asymmetry arises due to warping of the stainless steel sheet which reinforces the entire chord length of the "A" category foils. This sheet is rolled metal product and has internal stresses remaining from the manufacturing process which can cause the finished parts to bow. This error in flatness was manifested in the completed foils where the chord axis was found to be not perfectly perpendicular to the axis of travel in the bending stiffness measurements. In addition to the asymmetrical bending behaviour, this geometry would also cause a pitch bias in the propulsion trials. However, these errors in the structure and geometry are not believed to have had a dominant effect on the propulsive performance because it is observed that the bending behaviour of these foils is generally symmetrical with the execption of a few outlying data points. In the propulsion trials, the oncoming flow would also help to straighten the foil and align the chord with the streamwise direction.

Bends in the lead weights introduced additional errors in flatness and straightness to the completed foils. The lead sheet is a very malleable material and inevitably some small bends or twists were introduced into the weights during the foil manufacturing. These bends in the weights resulted in trailing edges which were not completely straight or aligned with the foil spanwise direction. In the bending stiffness measurements, this error resulted in a small gap between some points on the foil and the post when the two were first brought into contact. In spite of this gap, the location where any point on the foil first contacted the post always served as the datum from which all of the applied deflections were measured. Similar to the errors in flatness caused by warping of the stainless steel sheets, the imperfections in the geometry resulting from bends in the lead weights are not believed to have significantly impacted the results of the propulsion trials.

3.5 Theoretical Modelling of the Foil Structure

It is useful to develop a predictive model which would allow the dynamic deformation behaviour of the foils to be related to the structural properties such as mass and stiffness. Such a model can be used to explain why particular trends in the deformation are observed and to explain differences in propulsive performance between the foil designs. To this end, the damped-oscillator model shown in Figure 3.7 is considered. In this model, the block at the left side of the figure represents the aluminum rod near the leading edge of the foil which is driven in the heaving motion $h(t)$. In discussions of structural vibrations, this component of a model is commonly referred to as the *base* of the structure. The stiffness k represents the bending stiffness of the foil. The damping elements c_{int} and c_{abs} simulate the actions of internal structural damping and fluid drag respectively. The mass m is the effective mass of the foil including added fluid mass, and the motion $\gamma(t)$ is analogous to the movement of the flexible section of the foil chord behind the rod.

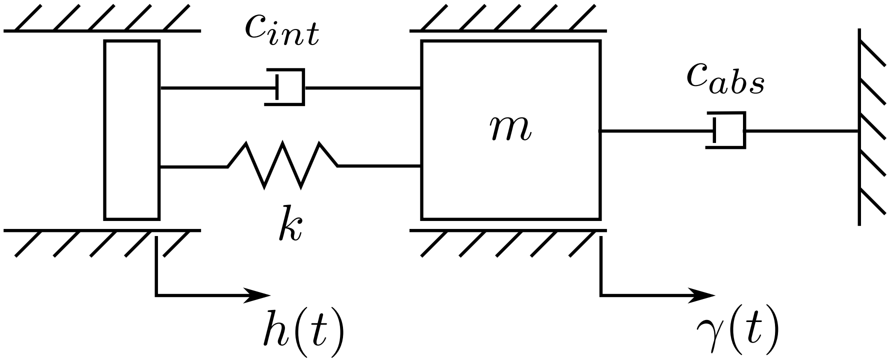

Figure 3.7: Schematic of the damped-oscillator model considered to calculate the phase of the bending of the foil with respect to the heaving motion and predict the amplitude of the motion of the flexible foil chord.

One challenge in the development of a damped-oscillator model is the selection of an appropriate damping law. Linear or viscous damping, where the damping elements exert a force opposing the motion and directly proportional to the velocity, is the most mathematically convenient approach. However, this damping law may not be a physically accurate description and consequently models based on linear damping may fail to accurately predict the dynamic response of the structure. In the case of the damping element c_{abs}, which acts on the absolute motion of the mass m, quadratic damping is likely a reasonable model since forces arising from fluid drag are proportional to the square of velocity. In this case, the force exerted by the damping element is given by the expression [46]:

$$f_{quad} = c_{abs} \left| \frac{d\gamma}{dt} \right| \frac{d\gamma}{dt} \tag{3.1}$$

The use of this damping model will result in a non-linear differential equation describing the motion of the mass. In the case at hand, the main interest is to determine the response of the foil to a sinusoidal input motion, $h(t) = h_0 \cos \omega t$. For this purpose, one possible approach to simplify the quadratic damping model is to replace the quadratic damping element with a linear damping element which dissipates equivalent energy during each cycle of the motion [46]. When sinusoidal input motions are applied, the mass is also expected to move in a sinusoidal motion profile:

$$\gamma(t) = \gamma_0 \cos\left(\omega t + \phi_{abs}\right) \tag{3.2}$$

Integrating the force applied by the damping element with respect to distance gives the energy dissipated during one cycle of the motion [46]:

$$E_{quad} = \frac{8}{3} c_{abs} \gamma_0^3 \omega^2 \tag{3.3}$$

The energy dissipated by a linear damping element during one cycle of a sinusoidal motion is given by [46]

$$E_{lin} = \pi c_{lin} \omega \gamma_0^2 \tag{3.4}$$

Equating the two energies and solving for the linear damping coefficient gives an expression for an equivalent linear damping coefficient to represent the quadratic damping [46]:

$$c_{abs,eq} = \frac{8}{3\pi} c_{abs} \omega \gamma_0 \tag{3.5}$$

To represent the internal damping c_{int}, it is reasonable to expect that the damping action may result from stress-strain hysteresis loops which dissipate energy as the materials stretch and contract. In this case, the energy lost per cycle of the motion is proportional to the square of the amplitude but independent of the frequency of the motion [46]. Again, by equating the energy lost in the hysteresis loop to the energy dissipated by a linear damping element, it is possible to derive an expression for an equivalent viscous damping coefficient to represent the hysteretic damping [46]:

$$c_{int,eq} = \frac{\beta}{\omega} \tag{3.6}$$

where β is the *hysteretic damping constant.* It is important to note that this equivalent damping element will act to produce a force proportional to the relative velocity between the mass and the base, $d(\gamma - h)/dt$, rather than the velocity of the mass in an absolute reference frame.

When the damping elements in the oscillator model are replaced with equivalent linear damping coefficients, it is possible to formulate a linear ordinary differential equation describing the dynamics of the system:

$$m\frac{d^2\gamma}{dt^2} + (c_{int,eq} + c_{abs,eq})\frac{d\gamma}{dt} + ky = kh + c_{int,eq}\frac{dh}{dt} \tag{3.7}$$

where the (t) have been omitted from $\gamma(t)$ and $h(t)$ since these quantities are implied to be time-varying. Substituting the forcing term from the right-hand side of Equation 3.7 into the well-known solution for a second-order oscillator system subject to sinusoidal input [46] gives the expression for the amplitude ratio:

$$\frac{\gamma_0}{h_0} = \sqrt{\frac{1 + (2\zeta_{int}r)^2}{(1-r^2)^2 + (2\zeta_{total}r)^2}} \tag{3.8}$$

where

$$\zeta_{total} = \frac{c_{int,eq} + c_{abs,eq}}{2\sqrt{km}}, \tag{3.9}$$

$$\zeta_{int} = \frac{c_{int,eq}}{2\sqrt{km}} \tag{3.10}$$

and

$$r = \omega\sqrt{\frac{m}{k}} \tag{3.11}$$

It can be noted that the equivalent damping coefficient which represents quadratic damping (Equation 3.5) is itself dependent on the amplitude, γ_0, of the motion of the mass. When this damping coefficient is substituted into Equation 3.8, the amplitude ratio becomes implicitly defined and it is necessary to solve a quartic polynomial (see Appendix B).

Once the amplitude ratio of the resulting motion for a given input frequency has been determined from Equation 3.8, the phase of the relative motion between the mass and the base can be calculated. The phase of the forcing term with respect to the input motion is determined from trigonometry:

$$\phi_{force} = -\tan^{-1}(-2\zeta_{int}r) \tag{3.12}$$

The phase of the absolute motion with respect to the applied force can be found from known solutions to the differential equations describing second-order oscillators [46]:

$$\phi_{abs-force} = -\tan^{-1}\left(\frac{2\zeta_{total}r}{1-r^2}\right) \tag{3.13}$$

The phase of the absolute motion with respect to the input motion is then given by

$$\phi_{abs} = \phi_{abs-force} + \phi_{force} \tag{3.14}$$

The absolute motion of the mass has thus been completely defined in terms of its amplitude and phase with respect to the input motion. The phasing of the relative motion or deformation of the structure can then be found by subtracting the input motion waveform and again applying trigonometric identities:

$$\phi_{rel} = -\tan^{-1}\left(-\frac{\frac{\gamma_0}{h_0}\sin\phi_{abs}}{\frac{\gamma_0}{h_0}\cos\phi_{abs} - 1}\right) \tag{3.15}$$

When quadratic or hysteretic damping models are used, it is useful to define the *quadratic damping frequency*

$$\omega_{qd} = \frac{3\pi\sqrt{km}}{8h_0 c_{abs}} \tag{3.16}$$

and the *hysteretic damping frequency*

$$\omega_{hd} = \frac{\beta}{\sqrt{km}} \tag{3.17}$$

These parameters remained fixed for a given foil structure and input motion amplitude as the frequency of the applied motion is changed. By determining these two frequencies and substituting into Equations 3.5 and 3.6, the equivalent damping coefficients can be expressed as functions of the input motion frequency and amplitude ratio. The resulting expressions are in turn substituted into Equation 3.8, so that the amplitude ratio can be determined for any given frequency of the input motion. The third important frequency which is required to completely define the structural properties of the foil design is the natural or resonant frequency,

$$\omega_n = \sqrt{\frac{k}{m}} \tag{3.18}$$

which sets the frequency ratio, r. For the foils constructed for this study, the resonant frequencies were determined using the tests described in Section 3.3. The *quadratic damping frequencies* and *hysteretic damping frequencies* were determined empirically by fitting the deformation behaviour predicted by the model to match the deformation behaviour observed in the propulsion trials. This fitting is described in Section 4.2.

Chapter 4

Analysis and Discussion of the Propulsive Performance Measurements

This chapter presents the experimental results of this study and develops explanations for the observed trends relating the propulsive performance to the foil structure and the oscillation kinematics. Because the dynamic deformation behaviour of the foils was found to be one of the main physical phenomena which governs the propulsive performance, it is useful to be able to observe the deformation, at least indirectly as the foil structure and oscillation kinematics are varied. This observation method is explained in Section 4.1. In Section 4.2, the parameters in the damped-oscillator model developed in Chapter 3 are determined empirically for the various foil designs. The trends in the deformation behaviour predicted by this model are used in the subsequent sections to explain the observed effects of the foil stiffness and mass and the oscillation amplitude and frequency on the propulsive performance. Section 4.3 examines the trends in thrust generation and efficiency for the different foil designs at various Reynolds numbers. Similarly, Section 4.4 examines changes in propulsive performance at various heave amplitudes. For the results presented in Sections 4.3 and 4.4, the foils were driven in a heaving motion and the pitching was provided only by the passive deformation of the foils. In Section 4.5, the effects of combining active heave and pitch motions are examined. Finally, Section 4.6 discusses how the results obtained from these experiments can be used to guide the design of practical propulsion systems.

4.1 Indirect Observation of the Foil Deformation

An understanding of the foil deformation behaviour is essential to explain the observed performance trends in the results, both when comparing the thrust generation and efficiency of foils with different structures and when considering the changes in performance which occur when the kinematic conditions are varied for given structure. The relative timing or phase between the foil deformation and the actuating motion is one important aspect of the dynamic deformation of a foil. The deformation phase acts to set the orientation of the foil with respect to the relative fluid flow throughout the motion cycle, particularly when there is no active pitching motion applied as in the results discussed in Sections 4.3 and 4.4. For efficient propulsion, it is useful to have the greatest deflection occur at some time when the foil is near the midpoint of its motion cycle when the transverse velocity is highest [27,31,47]. A foil which is operating with this phasing will generally present a smaller frontal area to the oncoming flow which reduces drag, and also direct a larger component of the lift force along the travel direction which increases the thrust as compared to a foil which undergoes the maximum deflection near the endpoints of its oscillation cycle. This concept is illustrated schematically in Figure 4.1 where the foil in the center frame with a deformation phase of $-\pi/2$ is shown to have smaller force components resisting the transverse and forward motions and larger force components in the direction of travel.

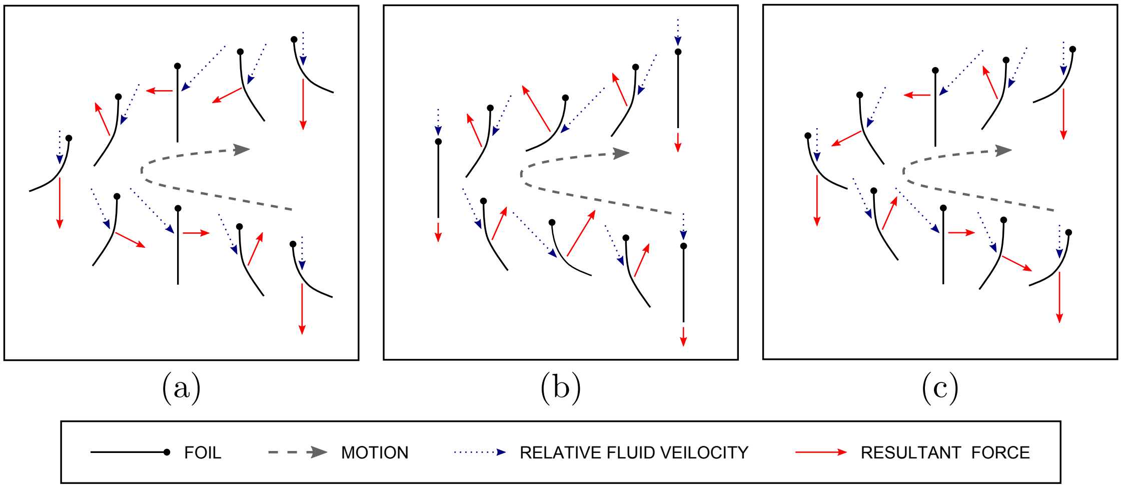

(a) (b) (c)

Figure 4.1: Conceptual illustration of a chordwise-flexible oscillating foil operating with the bending occurring (a) in phase, (b) at a phase of $-\pi/2$ and (c) anti-phase with respect to the input heaving motion.

In a limited number of trials, photographic recordings were made and in these cases the phase of the bending motion, as well as the amplitude, can be observed directly. However, it would have been impractical to make photographic recordings of all of the experiments conducted for this study because collecting these recordings is time-consuming and the images require a large volume of digital storage space. It is therefore useful to be able to correlate the deformation with the load cell measurements during trials for which photographic recordings are unavailable. To this end, it is useful to consider the foils as cantilevered beam structures. This model is reasonable since the foils are held at a set angle and position at the aluminum rod and the section of the chord length behind this rod is allowed to bend freely with no constraints at the trailing edge. For many vibrating beams, the deflections and bending moments can be assumed to be proportional as long as the applied forces or motions project onto a single vibration mode shape. For the foils considered in this study, the frequencies of the actuated motions are near to the lowest resonant frequencies and thus are expected to primarily excite the first vibration mode. The assumed proportionality between bending moments and deflections is valid provided that the materials have a linear stress-strain relationship and the shear deformations and rotational inertia are negligible [46].

The cantilevered beam model is useful here because in cases where the foils were not actively rotated, the bending moment at the aluminum rod is the main action which produces the load cell torque signal. If the model is valid, it is then reasonable to expect the measured torque and the observed deflection to be proportional in the trials for which photographic recordings are available. This expectation is shown to be realized in Figure 4.2 which shows the heave position, deflection and torque signal for three different foils operating at the same oscillation frequency. All three quantities have been normalized by the maximum recorded value during the trials. It is observed that the torque and deflection are proportional and occur at the same phase with respect to the heaving motion. It should be noted that the load cell torque and photographs were in fact recorded during separate trials and were synchronized for the purpose of this figure by matching the encoder positions with the photographically observed heaving position. The validity of the model is further demonstrated by Figure 4.3 which shows the phase of the deformation with respect to the heaving motion observed from the photographic recordings and torque signals for three foil designs over a range of oscillation frequencies. It is found that the phases determined from each method are generally consistent with each other.

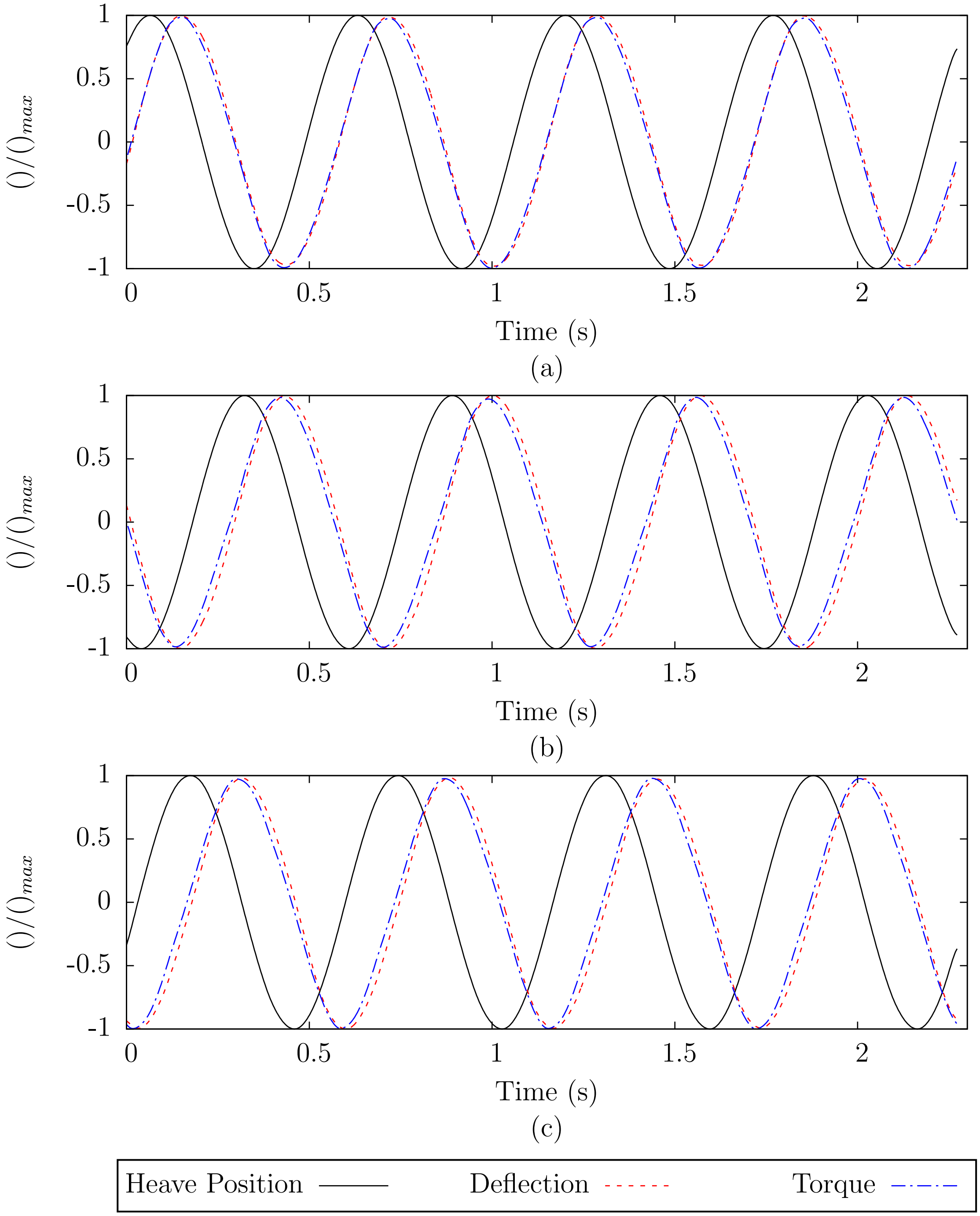

(a)

(b)

(c)

Figure 4.2: Normalized heave position, trailing edge deflection and pitch axis torque over four oscillation cycles for foils (a) A2, (b) B1 and (c) B3. The kinematic conditions during these trials are $St = 0.3$, $h_0/c = 0.125$ and $Re = 58\ 700$.

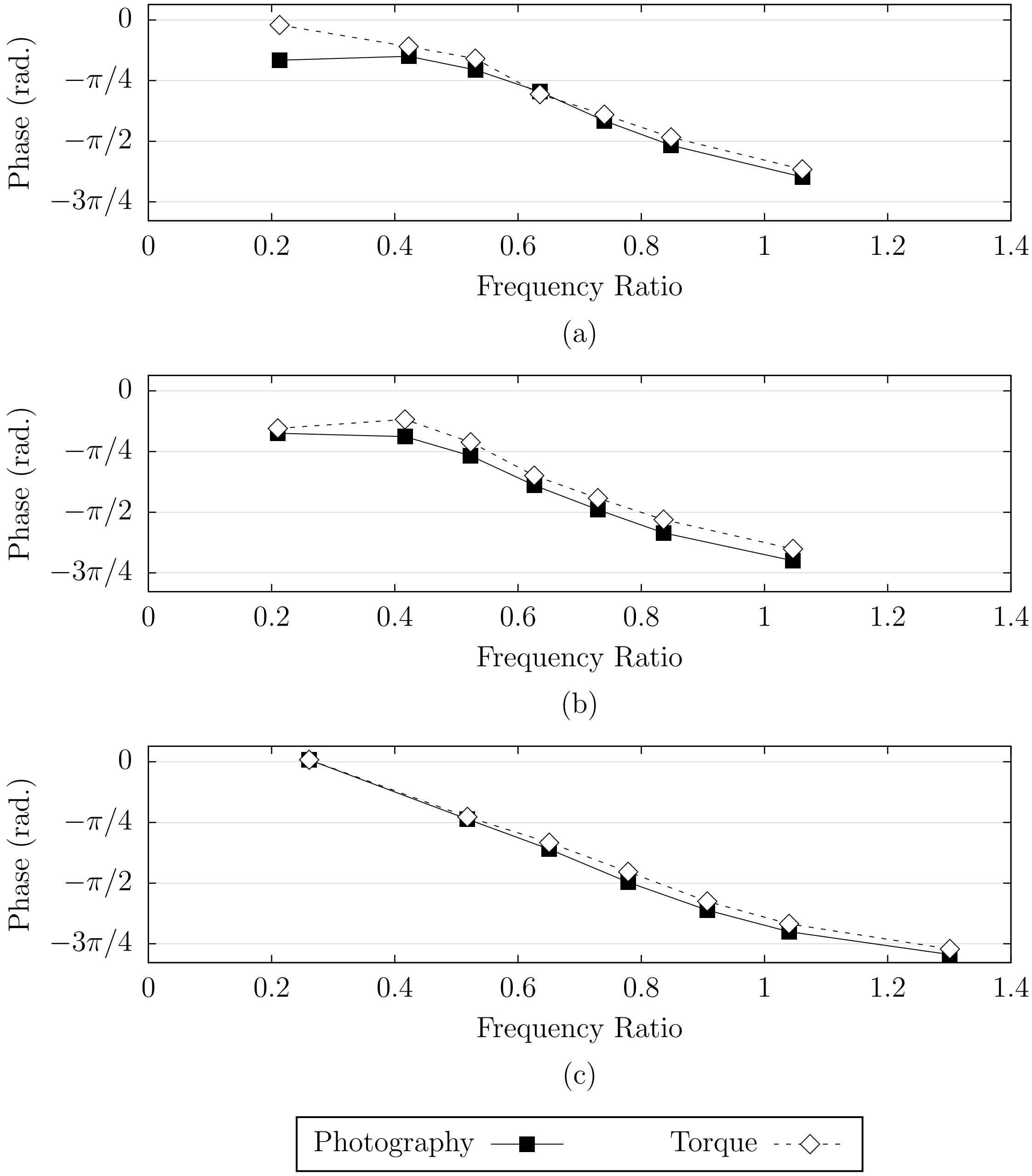

(a)

(b)

(c)

Figure 4.3: Phase lag between the foil deformation and the heaving motion as observed from the photographic records and the load cell torque signal over a range of frequency ratios for foils (a) A2, (b) B1 and (c) B3. The kinematic conditions during these trials are $h_0/c = 0.125$ and $Re = 58\ 700$.

4.2 Determination of Damping Parameters

While it has been demonstrated that the phasing of the foil deformation can be reliably observed from the load cell torque signal in Section 4.1, based on the cantilever beam model, a more complete understanding of the deformation behaviour and its relation to the structural properties is developed by considering a predictive model such as the damped-oscillator model discussed in Section 3.5. To assess the suitability of this model and the applicability of various damping laws, the model was tested with six different combinations of elements to represent the structural damping and fluid drag. When discussing the dynamic behaviour of a structure over a range of vibration frequencies, the term *phase response* can be used to refer to the evolution of the phase lag between the deformation and the input motion as the frequency is varied. The ability of a model with a particular combination of damping elements to accurately predict the phase response was taken as indication of its suitability to describe the structural dynamics of the foil. The damping elements considered in each of the models are summarized in Table 4.1.

Model	**Internal Damping**	**Absolute Damping**
1	none	linear
2	linear	linear
3	none	quadratic
4	linear	quadratic
5	hysteretic	quadratic
6	hysteretic	linear

Table 4.1: Summary of the damping elements used in each of the oscillator models which were tested as possible representations of the structure of the foils.

For each model, the predicted phase response was fitted to the measured phase response as observed from the load cell torque signal for each foil. To specify the model parameters, the resonant frequencies were taken from the measured values discussed in Section 3.3. The damping frequencies given by Equations 3.16 and 3.17 or the linear damping ratios as appropriate were adjusted to minimize the sum of the squared error between the predicted phase and the measured phase over a set of measurement points taken from a propulsion trial conducted with a flow speed $Re =$ 58 700 and heave amplitude $h_0/c = 0.125$. For each foil, the measured phase at the lowest frequency ratio was omitted from the fitting because, as observed in Figure 4.3a, there is some discrepancy between the photographic and torque measurements at this point. The calculations to find the damping parameters which yielded the minimum squared error were performed using the multi-variable optimisation routine in Matlab implemented by the function “fmincon” with the interior-point algorithm selected.

In the cases of Models 1 and 2 which contain only linear damping elements, the value of the linear damping ratio was restricted such that $\zeta_{total} \leq 0.01$. Similar restrictions were placed on Models 4 and 6 which also contain linear damping elements, but in these cases, the restriction was placed only on the contribution of the linear damping element. For example, for Model 4 it was required that $c_{int}/\left(2\sqrt{km}\right) \leq 0.01$. This maximum value was imposed based on examinations of the signals recorded during the tests to measure the foil resonant frequencies described in Section 3.3. The motion of a structure with linear damping undergoing free vibrations will take the form of an exponentially decaying sinusoid [46]:

$$\gamma(t) = Ce^{-2\zeta_{total}\omega_d t}\sin(\omega_d t + \phi) \tag{4.1}$$

where $\omega_d = \omega_n\sqrt{1-\zeta_{total}^2}$. This function was fitted to the load cell torque signal recorded for each foil by dividing out the dominant frequency component, taking the natural logarithm and using a least-squares linear regression to determine the constant C and the exponent $2\zeta_{total}\omega_d$. An example of a recorded signal and the corresponding fitted decaying sinusoidal function are illustrated in Figure 4.4. The maximum damping ratio calculated from the exponent of the fitted function for all of the foils was $\zeta_{total} = 0.00882$. Consequently, it was decided to restrict the range of linear damping coefficients used in the damped-oscillator models to prevent the optimisation algorithm from calculating an unrealistically large value in order to better match the measured phase response.

For four of the foils, Model 5 was able to fit the phase measurements with the least error, while for the other two, Model 4 was found to achieve a better fit. The fact that Models 4 and 5 achieve the best agreement with the measurements is unsurprising because these models include quadratic damping due to fluid drag along with some form of internal damping and thus likely best represent the physical damping actions affecting the foils. These two models also offer the most flexibility to the optimisation algorithm when fitting the model to the measurements since there are two parameters

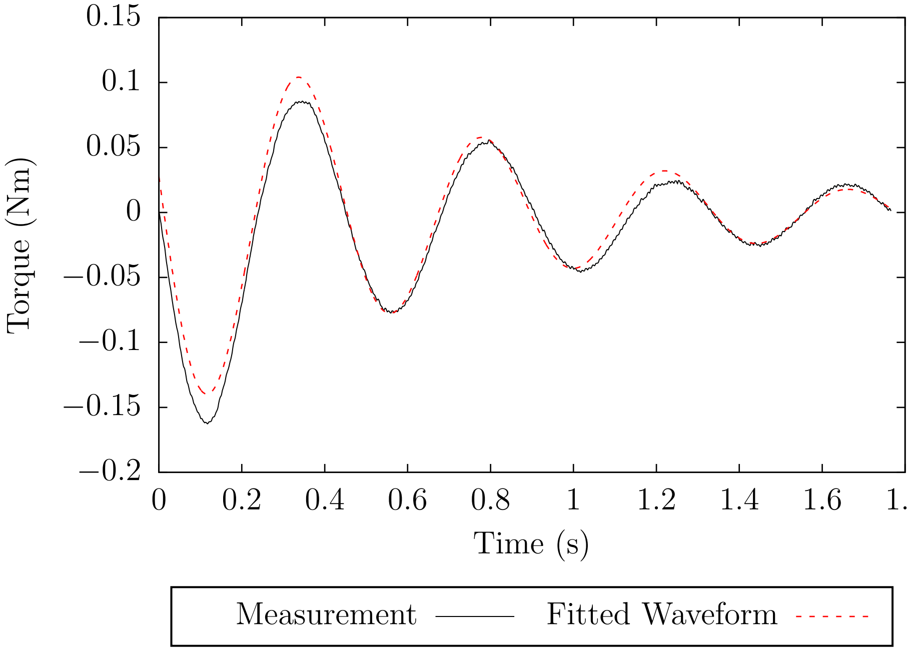

Figure 4.4: Example of a recorded torque signal from the tests to measure the resonant frequencies of the foils and a fitted exponentially-decaying sinusoidal function.

which can be adjusted independently, one of which allows for a damping coefficient that varies with both frequency and amplitude. The phase responses predicted by the fitted models for foil B3 are compared with the measured phase response in Figure 4.5. The results are similar for the other foils. Although Models 4 and 5 achieved the best fit to the measurements, inspection of Figure 4.5*c* reveals that the agreement between measurements and the predictions of Model 3 is also good. This model includes only quadratic damping acting on the absolute motion of the mass. Conversely, Figures 4.5*b* and 4.5*f* show that Models 2 and 6 which include internal damping as in Models 4 and 5, but replace the quadratic damping with linear damping, are not able to accurately predict the phase response. This finding suggests that quadratic damping which results from fluid drag is one of the principal physical phenomena governing the dynamic deformation of the foils. Results emphasizing the importance of quadratic damping governing the dynamics of chordwise flexible oscillating foils have also been reported by Ramananarivo et al. [31]. Since Model 3, which omits any internal damping element, is mathematically simpler than Models 4 and 5 but is still able to represent the dominant physical phenomena and accurately predict the phase response, further discussions of the structural dynamics will refer to this model.

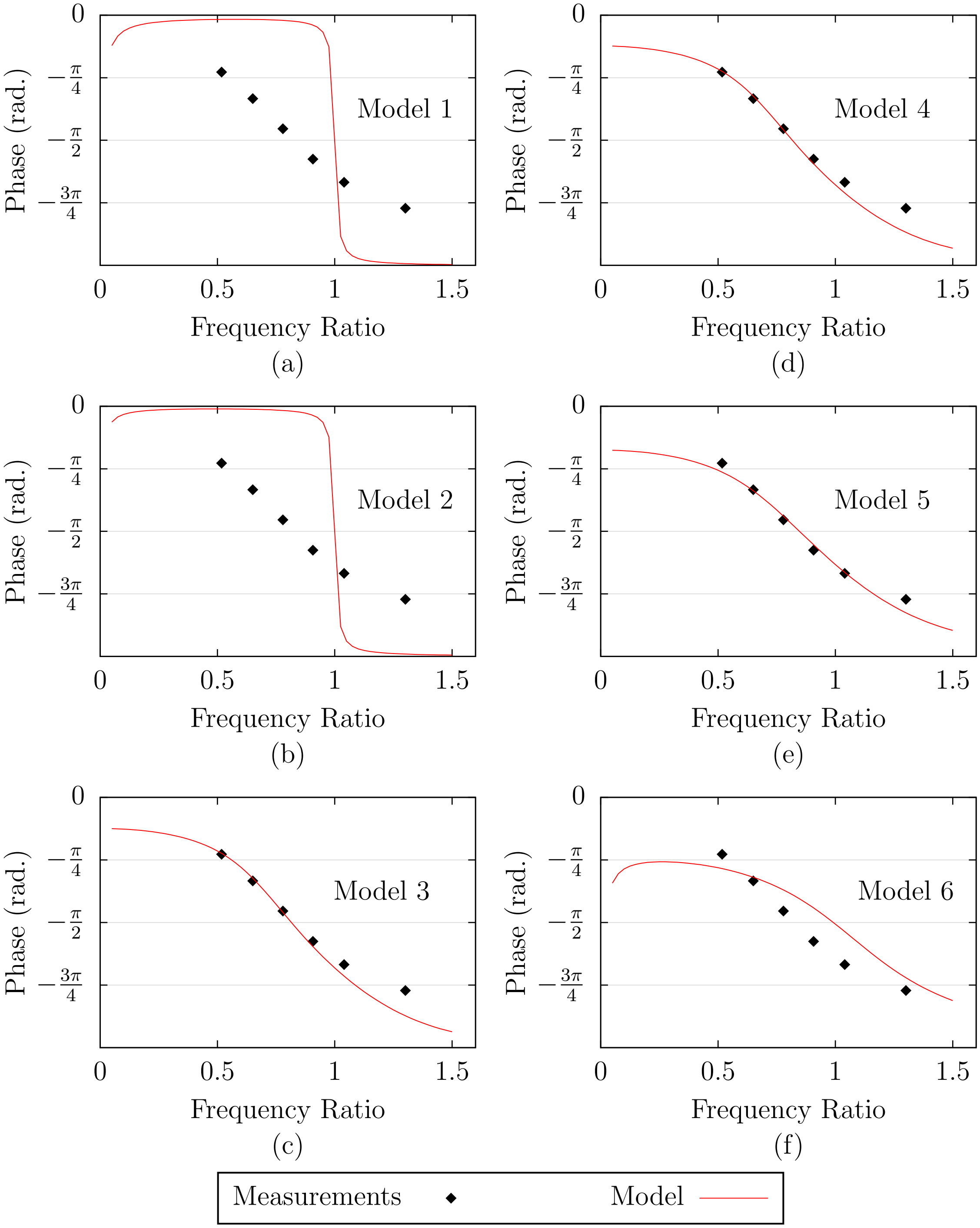

(a) (d)
(b) (e)
(c) (f)

Figure 4.5: Comparison of the phase responses predicted by the various damped-oscillator models with the deformation phase as observed from the torque signal for the foil B3 at Re=58 700 and $h_0/c = 0.125$.

The variation with respect to frequency ratio of the equivalent damping ratio calculated by the fitted damped-oscillator model for each foil is shown in Figure 4.6. By comparing the different foil designs, it is observed that the damping ratios generally decrease with increasing inertia or stiffness of the foil. In other words, the vibration of the stiffer and heavier “A” group foils is relatively less damped compared to “B” group foils of the same resonant frequency. This difference in damping produces corresponding changes in the phase response and the amplitude of the motion of the bending foil. The implications of these changes for the propulsive performance will be examined in Sections 4.3 and 4.4. The decrease in damping ratio with increasing inertia or stiffness is expected since these quantities appear in the denominator of the expression for the equivalent damping ratio (Equation 3.9). One exception to this trend is the foil B3 which has a larger embedded mass than the foil B2, but is observed to also have a larger damping ratio. However, the foil B3 was also measured to have a smaller bending stiffness than B2 in spite of the fact that both foils have the same internal reinforcement design. It is possible that this smaller bending stiffness has lead to the greater damping ratio of the foil B3.

As well as predicting the phase responses of the foils, the damped-oscillator model also offers a qualitative description of the *amplitude response*, or variation of the amplitude of the foil motion in response to input motions of varying frequencies. For propulsion applications, it is most relevant to examine the amplitude of the absolute motion of the bending section the foil since this amplitude will determine the wake width and relative velocity between the foil and the fluid. The discussion of amplitude in this way contrasts the discussion of phasing where the relative motion rather than the absolute motion is considered more relevant. It is not reasonable to expect to be able to observe quantitative agreement between the amplitude ratios predicted by the model and the measured motions. The model has simplified the foil to a single-degree-of-freedom system and no solution in space by which the time-varying solution can be scaled has been determined. However, it is possible to compare the trends in amplitude ratio predicted by the model with the photographically observed motions. This comparison is shown in Figure 4.7 where the measured amplitude of the trailing edge motion and the calculated amplitude ratios are plotted together for three different foil designs. It is observed that the measured motion and predicted amplitude ratio follow a similar curve in variation with the frequency ratio. It is also found that the maximum observed motion occurs at approximately the same frequency ratio as the maximum calculated amplitude ratio.

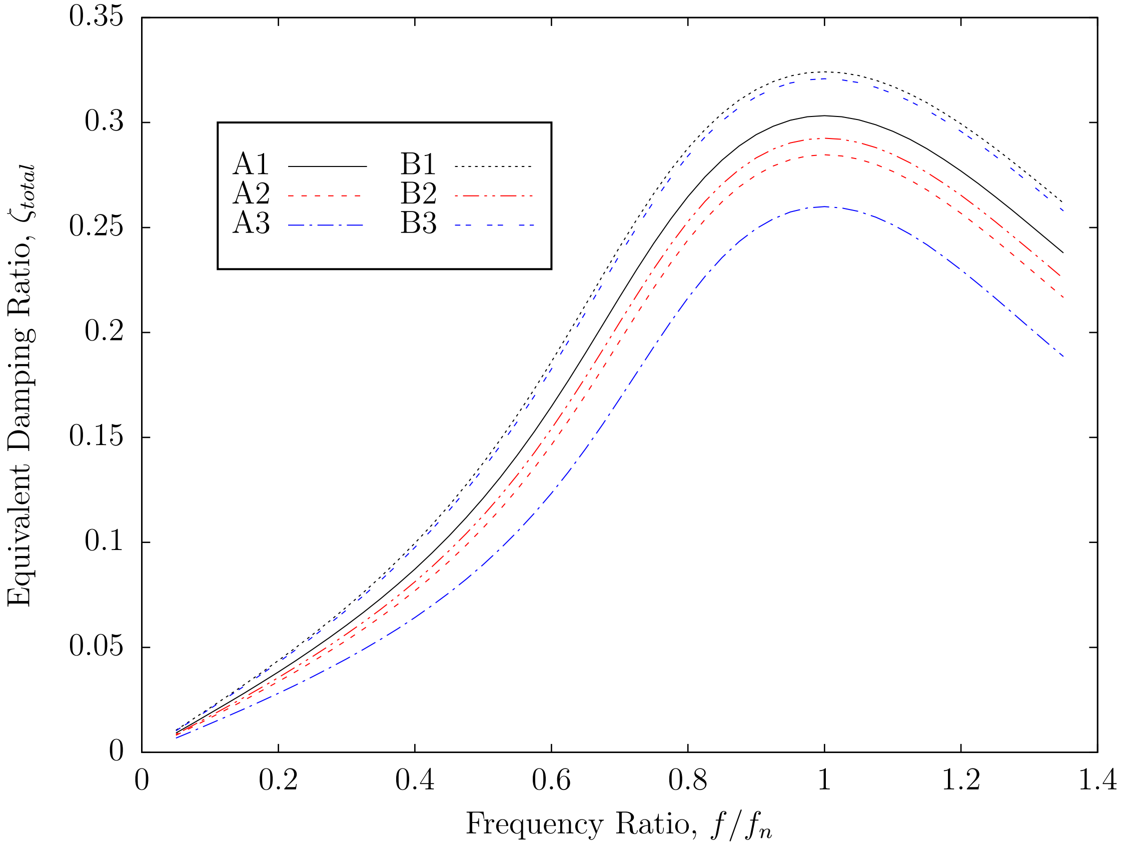

Figure 4.6: Variation of the equivalent damping ratio with frequency ratio as predicted by the damped-oscillator model for each foil design.

The damped-oscillator model which has been considered here provides some insight into the physical phenomena which govern the deformation of the foils which in turn influences the propulsive performance. The mathematics have been greatly simplified by first replacing the partial differential equation problem describing the motion of the foil in time and space with a single-degree-of-freedom system described by an ordinary differential equation. Further simplifications have been made by replacing the non-linear damping mechanisms with equivalent linear elements. In spite of these simplifications, the model is able to accurately predict the evolution of the phase of the relative motion and the amplitude of the absolute motion of the bending foil as the input heaving frequency is varied. The simplified model can therefore serve to assist in the development of explanations for the propulsive performance trends which are observed as the foil design or oscillation kinematics are varied. These explanations are developed in the following sections.

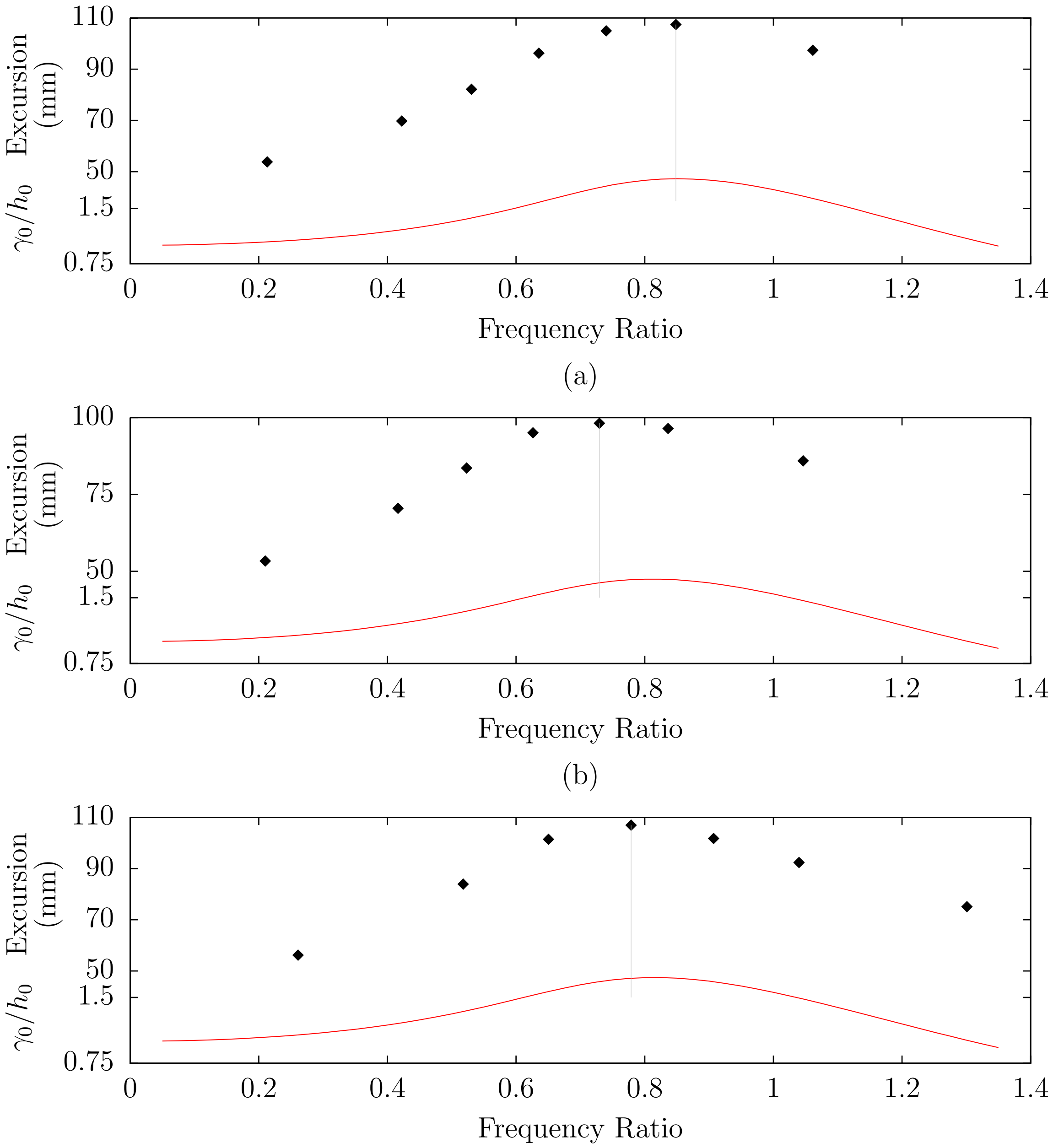

(a)

(b)

(c)

Figure 4.7: Comparison of the photographically observed trailing edge excursion with the amplitude ratios predicted by the damped-oscillator model for foils (a) A2, (b) B1 and (c) B3.

4.3 Effect of the Foil Structure on Propulsive Performance at Various Reynolds Numbers

The forward travel speed, or Reynolds number in dimensionless form, is one parameter which is known to affect the thrust production and efficiency of an oscillating foil [7]. For a fixed motion amplitude, the oscillation frequency associated with any particular Strouhal number will change as the Reynolds number is varied. For efficient and effective propulsion, it is necessary to operate an oscillating foil within a certain range of Strouhal numbers so that the disturbances applied to the flow by the foil are amplified into a thrust-producing wake [12]. Therefore, the shift in the Strouhal number with respect to the oscillation frequency caused by a change in Reynolds number has implications for the use of flexible foil designs because the frequency ratios within the range of optimal Strouhal numbers will also change.

In the present work, it was expected that the foils would operate with greater propulsive efficiency if the resonant frequency were chosen such that the structural response which provides a beneficial phase and amplitude of the deformation occurred at an oscillation frequency within the optimal range of Strouhal numbers. To test this hypothesis, trials were conducted with each of the foil designs at three different flow speeds. The heave amplitude was set at a constant value of h_0/c=0.125 throughout these trials and no active pitching motion was applied. The measured thrust coefficients and efficiencies are shown in Figures 4.8 and 4.9 respectively. It was anticipated that the foils with lower resonant frequencies would achieve higher efficiencies at the lowest Reynolds number. For this flow speed, the deformation behaviour of these foils which occurs at oscillation frequencies around the expected optimal Strouhal is also believed to be conducive to efficient propulsion. The performance of foils with higher resonant frequencies was expected to improve as the the Reynolds number was increased. However, this trend is not observed and the performance trends and relative differences in the thrust and efficiency among the foil designs are largely unchanged as the Reynolds number is varied.

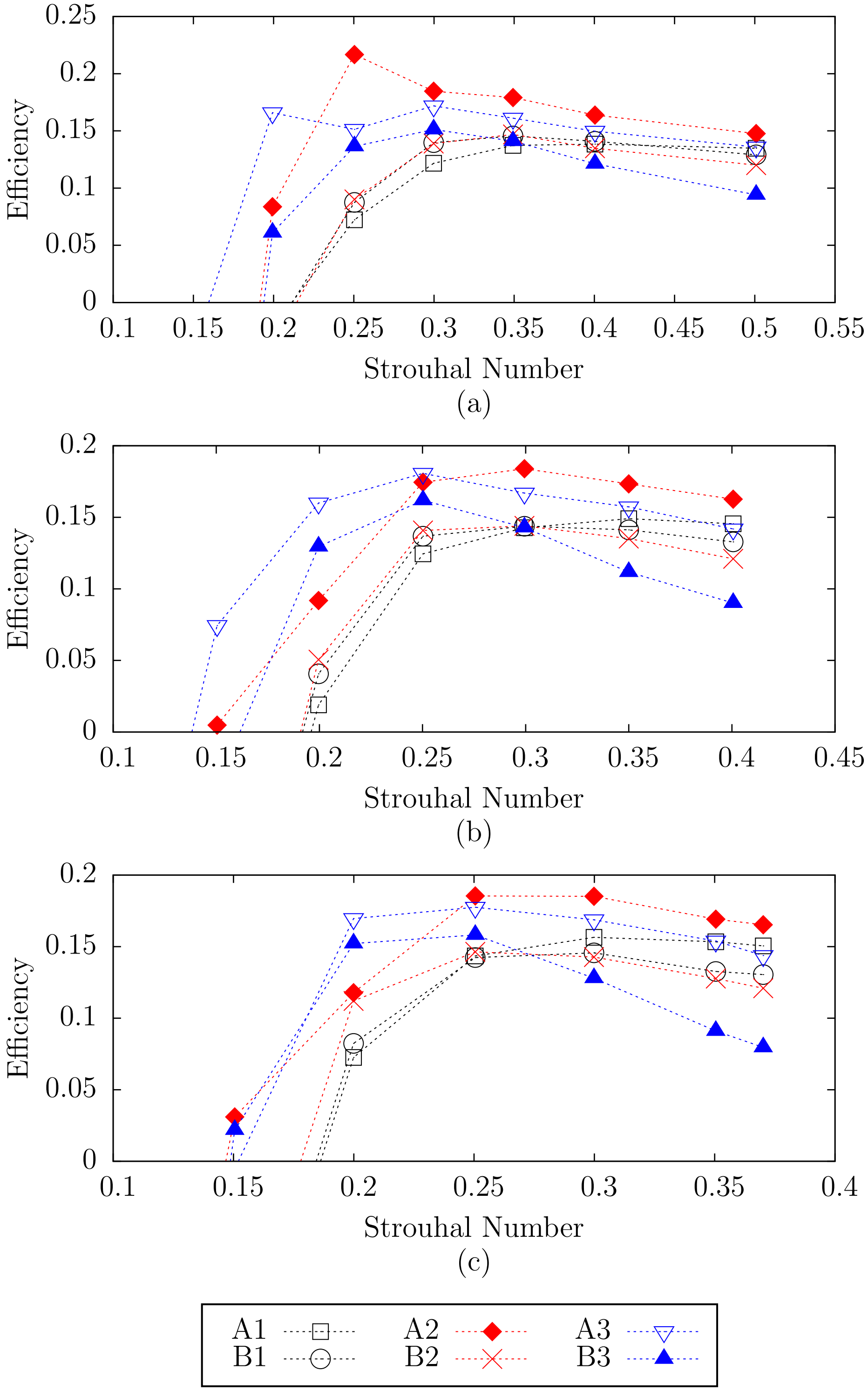

(a)

(b)

(c)

Figure 4.8: Variation of efficiency with respect to Strouhal number compared for various foil designs at (a) *Re*=58 700, (b) *Re*=73 140 and (c) *Re*=81 060.

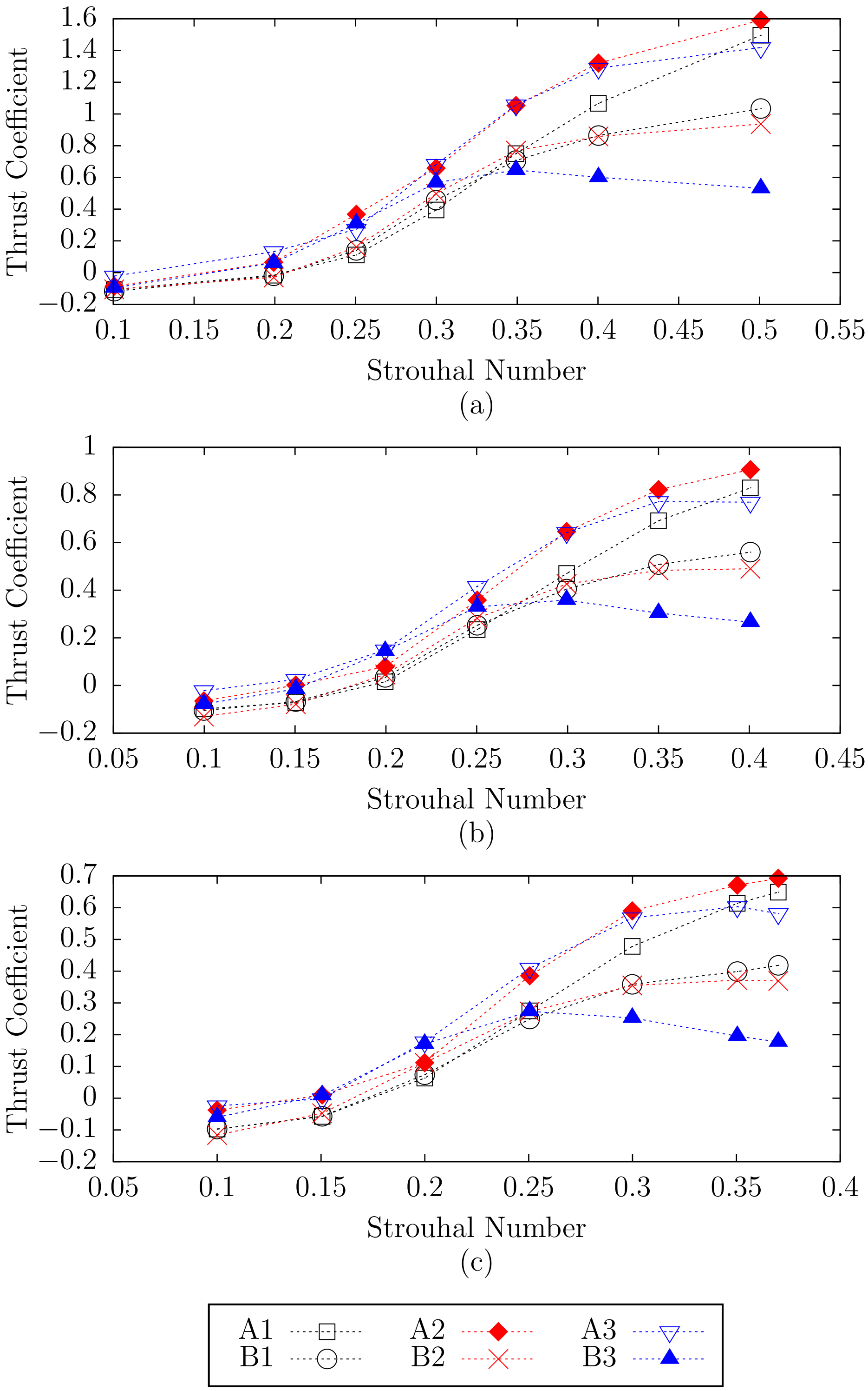

Figure 4.9: Variation of thrust coefficient with respect to Strouhal number compared for various foil designs at (a) *Re*=58 700, (b) *Re*=73 140 and (c) *Re*=81 060.

Due to the effects of the three-dimensional flow around the foils, it is possible that operation at the optimal Strouhal number for the effective development of a thrust-producing wake was never achieved during these trials. The heave amplitude and flow speeds were chosen such that the Strouhal number $St = 0.3$ would occur at the same oscillation frequency as the expected optimal frequency ratio of $f/f_n = 0.8$ for at least one of the foil designs at each Reynolds number. This Strouhal number was targeted because it was identified to lead to efficient propulsion by Anderson et al. [12]. However, this study considered high-aspect-ratio foils. For low-aspect-ratio foils, which are more similar to the design considered in the present work, various authors [17, 19, 22] have reported values for the optimal Strouhal number which vary considerably from this optimum for two-dimensional foils.

The foil deformation may have also interfered with the ability of the foils to achieve high propulsive efficiency by operating in the correct range of Strouhal numbers. The oscillation kinematics were designed to set the Strouhal number during operation based on the amplitude of the heaving motion. However, the Strouhal number based on the the total distance swept by the trailing edge is likely more relevant since the width of the wake will be more similar to this amplitude. Because of the relatively low heave-to-chord ratio of the current design, any bending of the foils would result in a substantial change in the amplitude of the motion of the trailing edge. In fact, during some the trials which were observed by high-speed photography, the trailing edge amplitude was more than twice the heave amplitude. Therefore, even if the Strouhal number $St = 0.3$ would in fact produce an optimal response by the wake, the foil motion may have never actually achieved this effective Strouhal number.

Although a demonstration of improved propulsive efficiency by appropriately matching the structural design and Reynolds number was not possible, the results do indicate that the efficiency is affected by the frequency ratio. Figure 4.10 shows the measured efficiencies of all of the foils at all of the Reynolds numbers plotted against the frequency ratio. For each foil at each Reynolds number, the measured efficiencies have been normalized by dividing by the maximum efficiency observed for that particular combination of foil design and Reynolds number. The maximum efficiencies are generally achieved at a frequency ratio around $f/f_n = 0.8$, indicating that the frequency ratio was properly targeted in the design of the foil structures and oscillation kinematics.

In contrast to the relation between efficiency and frequency ratio, the effect of the Strouhal number on efficiency is less clear. When the same normalized efficiency

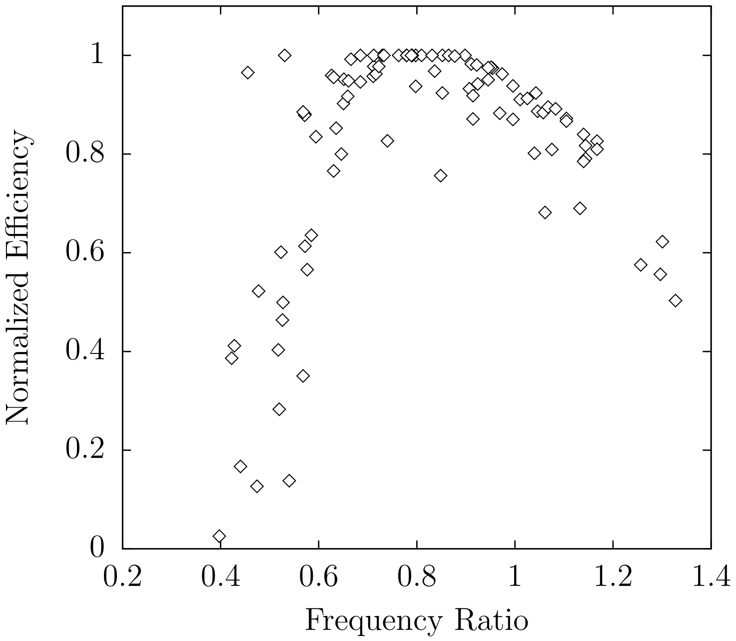

Figure 4.10: Normalized efficiency as a function of frequency ratio for all foil designs and Reynolds numbers considered.

considered in Figure 4.10 is instead plotted against the Strouhal number as in Figure 4.11, there is no particular value which appears to be optimal. At any particular Strouhal number, the normalized efficiency falls somewhere within a relatively wide band depending on the foil structural design and the Reynolds number. This result suggest that the measured efficiencies are more strongly dependent on the frequency ratio than Strouhal number, possibly because the foils were operating outside of the band of optimal Strouhal numbers throughout the entire range of oscillation frequencies.

In order to understand why operation at a particular frequency ratio leads to improved efficiency, it is necessary to consider the structural dynamics of the foils. As discussed in Section 1.4, the optimal frequency ratio may lead to either a beneficial phase between the input motion and the deformation, or a resonant amplification of the input motion. In fact, there is some debate in the literature [31] as to whether it is the phasing or amplification which is more important. In the case at hand, the deformation phase can be observed from the load cell torque signal as discussed in Section 4.1. The phase of the torque signal for all of the foil designs and Reynolds numbers considered in the trials is plotted against frequency ratio in Figure 4.12. It

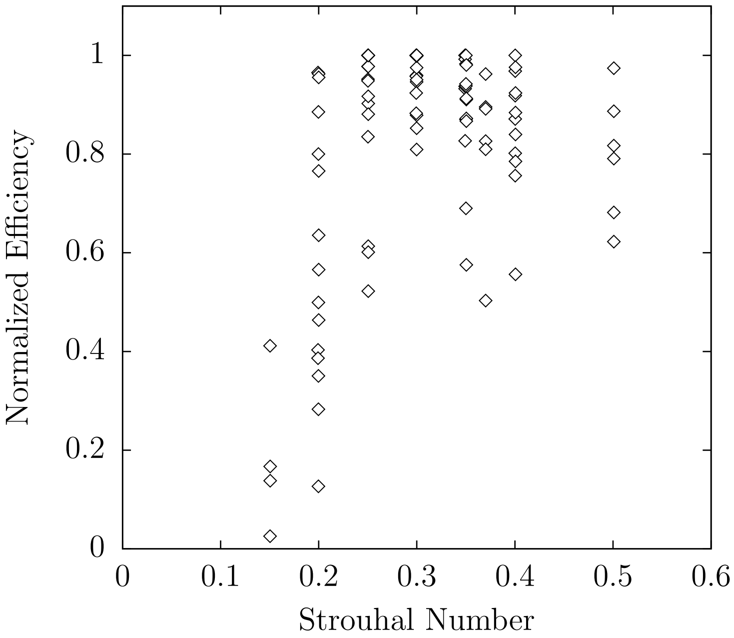

Figure 4.11: Normalized efficiency as a function of Strouhal number for all foil designs and Reynolds numbers considered.

is observed that the evolution of the phase with respect to frequency ratio is fairly consistent in all cases. The deformation phasing may therefore be in part responsible for the consistent relation which is also observed between the efficiency and frequency ratio for all of the foils.

The torque phase which occurs around the observed optimal frequency ratio is approximately $-\pi/2$. As discussed in Section 4.1, this phase is theoretical conducive to efficient propulsion since the maximum deflection occurs when the relative velocity between the foil and the fluid is high, and the deformed shape directs the lift forces to produce forward thrust. Indeed, when the normalized efficiency is plotted against the torque phase in Figure 4.13, the efficiency is generally found to be high at this phase. However, these results do not necessarily indicate that the relatively high efficiency observed for each foil near the frequency ratio which results in this phasing can be attributed to the beneficial phase lag. When the amplitude ratios predicted by the damped-oscillator models fitted for each foil in Section 4.2 are plotted in Figure 4.14, it is found that the peak amplitude ratio is also achieved at a approximately the same frequency ratio which was observed to produce the peak efficiency. The results presented here therefore do not favour either argument as to whether the peak

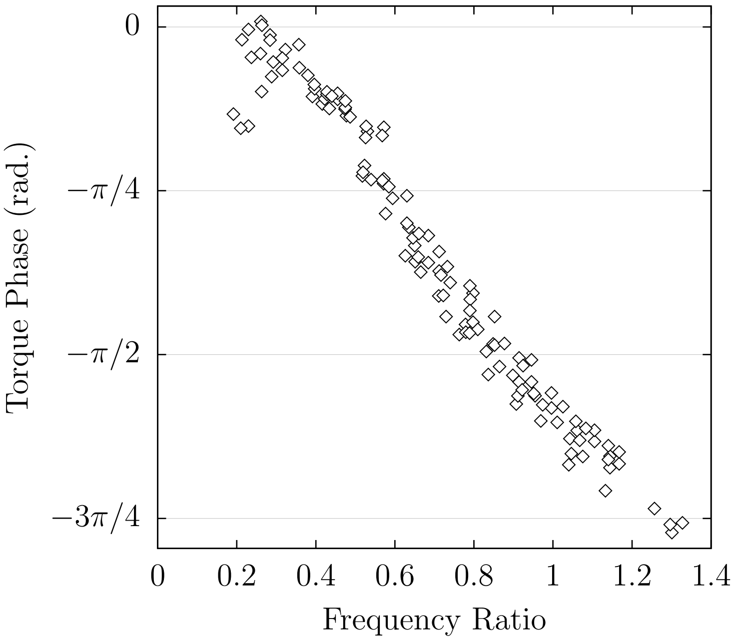

Figure 4.12: Evolution of the deformation phase with frequency ratio for all foil designs and Reynolds numbers considered.

efficiency is achieved through optimal phasing or by resonant amplification of the motion. Instead, it is likely a combination of these factors which lead to the relatively high propulsive efficiency at a particular frequency ratio for the foils considered here.

While the foil resonant frequency has been demonstrated to be a governing parameter in the propulsive performance, it is well known that this structural parameter is in fact a ratio of two quantities: the stiffness and the inertia. It is therefore interesting to be able to examine the relative performance of foils with the same resonant frequency but proportionally different stiffness and inertia. To this end, we extract and compare the results for the foil pairs A2-B1 and A3-B2. The foils within each of these pairs have approximately the same resonant frequency but significantly different stiffness and inertia due to the different reinforcements and embedded masses used in each case. Examining the traces associated with these foil designs in Figures 4.8 and 4.9, it is observed that the heavier and stiffer foils, A2 and A3, achieve higher efficiency and produce greater thrust than their lighter and more flexible counterparts, B1 and B2. The difference in efficiency is small, but the thrust production is substantially higher, indicating that the heavier and stiffer design is much more effective as a propulsion mechanism.

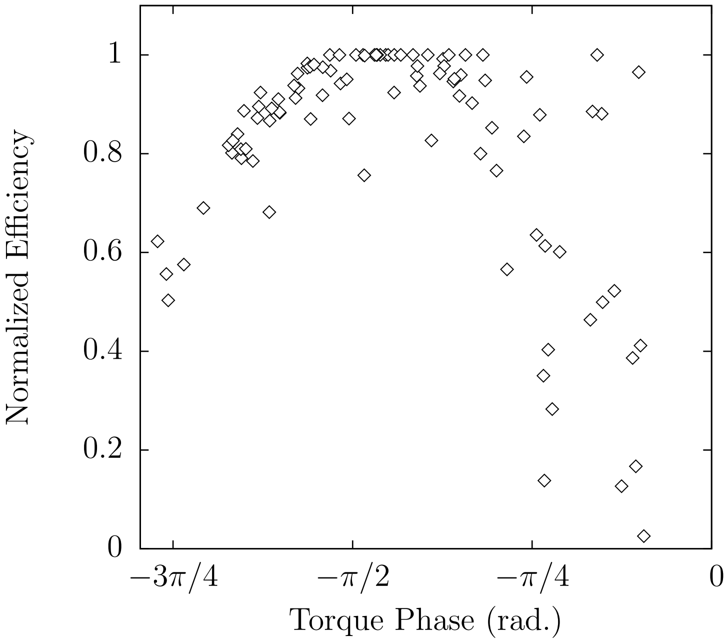

Figure 4.13: Normalized efficiency as a function of deformation phase as observed from the load cell torque signal.

The relatively better performance of the heavier and stiffer foils can be attributed, at least in part, to the smaller damping ratios for these designs. As shown in Figure 4.14, the damped-oscillator models predict that the foils A2 and A3 have higher amplitude ratios than foils B1 and B2 when operating at the same frequency ratio. The greater amplitude of motion results in higher relative velocity between the foil and the fluid and a larger swept area which in turn leads to greater thrust production. In the case of the foil pair A2-B1, the greater motion amplitude of foil A2 is also confirmed by the photographic observation of the trials at $Re = 58\ 700$ as shown in Figure 4.15.

One could also propose the argument that the stiffer and heavier foils achieve better performance by deforming into a more hydrodynamically suitable shape than the lighter and more flexible foils. For example, it could be suggested that the curvature along the chord of the stiffer foils somehow introduces a camber which increases the strength of the bound circulation and thus increases the lift forces. However, an examination of the photographic records does not support this explanation. Instead it is found that when the deflection at the trailing edge of two foils is the same, the foil profiles also follow the same curve along the chord length. As an example, two

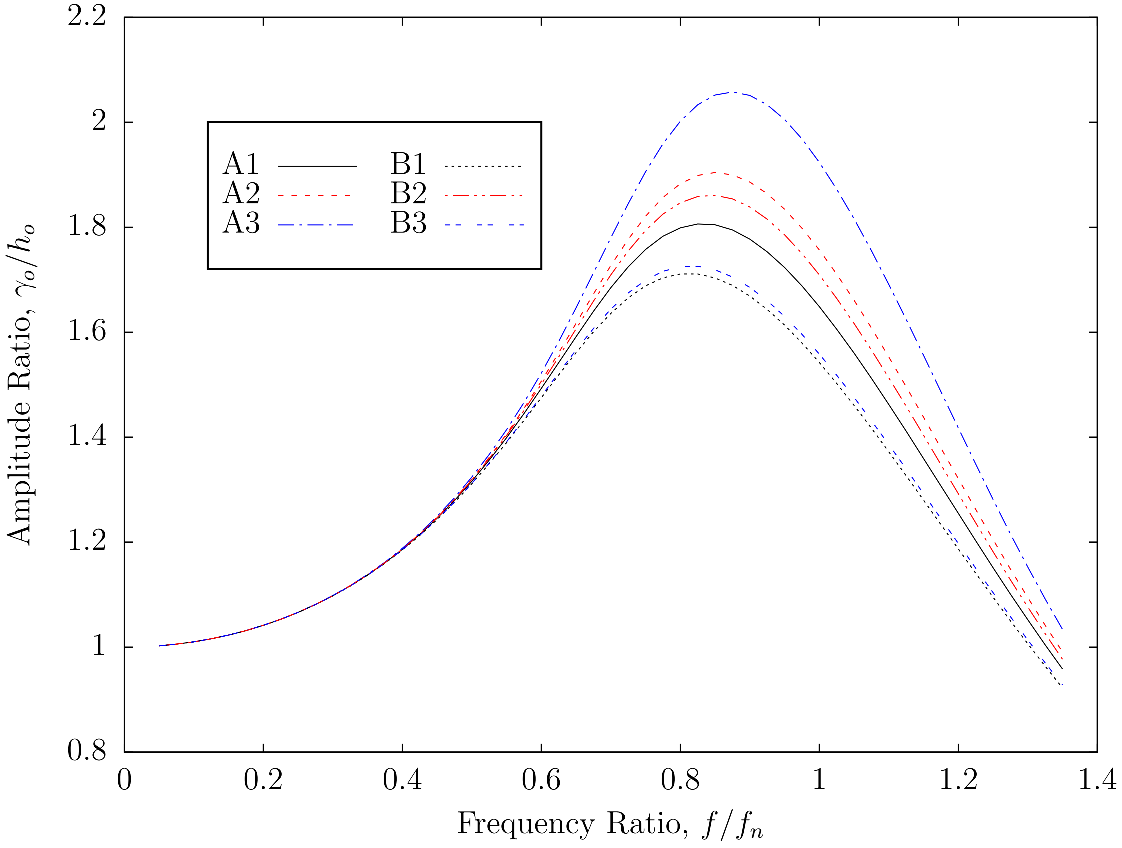

Figure 4.14: Amplitude ratios predicted by the damped-oscillator model for all foil designs over a range of frequency ratios.

frames showing the foils A2 and B1 with the same deflection at the trailing edge were extracted from the recordings taken during the trial at $Re = 58\ 700$ and $St = 0.4$. The detected edges tracing the foil profiles from these frames have been superimposed for comparison in Figure 4.16 and it is shown that the deformed shape of each foil is essentially the same. This result is expected because the theoretical vibration mode shapes for cantilevered beams with and without concentrated mass near the tip are also similar [48]. It is therefore more likely that the discrepancies in propulsive performance between the foils of the same resonant frequency but with different mass and stiffness are attributable to differences in the amplitude of the trailing edge motion rather than any changes in the deformed profile.

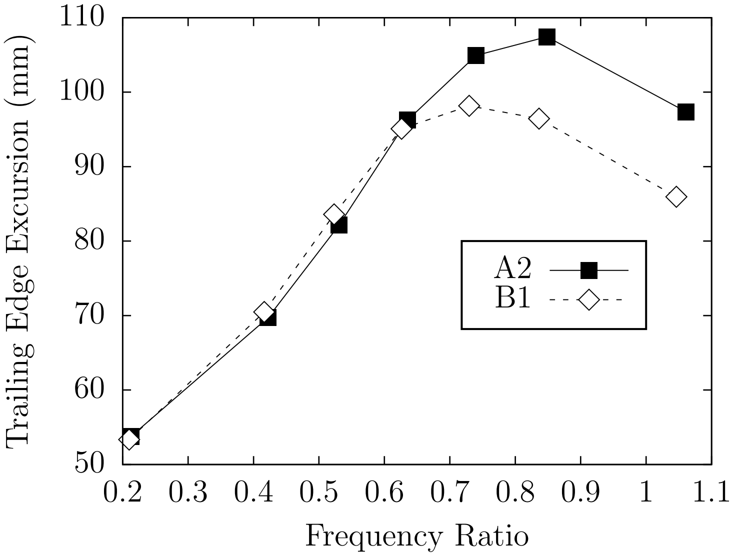

Figure 4.15: Trailing edge excursion determined from the photographic observation of foils A2 and B1 during trials at $Re = 58\ 700$.

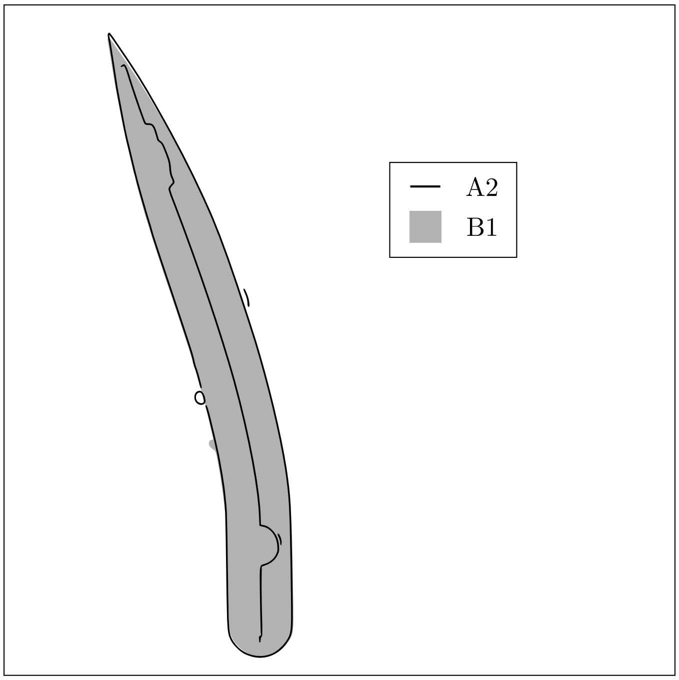

Figure 4.16: Comparison of the photographically observed deformed profiles of foils A2 and B1 with the same deflection at the trailing edge.

4.4 Effect of the Foil Structure on Propulsive Performance at Various Heave Amplitudes

In addition to the propulsion trials at various Reynolds numbers, trials were also conducted with varying dimensionless heave amplitude, h_0/c. All of these trials were conducted at the same Reynolds number $Re = 80\ 060$, and without an active pitching motion. The measured efficiencies and thrust coefficients are plotted in Figures 4.17 and 4.18 respectively. Unlike the case of varying Reynolds number, where the results were similar in each trial, changing the heave amplitude was observed to have a marked effect on the relation between the foil structural properties and efficiency. When comparing the propulsive performance of different structural designs, it is observed that in the lowest amplitude case ($h_0/c = 0.125$), the stiffer "A" group foils develop significantly greater thrust forces and also operate more efficiently. The same result was found in all of the trials at various Reynolds numbers. As the heave amplitude is increased, however, the foils are all observed to approach approximately the same level of efficiency with neither group achieving substantially better performance.

In the low-amplitude trials, and all of the trials at various Reynolds numbers, the greater thrust production of the heavier and stiffer group "A" foils was attributed to greater resonant amplification of the input motion due to lower equivalent damping ratios in the stiffer design. While the resonant amplification of the input motion apparently leads to greater thrust production, the required power input is also increased in order to drive the larger amplitude motion. At low heave amplitudes, the increased output power resulting from the greater thrust apparently exceeds the corresponding increase in input power and the efficiency of the heavier foils is somewhat greater. At higher heave amplitudes the two power increases appear to cancel each other and the efficiency is comparable for both the heavier and lighter designs.

In addition to changing the efficiencies achieved by the different foil designs relative to each other, varying the heave amplitude was also found to affect the trends relating the propulsive efficiency to frequency ratio. When the efficiencies achieved by each combination of structural design and heave amplitude are normalized by the maximum value and plotted against frequency ratio as in Figure 4.19, the peak efficiencies are generally found at approximately the same location as long as the same heave amplitude is considered. When the heave amplitude is increased, however, there is observed to be a shift in the peak efficiency towards lower frequency ratios.

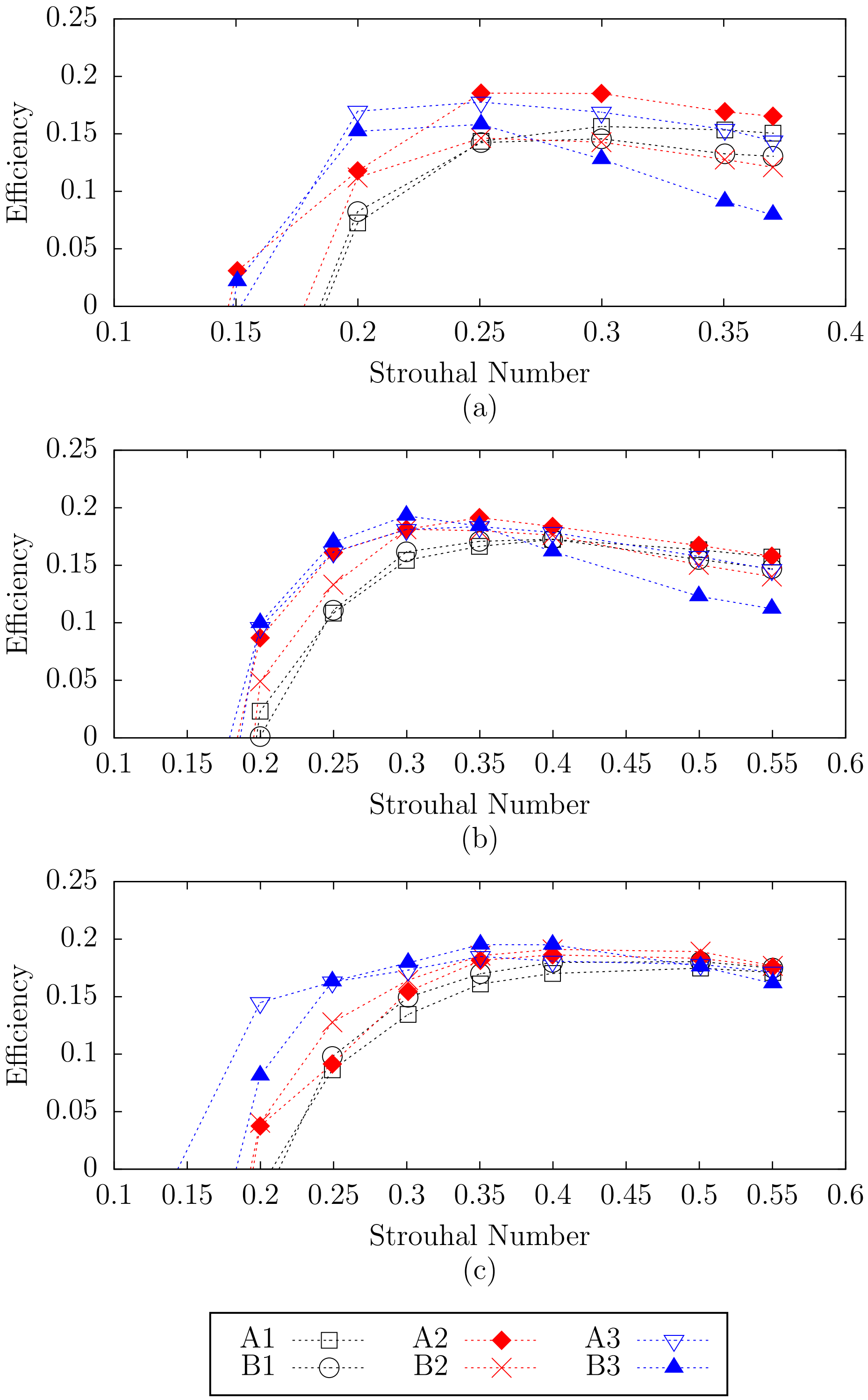

Figure 4.17: Variation of efficiency with respect to Strouhal number compared for various foil designs at (a) $h_0/c = 0.125$, (b) $h_0/c = 0.1875$ and (c) $h_0/c = 0.25$.

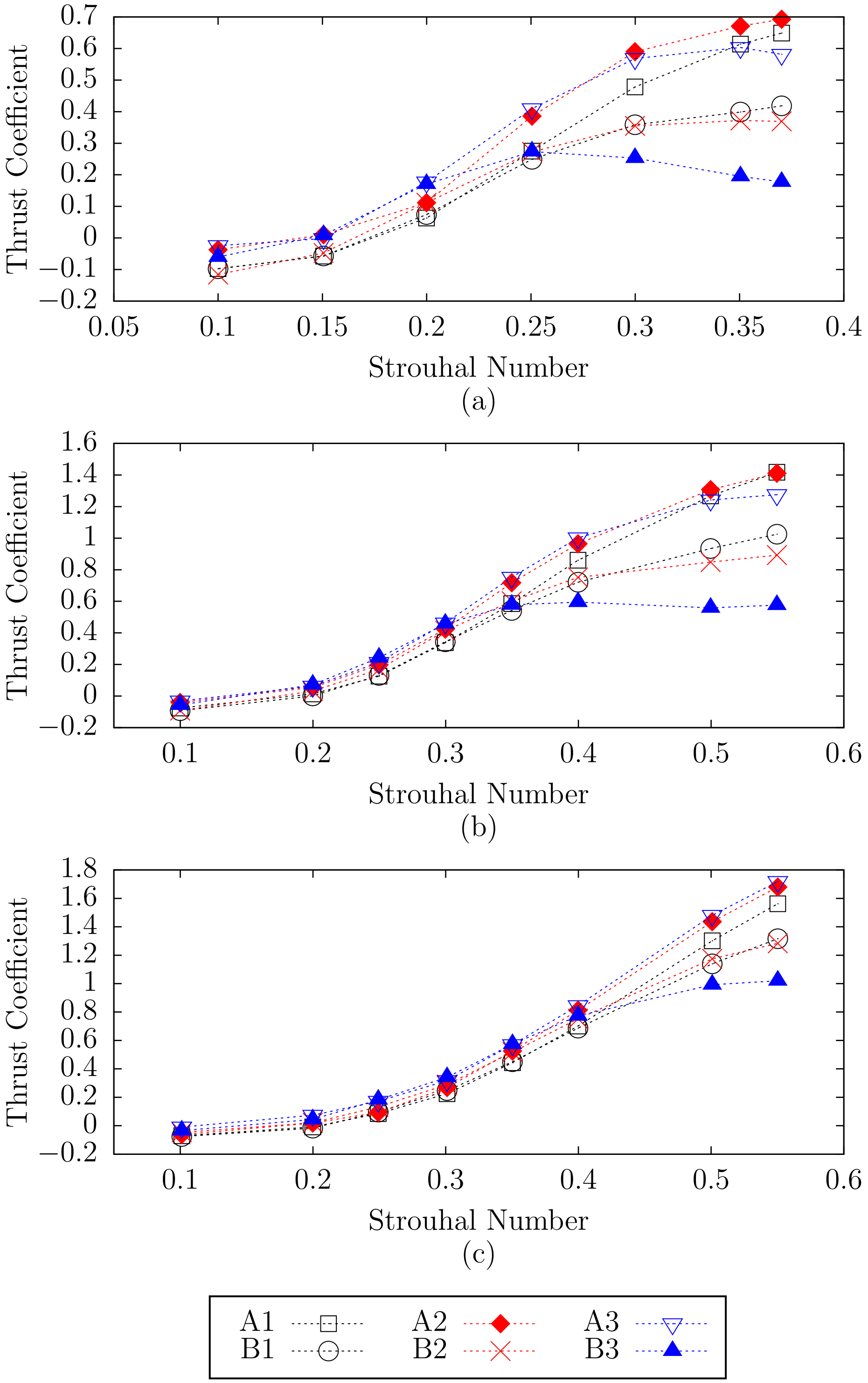

Figure 4.18: Variation of thrust coefficient with respect to Strouhal number compared for various foil designs at (a) $h_0/c = 0.125$, (b) $h_0/c = 0.1875$ and (c) $h_0/c = 0.25$.

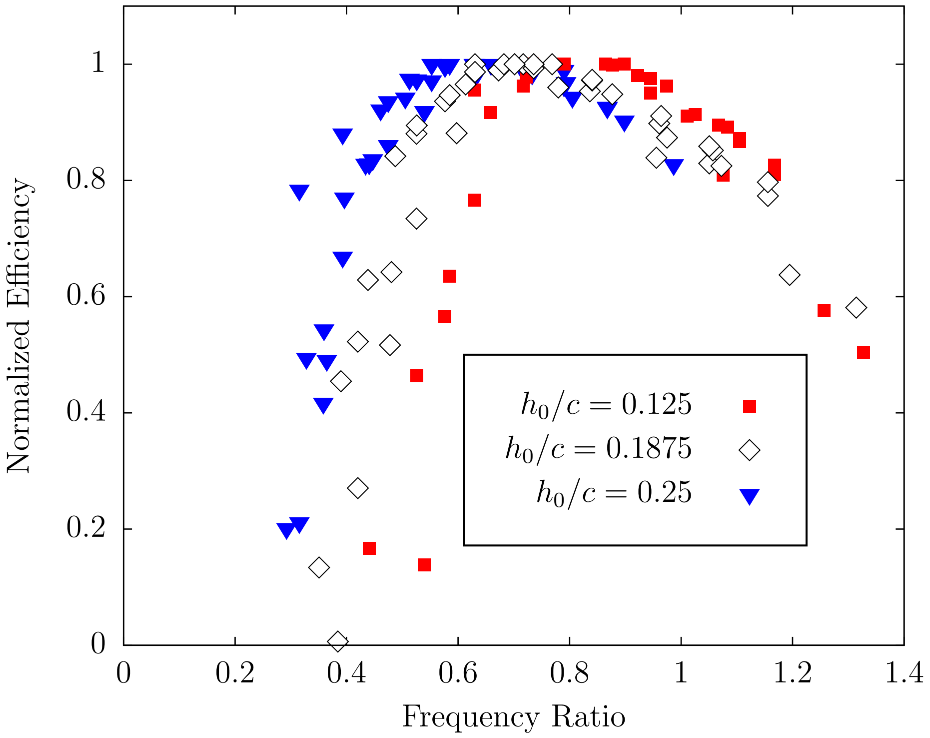

Figure 4.19: Normalized efficiency as a function of frequency ratio for all foil designs at three different heave amplitudes.

It is possible that the shift of the point of peak efficiency towards lower frequency ratios as the heave amplitude is increased can be attributed to a corresponding shift in the band of optimal Strouhal numbers towards lower oscillation frequencies. However, it was observed from the results presented in Section 4.3 that the correlation between the Strouhal number and efficiency is poor and it was speculated that the optimal Strouhal band has been missed entirely by the foil designs and oscillation kinematics considered here. It is therefore reasonable to expect that there are some changes in the dynamic deformation behaviour of the foils which occur when the heave amplitude is varied and that these changes in turn lead to different trends in the propulsive performance. To investigate this possibility, we first examine the trends in the variation of the deformation phase lag with frequency ratio as the heave amplitude is increased. Again, the phase lag has been observed indirectly based on the torque signal from the load cell as discussed in Section 4.1. The results plotted in Figure 4.20 show when the heave amplitude is increased, the phase lag develops more quickly at low frequencies, but the measurements approach the same trend at higher frequency ratios.

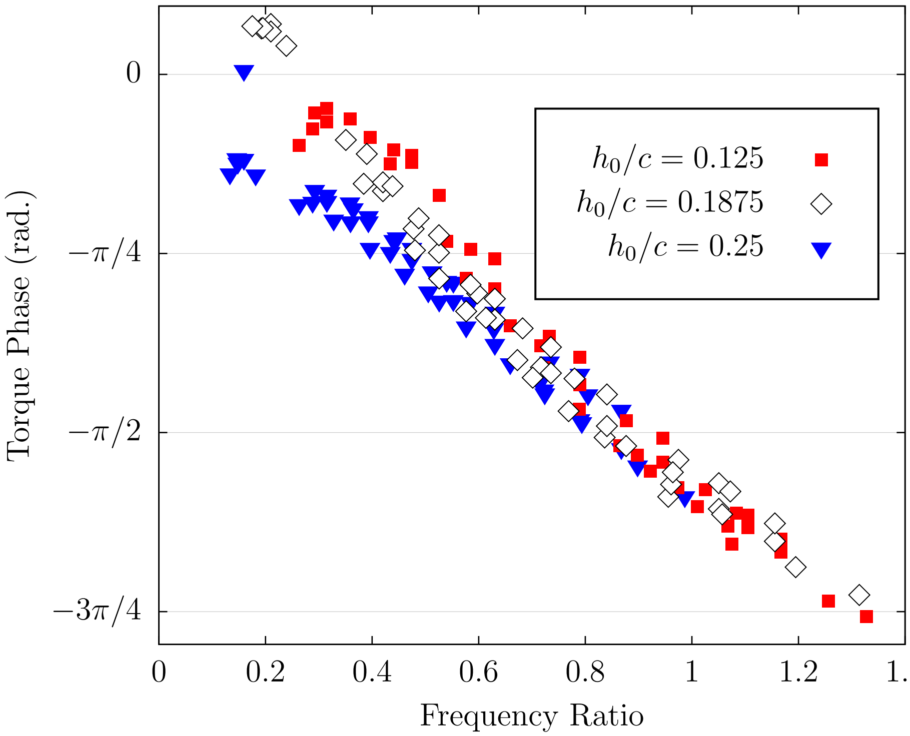

Figure 4.20: Evolution of the deformation phase as a function of frequency ratio for all foil designs at three different heave amplitudes.

The damped-oscillator model developed in Section 3.5 predicts a trend in the deformation phase similar to what was observed from the measurements in Figure 4.20 when the amplitude of the input motion is increased. This amplitude appears in the denominator of Equation 3.16 for the *quadratic damping frequency*. Therefore, if the heave amplitude is scaled by some factor, this fitted frequency for any given foil design should be multiplied by the reciprocal factor. In Figure 4.21, the predicted damping ratios, deformation phases and amplitude ratios predicted by the model fitted for the foil B3 are plotted for three different input motion amplitudes. Essentially, it is found that because the velocity of the motion increases when the amplitude is increased, the damping forces also become greater and the equivalent damping ratio increases. The increased damping ratio leads to faster development of the phase lag at low input motion frequencies. The higher damping ratio also reduces the peak amplitude ratio and causes the location of the peak to shift towards lower frequency ratios. Since both the peak amplitude ratio and the development of a suitable deformation phase lag are observed to shift towards lower frequency ratios as the heave amplitude increases, it is difficult to attribute the corresponding shift in the peak efficiency to either of these two changes. Again, similar to the findings from the trials at various Reynolds numbers, it is likely a combination of beneficial deformation phasing and resonant amplification of the input motion which leads to the relatively high efficiency at a given frequency ratio.

While the difference in efficiency between the foils with equivalent resonant frequency within the pairs A2-B1 and A3-B2 was found to diminish as the heave amplitude was increased, the heavier and stiffer group "A" foils still produced greater thrust and thus achieved higher overall propulsive performance. However, a slight decrease in the discrepancy in thrust production was also observed. As a measure of the difference in thrust production between the two foils A3 and B2, the relative difference in thrust coefficient given by

$$C_{T,rel} = \frac{C_{T,A3} - C_{T,B2}}{C_{T,B2}} \tag{4.2}$$

can be considered. This relative difference has been plotted against the frequency ratio in Figure 4.22 and is found to be generally smaller as the heave amplitude is increased. For example, at frequency ratios around $f/f_n = 0.8$, the foil A3 produces approximately 37% greater thrust than B2 when the heave amplitude is set to $h_0/c = 0.125$, but when the amplitude is $h_0/c = 0.25$ the difference is only 26% at the same frequency ratio. The findings are similar when comparing the thrust production of the foils A2 and B1. Although these results indicate that the increased thrust production associated with use of stiffer and heavier foils is reduced when the heave amplitude is increased, further experiments over a wider range of amplitudes are necessary to confirm this trend. In the cases considered here, the changes in the relative thrust coefficient with varying heave amplitude are subtle and the thrust coefficients at the low amplitude are subject to considerable uncertainty due to the relatively small streamwise forces.

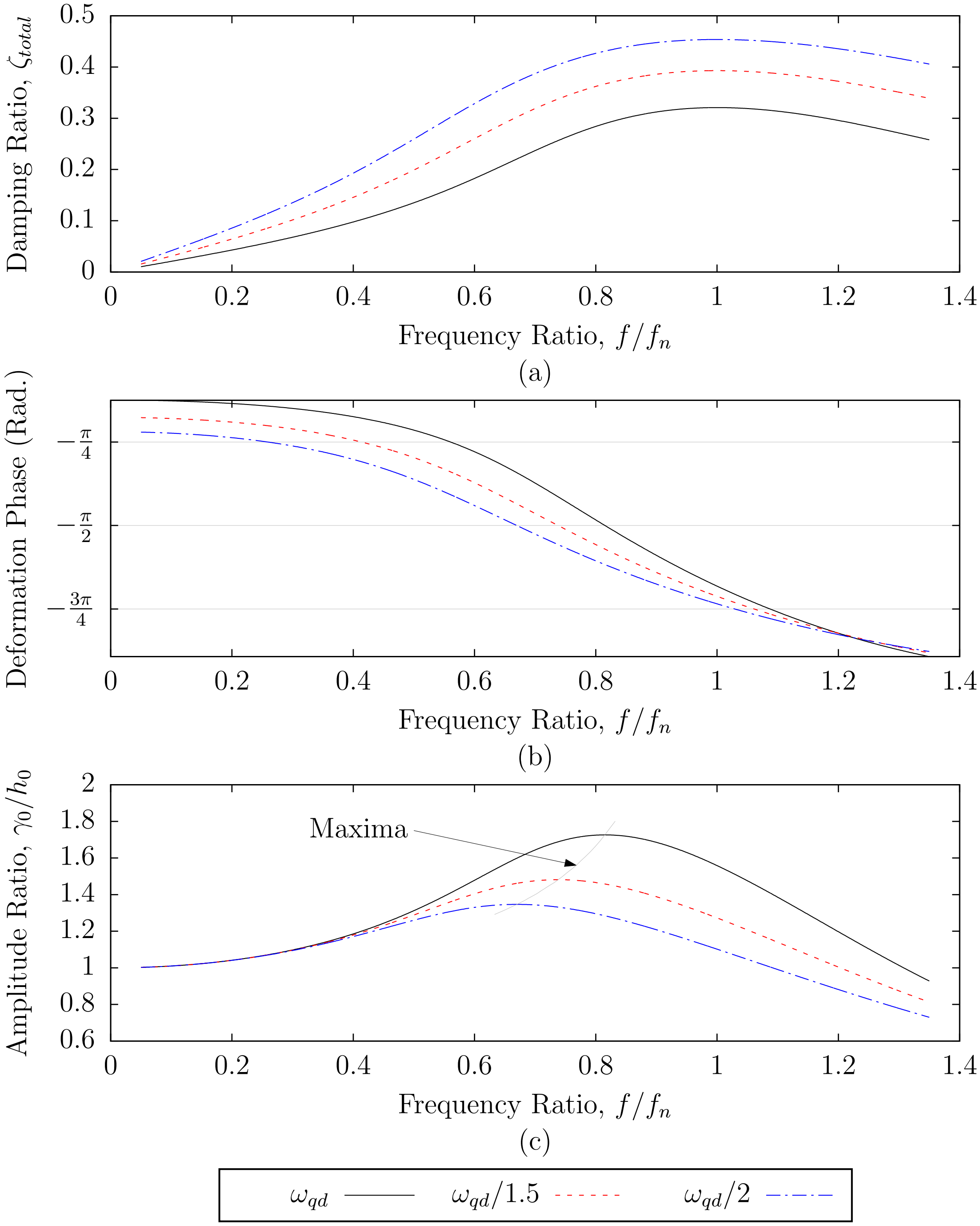

Figure 4.21: Predicted changes by the damped-oscillator model in the trends of (a) equivalent damping ratio, (b) deformation phase and (c) amplitude ratio with respect to frequency ratio when the *quadratic damping frequency* is scaled due to scaling of the input motion amplitude by a reciprocal factor.

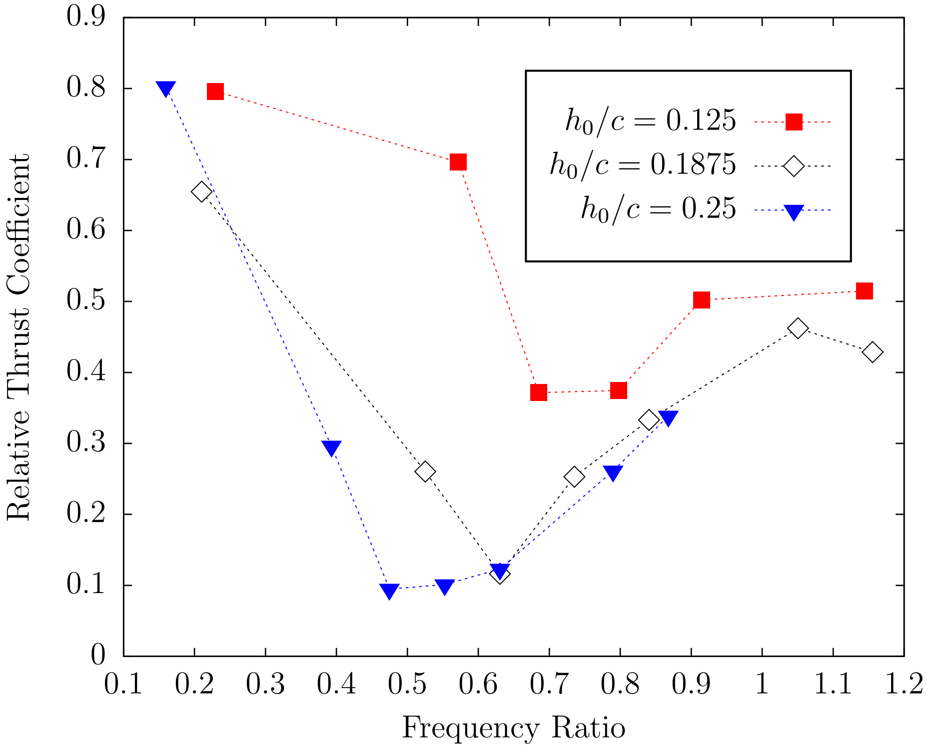

Figure 4.22: Variation with respect to frequency ratio in the relative difference between the thrust coefficients of the foils A3 and B2 at three different heave amplitudes.

4.5 Propulsive Performance of Foils with Combined Active Pitch and Heave Motions

In addition to the heave-only trials conducted at various Reynolds numbers and heave amplitudes, a set of trials was conducted where the foil was actively rotated in a pitching motion. In these trials, the heave amplitude was set to $h_0/c = 0.125$ and the flow speed was set to establish a Reynolds number of Re=80 060. The pitching amplitude was set to a constant $\theta_0 = 10°$ for all frequencies considered. The phase of the pitching motion with respect to the heaving motion was set to $\phi_{pitch} = -\pi/2$. These kinematics were chosen to establish the same trailing edge excursion for a hypothectical inflexible foil as the mid-amplitude ($h_0/c = 0.1875$) case considered during the trials at various heave amplitudes.

Although the chosen combined pitching and heaving kinematics were expected to result in a similar wake width to the mid-amplitude heave-only trial, the propulsive performance measured in each case is considerably different. The measured efficiencies and thrust coefficients for all of the foils in the active pitch trials are plotted in Figures 4.23 and 4.24 respectively. In these figures, the Strouhal number against which the results are plotted is based on the trailing edge excursion of a theoretical rigid foil rather than the heave amplitude.

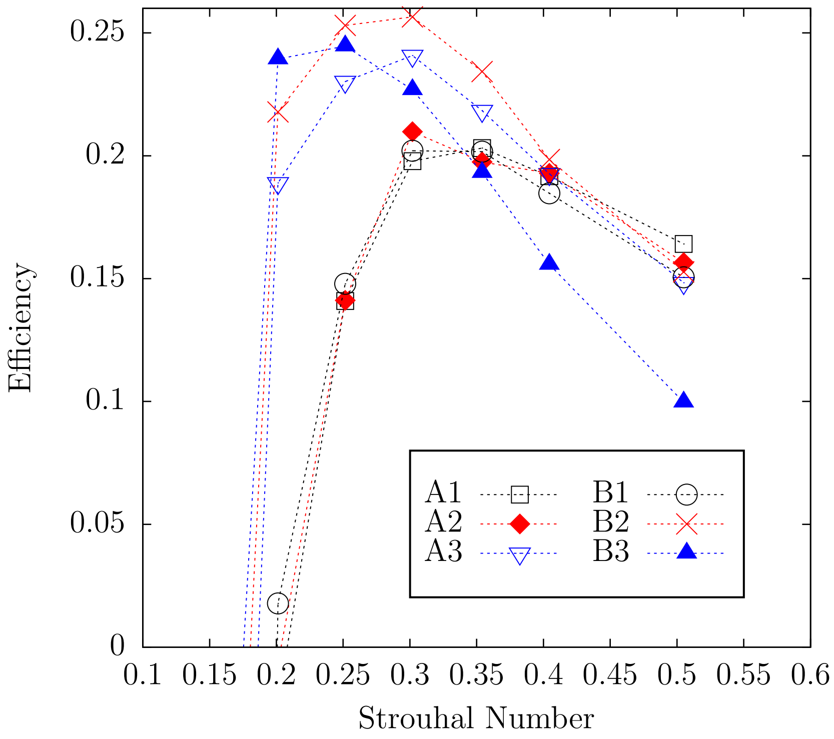

Figure 4.23: Variation of efficiency with respect to Strouhal number compared for various foil designs during a propulsion trial with an active pitching motion.

One of the most striking differences between the results obtained from the trials with an active pitching motion presented in Figures 4.23 and 4.24 and those for the heave-only trial with an equivalent trailing edge amplitude shown in Figures 4.17*b* and 4.18*b* is that the efficiency is considerably higher in the active pitch case while the thrust production is much lower. The change in performance in particularly marked for the foils A3, B2 and B3. This change is observed because the angle of attack between the foil and the fluid is smaller in the active pitch case. For both the heave-only and combined heave and pitch motions, the foil deflection will act to reduce the angle of attack during some portion of the oscillation cycle, depending on the

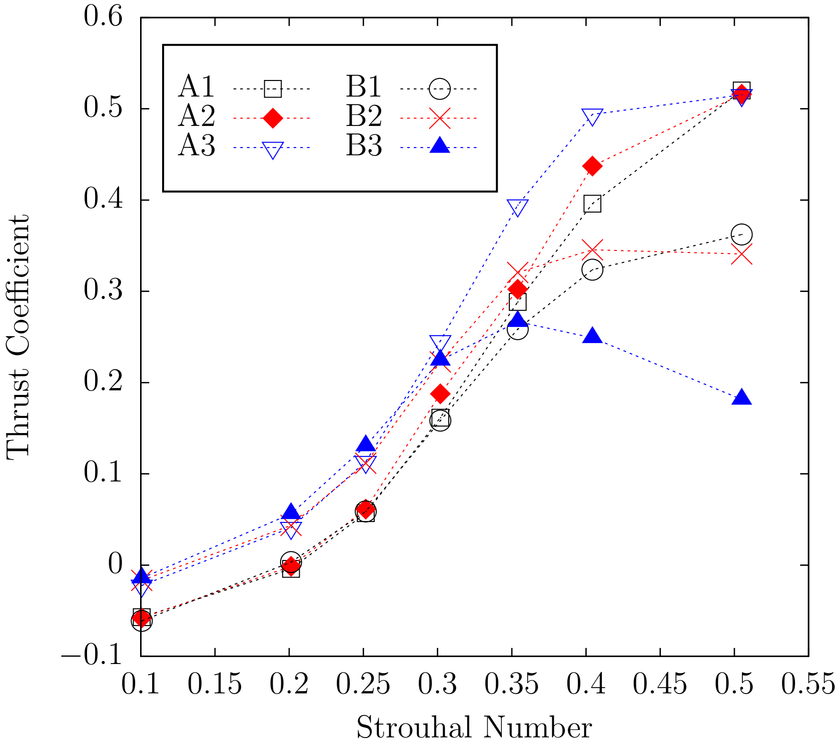

Figure 4.24: Variation of thrust coefficient with respect to Strouhal number compared for various foil designs during a propulsion trial with an active pitching motion.

deformation phasing. When an active pitching motion is applied, however, there is an additive effect of the active rotation and the deflection which both act to reduce the angle of attack making it lower as compared to the heave-only case. For the foil design considered here, there is also portion of the foil chord ahead of the pitching axis which is relatively short and stiff and is not expected to have deflected appreciably during the propulsion trials. In the heave-only trials, this section of the foil chord therefore remained roughly perpendicular to the heaving motion, establishing a very high angle of attack at the leading edge. In the case of the trials with an active pitching motion, this section of the chord would have been rotated to reduce the angle of attack at the leading edge. When the angle of attack is lowered, the drag coefficient and the projected area of the foil to the oncoming flow are reduced which results in smaller drag forces resisting the heaving motion. The corresponding decrease in the power required to drive this motion is apparently more than sufficient to compensate for the added energy input required to actively rotate the foils. The reduced power input in turn leads to improved efficiency. However, when the angle of attack is reduced, the strength of the bound circulation established on the foil is lower and the lift forces decrease. The smaller lift forces in turn lead to the reduced thrust production observed during the experiments.

Developing an understanding of the relationship between the foil structural dynamics and the propulsive performance becomes somewhat more complicated for the propulsion trials with combined heave and pitch motions as compared to the case of a heave-only motion. The difficulties arise for three reasons. First, when the foil is actively rotated, the motion of the foil chord relative to the heaving motion is established by the rotation in combination with the foil deformation rather than by the amplitude and phase responses of the foil structure alone. Consequently, a more complicated motion profile is expected. Second, the deformation behaviour will be excited to varying extents by both the heave and pitch motions which act out of phase with each other. It is therefore more difficult to predict of the response of the deformation to the input motion. Finally, in addition to the added complexity in predicting the motion of the bending foil chord, it also becomes more difficult to observe the deformation behaviour because the load cell torque signal is generated by both the bending moment which deforms the foils and also by the torque required to accelerate the rotational inertia as the foils are actively moved in a pitching motion. The phase of the torque signal with respect to heaving motion is therefore no longer necessarily indicative of the phase of the deformation with respect to this motion as it was in the heave-only case. Because of these complications in predicting and observing the deformation of the foil, the discussion presented here regarding the effect of the foil structure on propulsive performance is speculative rather than presenting definite conclusions.

It is observed in the results presented in Figure 4.24 that the heavier and stiffer "A" group foils produce greater thrust forces, similar to the heave-only cases. The trends in the efficiency shown in Figure 4.23 however, are considerably different. It is found that the three foils with the lowest resonant frequencies achieve higher efficiency than the other three foils which all achieve approximately the same lower level of efficiency. This result may suggest that for the foil designs with lower resonant frequencies, the foil deformation and the dynamics of the wake somehow act together constructively to improve the propulsive efficiency. For example, it is possible that these foil designs amplify the input motion to a greater extent at low frequencies near to the optimal Strouhal where the disturbances applied by the foil to the flow lead to the effective development of a thrust-producing jet. However, the amplification must not have been so large as to move the effective Strouhal number beyond the optimal range for efficient propulsion as in the heave-only trials. While this explanation is possible, it cannot be verified conclusively from the experimental results because there is no observation of the foil deformation or flow structures available to demonstrate that the foils with lower resonant frequency are in fact producing a beneficial amplification of the input motion or that the development of a jet-like wake structure occurs most effectively at the same Strouhal number where the peak efficiency is observed.

4.6 Implications of the Performance Trends for the Design of Practical Propulsion Systems

The foil design considered in the experiments for this study was chosen to fit within the dimensions and capabilities of the water tunnel and motion system used for the propulsion testing rather than to emulate the design of any kind of practical propulsion system, either biological or mechanical. The results obtained from these trials however, do demonstrate four performance trends which may be useful to consider in the design of a practical propulsion system, even if the actual geometry or structure of the prototype is substantially different than the design considered here.

First, it was found that quadratic damping action due to fluid drag is one of the governing phenomena in the structural deformation of a flexible foil. This result indicates that it is important to account for this action in design-stage calculations to predict the structural dynamics of flexible foil. Although the model which was developed in this study includes a quadratic damping element, it will likely not be useful for design calculations because the damping parameters must be fitted based on experimental measurements which would not be available at the design stage. Additionally, the model has not considered the spatial variation of the forces and motions of the foil by replacing the continuous distribution of mass, stiffness and damping with a single-degree-of-freedom system. This approximation makes the model unsuitable for quantitative predictions of the amplitude of the deflection.

Second, the performance of massive and stiff foils was found to be different than that of less massive and more flexible foils of the same resonant frequency. These differences arise because the forces resulting from the quadratic damping action become smaller relative to the inertial and elastic forces as the mass and stiffness increase. Although the frequency ratio and Strouhal number are the same for any given input motion frequency, the difference in damping ratio for heavier and lighter foils makes the structural response and of these foils different. A lighter foil, which is more heavily damped, will have a greater deformation phase lag, but smaller absolute amplitude of the motion. It was found that the greater amplitude of the motion for the heavier foils leads higher thrust production, and for small heaving amplitudes the heavier foils also achieved higher efficiency.

The improved thrust generation and efficiency of the heavier foils was unexpected considering the results reported previously by Yin and Luo [33] who also tested foils with equivalent resonant frequencies but varying levels of inertia. In this work, it was found that the thrust production of the lighter foils was higher up to a frequency ratio of approximately $f/f_n = 0.5$ and that the lighter foils achieved higher efficiency at all frequency ratios considered. However, this study approached the problem using numerical simulations. Consequently, the authors were not limited by the limitations of physical materials and were able simulate the operation of foils with much larger differences in inertia than what was possible in the current experimental work. It is therefore possible that the heavier foils in the work of [33] had much lower equivalent damping ratios than the lighter ones and did not develop the appropriate deformation phase lag for efficient or effective propulsion until reaching relatively high frequency ratios. The work of [33] also used a much higher heave amplitude of $h_0/c = 1.25$, than the maximum heave amplitude of $h_0/c = 0.25$ considered in the present work. In the present work, it was found that the performance benefits associated with heavier foils diminished to some extent as the heave amplitude increased. The difference between the heave amplitudes considered in the two studies may therefore further explain the discrepancy between the observed effects of the foil inertia on thrust generation and efficiency.

The use of embedded masses within a foil to adjust the damping ratio and resonant frequency is a peculiar design which was contrived for the current experimental tests and it is unlikely to find application in practical propulsion systems. Even though the heavier foils were observed to be more effective for propulsion by achieving comparable or higher efficiency than the lighter foils while also producing more thrust, contradictory findings have been reported in other works [33,34]. The effect of inertia on performance is therefore variable and designers should consider cautiously whether added inertia would be useful in any particular design. Furthermore, in most practical cases it is desirable to minimize the mass of the vehicle to improve the payload capacity and reduce the energy input required for acceleration. The addition of embedded masses within a vehicle's propulsion system would counterproductive towards achieving this objective. If it is expected that increasing the inertia of any particular foil design is necessary to lower the resonant frequency or reduce the damping ratio, it is suggested that this design change be accommodated by repositioning structural elements such as reinforcing battens rather than deliberately adding embedded masses for that purpose.

As a third principal finding, the relation between efficiency and frequency ratio was reasonably consistent for all of the foil designs. Conversely, the efficiency achieved at any given Strouhal number relative to the maximum measured value for a given combination of foil structure and Reynolds number was found to vary substantially depending on the foil design. This result indicates that appropriately matching the foil resonant frequency to the operating conditions should be one of the main considerations at the design stage of a propulsion system. It is unclear whether the relatively high efficiency observed at a given frequency ratio arises due to the resonant amplification of the input motion at this frequency, or due to a beneficial phase between the foil deformation and the input motion which establishes the appropriate angle of attack. However, it is clear that the structural dynamics play an important role in the propulsive performance of the foils. The frequency ratio which resulted in the peak efficiency was found to be remain roughly constant as the Reynolds number varied but was observed to shift to a lower value as the heave amplitude increased. The change in the optimal frequency ratio was attributed to a corresponding shift in the frequency ratio which produced the greatest resonant amplification of the input motion and also to the development of a beneficial deformation phase lag at lower frequency ratios in the high-amplitude case.

Since the foils achieve peak efficiency when operating at a certain frequency ratio, and it is known from previous works [12] that a certain range of Strouhal numbers leads to efficient propulsion through the rapid amplification of disturbances in the flow to form a jet-like wake, it was expected a distinct improvement in efficiency would be observed if the motion amplitude, flow speed and foil resonant frequency were chosen such that the optimal Strouhal number and frequency ratio occur for the same oscillation frequency. However in the results obtained here, the peak efficiencies achieved by the foils of different resonant frequencies relative to each other remained essentially unchanged as the flow speed was varied. Even though it was not demonstrated to be possible to adjust the foil designs for improved efficiency in the present work, it is still reasonable to expect that such adjustments are possible. When the efficient operation at a given flow speed is considered as a design goal, it is important that the wake dynamics be properly understood. In the current study, the correct optimal Strouhal number, considering the particular kinematics and geometry of the foils, was not known and the Strouhal number was targeted based on theoretical and experimental results obtained for two-dimensional foils. The effective width of the wake was also likely larger than what was assumed at the design stage due to the foil deformation. To properly design foils for operation at a given flow speed, the wake dynamics and effective wake velocity profile should have been considered more carefully.

Finally, as a fourth observation, it was found that combining active pitching and heaving motions leads to improved propulsive efficiency as compared to the cases which used a heaving motion alone and relied on the passive deformation of the foil to orient it at a proper angle of attack with respect to the fluid flow. However, the active pitching motion lowered the thrust production. Even in the presence of an active rotation to establish the proper angle of attack, the dynamic deformation of the foil was still found influence the propulsive performance. Given that a drive mechanism which can produce a combined rotation and translation with the proper phasing between the two motions will be more complicated and likely heavier than a mechanism which produces a heaving motion alone, designers should consider whether the addition of the combined motion is consistent with the design goals for the vehicle. If it is necessary to develop high thrust forces, then addition of an active pitching motion may not be beneficial. If high efficiency for long distance travel is required, an active pitching mechanism combined with a foil structure of the appropriate mass and stiffness will be useful to achieve this objective.

Chapter 5

Conclusion

An experimental study has been conducted to examine the effect of the structural properties and oscillation kinematics of an oscillating-foil propulsion mechanism on its thrust generation and efficiency. Model foils with the same external geometry but varying mass and stiffness were constructed by embedding an internal metal structure within a silicone rubber encapsulant. The foils were then driven in an oscillating motion in a water tunnel by a computer-controlled servo-motor motion system while the forces and torque acting on the foils were measured using a three-axis load cell. The oscillation frequencies and amplitudes were adjustable by changing the program controlling the motion system, while the Reynolds number could be adjusted by changing the flow speed in the tunnel. The thrust coefficient and propulsive efficiency of the foils was calculated based on the measurements recorded in each trial. In a limited number of cases, photographic recordings were made to observe the deformation of the flexible foils directly. It was found that in other cases, the deformation could be observed indirectly by measurement of the bending moments. Based on the experimental results, it was possible to draw four main conclusions.

First, in agreement with previous works, it was found that the quadratic damping action due to fluid drag is one of the main physical phenomena which governs the foil deformation. This result was determined by comparing the measured phase lag between the foil deformation and the input motion with the phase lag predicted by single-degree-of-freedom oscillator models with various forms of damping. The agreement between the model predictions and the measurements improved considerably when a quadratic damping element was included compared to models which only included linear or hysteretic damping. The single-degree-of-freedom oscillator model was also able to predict the amplitude response of the foil motion in a qualitative sense.

Secondly, the performance of heavier and stiffer foils was found to be different compared to lighter and more flexible foils of the same resonant frequency. The difference in performance is attributed to the lower effective damping ratio in the case of the heavier foils. The lower damping ratio allowed for greater resonant amplification of the input motion which in turn resulted in higher thrust production with similar efficiency as compared to the lighter foils with greater effective damping. This result essentially indicates that the more massive foils are more effective propulsion mechanisms. Previous studies have produced contradictory findings, demonstrating improved propulsive performance by lighter and more flexible foils. Both results should therefore be interpreted with some caution if applied to the design of practical propulsion systems. It is likely important that designers of such systems consider the changes to both the amplitude and phase responses of a given foil design as its inertia is changed in order to find an optimal combination of mass and stiffness which will lead to effective thrust production and high efficiency.

As a third finding, a consistent trend relating the propulsive efficiency to the frequency ratio was observed for all of the foil designs. For any particular design at a given frequency ratio, the efficiency relative to the peak efficiency achieved by that particular design was found to be similar. While the same trend was observed at each Reynolds number considered, the frequency ratio which lead to the peak efficiency was found to shift towards a lower value as the heave amplitude was increased.

Finally, it was found that by using an active rotation or pitching motion, the propulsive efficiency was improved considerably compared to the cases where the foils were moved in a heaving only motion and the system relied on the passive bending of the foils to establish the relative orientation between the foil chord and the flow. However, the thrust production in the cases with active pitching motion was found to be lower.

5.1 Recommendations for Future Work

The findings reported in this work raise additional research questions in the field of oscillating-foil propulsion which are interesting to investigate both from the standpoint of improving the theoretical understanding of the fluid-structure interaction associated with these propulsion systems and also as a means to develop more effective practical propulsion systems. Some of these questions and suggestions for possible approaches to resolve them are discussed here.

It was observed that the propulsive efficiency follows a consistent trend with respect to the frequency ratio for all of the foil designs considered here. It is expected that the relatively higher efficiency at a given frequency ratio results from a combination of the development of the appropriate phase lag between the actuating motion the passive deformation along with resonant amplification of the input motion by the deformation. It would also be interesting assess the effect of the deformation phase and motion amplitude on the wake structure to determine whether optimal phasing or larger amplitude motions encourage the development of a thrust-producing jet, similar to what has been observed by operation at the appropriate Strouhal number for rigid foils. To address this question, quantitative flow visualisation methods such as particle image velocimetry could be used to record the wake structure for a foil operating at various frequency ratios where relatively higher and lower efficiencies were observed. It would also be worthwhile to compare the wake structures of two foils of the same resonant frequency but different mass and stiffness to help explain the greater thrust development in the case of the more massive foil. Because the flow over the foils considered for this study likely includes significant three-dimensional components, the analysis by particle image velocimetry should likely be accompanied by some other technique such as dye visualisation, or conducted at multiple parallel planes in order to develop some understanding of the spanwise variation in the flow structure. Alternatively, models with a higher aspect ratio and end plates could be constructed to reduce the spanwise flow, although this approach would complicate the experimental apparatus.

The single-degree-of-freedom damped-oscillator model developed in this work was useful to understand the structural dynamics of the foils and therefore to interpret the observed trends in propulsive performance but is not expected to be effective for design work and predicting the performance of a prototype foil. For this model, it was necessary to the determine damping parameters empirically by fitting the predicted phase response to experimental measurements for a foil with a known resonant frequency. With the objective of developing a design tool, it would be worthwhile to examine how to adapt this model such that the dimensionless parameters could be predicted in advance. Since the damping forces are developed primarily due to fluid drag, it may be possible to relate the damping parameters used in the model to a drag coefficient and the material properties of the fluid, all of which could be estimated from tabulated values in engineering textbooks. If the *quadratic damping frequency* and the foil resonant frequency could be estimated before constructing a prototype, the model could be used to predict the amplitude and phase responses and make adjustments to the design which would improve the efficiency or thrust production during operation at a particular oscillation frequency.

The Strouhal number is a second dimensionless frequency along with the frequency ratio which is known to affect the propulsive efficiency. In this study it was expected that performance could be improved by designing the foil and the oscillation kinematics such that optimal Strouhal number and frequency ratio occur at the same input motion frequency. This improvement in efficiency was not demonstrated in the results. It is expected that the effective width of the wake in the trials based on the trailing edge motion was significantly different from the width considered at the design stage based on the heave amplitude. To further investigate whether the propulsive efficiency can be improved by this matching of the optimal dimensionless frequencies, the trials could be repeated but with the flow speeds adjusted such that the expected optimal Strouhal number based on the trailing edge excursion occurs for the same frequency as the optimal frequency ratio. Flow visualisation techniques could also be used to examine the effect of the Strouhal number on the wake structure for the low-aspect-ratio design considered in this study so that the optimal Strouhal number could be properly identified with certainty rather than by assuming that the same trends identified for two-dimensional foils are also applicable in this case.

Appendix A

Resonant Frequencies of the Force Measurement System

If the load cell and the attached components are approximated as a second-order dynamic system, it is found that when oscillating forces are applied at up to one tenth of the lowest natural frequency, the error in the load cell readings due to the dynamic response of the system will be less than one percent [45]. In the set-up for the experiments in this study, the resonant frequencies were estimated to be 175 Hz for the force axes and 49 Hz for the torque axis which are both more than ten times the maximum oscillation frequency of 3 Hz. The details of calculation of these estimated resonant frequencies are included in this appendix.

The relevant resonant frequency, f_n, is given by

$$f_n = \frac{1}{2\pi}\sqrt{\frac{k}{I}} \tag{A.1}$$

where k is the stiffness of the load cell and I is the mass or inertia of the system including the load cell itself as well as the attached components [45].

The manufacturer estimates the stiffness of the load cell used in this study to be 5.8E6 N/m for the force axes and 5000 Nm/rad. for the torque axis.

For the force axes, the inertia of the relevant components of the experimental set-up have been measured and are listed in Table A.1.

Component	**Inertia**
Load cell	0.9 kg
Mast and Couplings	0.7 kg
Foil	1.0 kg

Table A.1: Relevant inertias for the estimate of the resonant frequencies of the load cell force axes.

In addition to the masses of the components, added mass effects from the water will make a significant contribution to the inertia. For a rectangular submerged plate, similar to the geometry of the foils, the added mass is given by [48]

$$\alpha \frac{\pi}{4} \rho l_1^2 l_2 \tag{A.2}$$

where ρ is the fluid density, l_1 is the short dimension of the rectangle and l_2 is the long dimension of the rectangle. The coefficient α depends on the aspect ratio of the rectangle and in the case of the foils considered here, the value $\alpha = 0.7$ is reasonable [48]. For a submerged circular cylinder such as the mast connecting the foils to the load cell, the added mass is given by [48]

$$\delta \pi \rho b^2 l^2 \tag{A.3}$$

where b is the radius of the cylinder and l is the length. The coefficient δ depends on the ratio of the length to the radius. For the mast used in the experiments, a value of $\delta = 0.96$ is reasonable [48]. The relevant parameters for use the the formulas given by Equations A.2 and A.3 are given in Table A.2

Parameter	**Value**
Water density, ρ	1000 kg/m^3
Foil dimension, l_1	0.14 m
Foil dimension, l_2	0.20 m
Submerged length of mast, l	0.15 m
Radius of mast, b	9.5 mm

Table A.2: Values of parameters necessary for the calculation of added mass effects.

Using the values in Table A.2, the effective inertia created by added mass effects is found to be 2.16 kg on the foil and 0.0413 kg on the mast. Combining these inertias with the measured values in Table A.1, the total relevant inertia for the force axes is approximately 4.8 kg. Substituting this value along with the stiffness into Equation A.1 gives a resonant frequency of 175 Hz.

To estimate the resonant frequency of the torque axis, it is necessary to determine the rotational inertia of the components from the mass and diameter or eccentricity. For circular cylinders, which can be used to represent the load cell and the mast, the inertia about an axis through the center is given by [48]

$$I = \frac{mB^2}{2} \tag{A.4}$$

where m is the mass and B is the radius. The distributed mass of the foil and its added mass effects are represented as a thin rod. For this geometry, the inertia about an axis which passes through the point at one end of the rod is given by [48]

$$I = \frac{mL^2}{3} \tag{A.5}$$

where L is the length of the rod. The embedded weights within the foils can be treated as if all of the mass is concentrated at a set distance, ϵ, from the axis of rotation. In this case the inertia is given by [48]

$$I = m\epsilon^2 \tag{A.6}$$

The geometric parameters and mass of the components for the use in Equations A.4-A.6 are tabulated along with the calculated rotational inertias in Table A.3. The inertia due to the added mass effects on the mast is not included since it is likely small and a convenient formula is not available for its calculation. The inertias of the foil, its added mass and the embedded weight were calculated about an axis through the leading edge rather than the pitching axis to make a more conservative estimate while also simplifying the calculations.

Parameter	**Value**
Load cell mass	0.9 kg
Load cell radius	0.045 m
Load cell inertia	9.11E-4 $\text{kg} \cdot \text{m}^2$
Mast mass	0.7 kg
Mast radius	9.5 mm
Mast inertia	3.18E-5 $\text{kg} \cdot \text{m}^2$
Foil distributed mass	0.62 kg
Foil length	0.2 m
Foil inertia	8.23E-3 $\text{kg} \cdot \text{m}^2$
Added mass	2.2 kg
Added mass length	0.2 m
Added mass inertia	2.93E-2 $\text{kg} \cdot \text{m}^2$
Embedded mass	0.38 kg
Eccentricity	0.2 m
Embedded mass inertia	1.53E-2 $\text{kg} \cdot \text{m}^2$

Table A.3: Rotational inertias of the force measurement system components.

The rotational inertias listed in Table A.3 are summed to give a total inertia of 5.4E-2 $\text{kg} \cdot \text{m}^2$. Substituting this inertia along with the stiffness into Equation A.1 gives a natural frequency of 49 Hz.

Appendix B

Solution of the Damped-oscillator Models for Amplitude Ratio

When solving to find the amplitude ratios predicted by Models 3, 4 and 5 described in Section 4.2 it is necessary to determine the solutions of quartic polynomials.

In the case of Model 3, which contains only quadratic damping proportional to the absolute velocity of the mass, the total equivalent damping ratio, ζ_{total} can be expressed in terms of the quadratic damping frequency as

$$\zeta_{total} = \frac{\omega}{2\omega_{qd}} \frac{\gamma_0}{h_0} \tag{B.1}$$

Substituting Equation B.1 into Equation 3.8 gives the implicit expression for the amplitude ratio:

$$\frac{\gamma_0}{h_0} = \frac{1}{\sqrt{\left(1 - r^2\right)^2 + \left(r \frac{\omega}{\omega_{qd}} \frac{\gamma_0}{h_0}\right)^2}} \tag{B.2}$$

which can be rearranged to give the quartic polynomial:

$$\left(r \frac{\omega}{\omega_{qd}}\right)^2 \left(\frac{\gamma_0}{h_0}\right)^4 + \left(1 - r^2\right)^2 \left(\frac{\gamma_0}{h_0}\right)^2 - 1 = 0 \tag{B.3}$$

Equation B.3 does not contain any cubic or linear terms and can therefore be solved by considering it as a quadratic polynomial in $(\gamma_0/h_0)^2$. Applying the quadratic formula [49] and considering only the positive root gives

$$\left(\frac{\gamma_0}{h_0}\right)^2 = \frac{-\left(1-r^2\right)^2 + \sqrt{\left(1-r^2\right)^4 + 4\left(r\frac{\omega}{\omega_{qd}}\right)^2}}{2\left(r\frac{\omega}{\omega_{qd}}\right)^2} \tag{B.4}$$

After evaluating the right side of Equation B.4, the amplitude ratio is easily determined by taking the square root and and again considering only the positive value.

When the oscillator is driven at its resonant frequency such that $r = 1$, Equation B.3 can be simplified and it is advisable to do so in order to reduce the numerical error in the evaluation of the solution. In this case, the amplitude ratio is given by

$$\frac{\gamma_0}{h_0} = \sqrt{\frac{\omega_{qd}}{\omega}} \tag{B.5}$$

When solving for the amplitude ratio predicted by Model 5, the *quadratic damping frequency* and *hysteretic damping frequency* can be used to express the relevant damping ratios as

$$\zeta_{total} = \frac{\omega}{2\omega_{qd}}\frac{\gamma_0}{h_0} + \frac{\omega_{hd}}{2\omega} \tag{B.6}$$

and

$$\zeta_{int} = \frac{\omega_{hd}}{2\omega} \tag{B.7}$$

Again, by substituting the damping ratios given by Equations B.6 and B.7 into Equation 3.8, we find that the amplitude ratio is given implicitly by

$$\frac{\gamma_0}{h_0} = \sqrt{\frac{1+\left(r\frac{\omega_{hd}}{\omega}\right)^2}{\left(1-r^2\right)^2 + \left[r\left(\frac{\omega_{hd}}{\omega} + \frac{\omega}{\omega_{qd}}\frac{\gamma_0}{h_0}\right)\right]^2}} \tag{B.8}$$

In a manner similar to the solution of Model 3, we rearrange the implicit expression given by Equation B.8 into a quartic polynomial but in this case a cubic term is present due to the component of the total damping ratio in Equation B.6 which does not depend on the amplitude. The resulting expression for the amplitude ratio is

$$\begin{aligned} &\left(r\frac{\omega}{\omega_{qd}}\right)^2\left(\frac{\gamma_0}{h_0}\right)^4 + 2r^2\frac{\omega_{hd}}{\omega_{qd}}\left(\frac{\gamma_0}{h_0}\right)^3 + \Big[\left(1-r^2\right)^2 + \\ &\qquad \left(r\frac{\omega_{hd}}{\omega}\right)^2\Big]\left(\frac{\gamma_0}{h_0}\right)^2 - \left[1+\left(r\frac{\omega_{hd}}{\omega}\right)^2\right] = 0 \end{aligned} \tag{B.9}$$

The amplitude ratio is then found by substituting the coefficients of Equation B.9 into the published formulae for the solution of quartic polynomials [49] and selecting the real, positive root. The solution of Model 4 is identical to that of Model 5 except that the internal damping ratio given by Equation B.7 and the second term of Equation B.6 are constant rather than varying with the reciprocal of the frequency of the applied motion.

Bibliography

[1] K. Jones, C. Bradshaw, J. Papadopoulos, and M. Platzer, “Bio-inspired design of flapping-wing micro air vehicles,” *Aeronautical Journal*, vol. 109, no. 1098, pp. 385–393, 2005.

[2] D. Roper, S. Sharma, R. Sutton, and P. Culverhouse, “A review of developments towards biologically inspired propulsion systems for autonomous underwater vehicles,” *Proceedings of the Institution of Mechanical Engineers, Part M: Journal of Engineering for the Maritime Environment*, vol. 225, no. 2, pp. 77–96, 2011.

[3] C. P. Ellington, “The novel aerodynamics of insect flight: Applications to micro-air vehicles,” *Journal of Experimental Biology*, vol. 202, no. 23, pp. 3439–3448, 1999.

[4] F. van Breugel, W. Regan, and H. Lipson, “From insects to machines: Demonstration of a passively stable, untethered flapping-hovering micro-air vehicle,” *IEEE Robotics & Automation Magazine*, vol. 15, no. 4, pp. 68–74, 2008.

[5] D. Barrett, M. Grosenbaugh, and M. Triantafyllou, “The optimal control of a flexible hull robotic undersea vehicle propelled by an oscillating foil,” in *Proceedings of the 1996 Symposium on Autonomous Underwater Vehicle Technology*, (Monterey, CA), pp. 1–9, 1996.

[6] G. C. H. E. de Croon, K. M. E. de Clercq, R. Ruijsink, B. Remes, and C. De Wagter, “Design, aerodynamics, and vision-based control of the delfly,” *International Journal of Micro Air Vehicles*, vol. 1, no. 2, pp. 71–97, 2009.

[7] M. S. Triantafyllou, A. H. Techet, and F. S. Hover, “Review of experimental work in biomimetic foils,” *IEEE Journal of Oceanic Engineering*, vol. 29, no. 3, pp. 585–594, 2004.

[8] J. E. Colgate and K. M. Lynch, “Mechanics and control of swimming: A review,” *IEEE Journal of Oceanic Engineering*, vol. 29, no. 3, pp. 660–673, 2004.

[9] S. P. Sane, “The aerodynamics of insect flight,” *Journal of Experimental Biology*, vol. 206, no. 23, pp. 4191–4208, 2003.

[10] S. Heathcote and I. Gursul, “Flexible flapping airfoil propulsion at low Reynolds numbers,” *AIAA Journal*, vol. 45, no. 5, pp. 1066–1079, 2007.

[11] K. D. Jones and M. F. Platzer, “Design and development considerations for biologically inspired flapping-wing micro air vehicles,” *Experiments in Fluids*, vol. 46, no. 5, pp. 799–810, 2009.

[12] J. M. Anderson, K. Streitlien, D. S. Barrett, and M. S. Triantafyllou, “Oscillating foils of high propulsive efficiency,” *Journal of Fluid Mechanics*, vol. 360, pp. 41–72, 1998.

[13] C. P. Ellington, C. van den Berg, A. P. Willmott, and A. L. R. Thomas, “Leading-edge vortices in insect flight,” *Nature*, vol. 384, pp. 626–630, Dec. 1996.

[14] M. H. Dickinson, F.-O. Lehmann, and S. P. Sane, “Wing rotation and the aerodynamic basis of insect flight,” *Science*, vol. 284, no. 5422, pp. 1954–1960, 1999.

[15] G. S. Triantafyllou, M. S. Triantafyllou, and M. A. Grosenbaugh, “Optimal thrust development in oscillating foils with application to fish propulsion,” *Journal of Fluids and Structures*, vol. 7, no. 2, pp. 205 – 224, 1993.

[16] M. M. Koochesfahani, “Vortical patterns in the wake of an oscillating airfoil,” *AIAA Journal*, vol. 27, no. 9, pp. 1200–1205, 1989.

[17] H. Dong, R. Mittal, and F. M. Najjar, “Wake topology and hydrodynamic performance of low-aspect-ratio flapping foils,” *Journal of Fluid Mechanics*, vol. 566, pp. 309–343, 2006.

[18] J. A. Shercliff, *Vector Fields: Vector Analysis Developed through its Applications to Engineering and Physics*. London, UK: Cambridge University Press, 1977.

[19] J. H. J. Buchholz and A. J. Smits, “The wake structure and thrust performance of a rigid low-aspect-ratio pitching panel,” *Journal of Fluid Mechanics*, vol. 603, pp. 331–365, 2008.

[20] K. D. von Ellenrieder, K. Parker, and J. Soria, “Flow structures behind a heaving and pitching finite-span wing,” *Journal of Fluid Mechanics*, vol. 490, pp. 129–138, 2003.

[21] P. Blondeaux, F. Fornarelli, L. Guglielmini, M. S. Triantafyllou, and R. Verzicco, “Numerical experiments on flapping foils mimicking fish-like locomotion,” *Physics of Fluids*, vol. 17, Nov. 2005.

[22] P. R. Bandyopadhyay, J. M. Castano, W. H. Nedderman, and M. J. Donnelly, “Experimental simulation of fish-inspired unsteady vortex dynamics on a rigid cylinder,” *Journal of Fluids Engineering-Transactions of the ASME*, vol. 122, pp. 219–238, Jun. 2000.

[23] O. Barannyk, B. J. Buckham, and P. Oshkai, “On performance of an oscillating plate underwater propulsion system with variable chordwise flexibility at different depths of submergence,” *Journal of Fluids and Structures*, vol. 28, pp. 152–166, 2012.

[24] G. V. Lauder, “Swimming hydrodynamics: Ten questions and the technical approaches needed to resolve them,” *Experiments in Fluids*, vol. 51, no. 1, pp. 23–35, 2011.

[25] J. Young, S. M. Walker, R. J. Bomphrey, G. K. Taylor, and A. L. R. Thomas, “Details of insect wing design and deformation enhance aerodynamic function and flight efficiency,” *Science*, vol. 325, no. 5947, pp. 1549–1552, 2009.

[26] D. L. Altshuler, R. Dudley, and C. P. Ellington, “Aerodynamic forces of revolving hummingbird wings and wing models,” *Journal of Zoology*, vol. 264, no. 4, pp. 327–332, 2004.

[27] K. Isogai, Y. Kamisawa, and H. Sato, “Resonance type flapping wing for micro air vehicle,” *Transactions of the Japan Society for Aeronautical and Space Sciences*, vol. 52, pp. 199–205, Feb. 2010.

[28] P. Wu, B. Stanford, E. Sällström, L. Ukeiley, and P. Ifju, “Structural dynamics and aerodynamics measurements of biologically inspired flexible flapping wings,” *Bioinspiration & Biomimetics*, vol. 6, no. 1, p. 016009, 2011.

[29] J. Katz and D. Weihs, "Hydrodynamic propulsion by large amplitude oscillation of an airfoil with chordwise flexibility," *Journal of Fluid Mechanics*, vol. 88, pp. 485–497, 1978.

[30] S. Heathcote, Z. Wang, and I. Gursul, "Effect of spanwise flexibility on flapping wing propulsion," *Journal of Fluids and Structures*, vol. 24, no. 2, pp. 183–199, 2008.

[31] S. Ramananarivo, R. Godoy-Diana, and B. Thiria, "Rather than resonance, flapping wing flyers may play on aerodynamics to improve performance," *Proceedings of the National Academy of Sciences of the United States of America*, vol. 108, pp. 5964–5969, Apr. 2011.

[32] S. Michelin and S. G. L. Smith, "Resonance and propulsion performance of a heaving flexible wing," *Physics of Fluids*, vol. 21, Jul. 2009.

[33] B. Yin and H. Luo, "Effect of wing inertia on hovering performance of flexible flapping wings," *Physics of Fluids*, vol. 22, Nov. 2010.

[34] Q. Zhu, "Numerical simulation of a flapping foil with chordwise or spanwise flexibility," *AIAA Journal*, vol. 45, no. 10, pp. 2448–2457, 2007.

[35] H. W. Coleman and W. G. Steele, *Experimentation and Uncertainty Analysis for Engineers*. Toronto, ON: John Wiley and Sons, 1989.

[36] T. R. Padmanabhan, *Industrial Instrumentation: Principles and Design*. New York, NY: Springer, 2000.

[37] Novatech Measurements Limited, *Engineering Application Sheet E010 - Temperature*, 2013.

[38] National Instruments Corporation, *NI 4472 User Manual*, 2001.

[39] Parker Hannifin Corporation, *ACR9000 Series Hardware Installation Guide*, 2010.

[40] B. Gold and C. M. Rader, *Digital Processing of Signals*. Toronto, ON: McGraw-Hill, 1969.

[41] The Mathworks, *Matlab Function Reference*, 2010.

[42] Novatech Measurements Limited, *Engineering Application Sheet E007 - Measurement Mode*, 2013.

[43] Novatech Measurements Limited, *Engineering Application Sheet E004 - Repeatability*, 2013.

[44] Novatech Measurements Limited, *Engineering Application Sheet E009 - Cross Talk*, 2013.

[45] Novatech Measurements Limited, *Engineering Application Sheet E006 - Dynamic Force Measurement*, 2013.

[46] D. J. Inman, *Engineering Vibration.* Upper Saddle River, NJ: Pearson Education Inc., third ed., 2008.

[47] I. H. Tuncer and M. Kaya, "Optimization of flapping airfoils for maximum thrust and propulsive efficiency," *AIAA journal*, vol. 43, no. 11, pp. 2329–2336, 2005.

[48] R. D. Blevins, *Formulas for Natural Frequency and Mode Shape.* Malabar, FL: Krieger Publishing Company, 2001.

[49] D. Zwillinger, *CRC Standard Mathematical Tables and Formulae.* Boca Raton, FL: Taylor & Francis Group, thirty-second ed., 2012.